A comprehensive study on the mechanical properties and microstructure of 18Ni-300 maraging steel produced with various process parameters via powder bed fusion technique

by
Seyedamirreza Shamsdini

A Dissertation Submitted in Partial Fulfillment
of the Requirements for the Degree of

Doctor of Philosophy

in the Graduate Academic Unit of Mechanical Engineering

Supervisor: Mohsen Mohammadi, Ph.D., Department of Mechanical Engineering

Examining Board: Edmund Biden, D.Phil., Department of Mechanical Engineering
Clodualdo Aranas, Ph.D., Department of Mechanical Engineering
Huining Xiao, Ph.D., Department of Chemical Engineering

External Examiner: Amir Mostafaei, Ph.D., Department of Mechanical, Materials and Aerospace Engineering, Illinois Institute of Technology

This dissertation is accepted by the
Dean of Graduate Studies

THE UNIVERSITY OF NEW BRUNSWICK

April 2021

© Seyedamirreza Shamsdini, 2021

Abstract

A comprehensive study was conducted to investigate the mechanical properties and microstructure of additively manufactured 18Ni-300 maraging steel. The gas-atomized powder was used as the feedstock, and the morphology and microstructure were examined to reveal the cellular structure with a majority of spherical powder particles. Cubic samples were built with 40 and 50 µm powder layer thicknesses. The 40 µm samples were built using ceramic and brush recoater blades. The three variations were then heat-treated, and all six sets of samples were studied to measure porosity in different layers. All samples showed relatively low porosity levels. The porosity level was shown to increase a few millimetres underneath the finished surface and then decrease gradually. The heat-treatment process was shown to decrease the porosity level due to the evolution of the microstructure. The hardness was also measured for different layers, and no variation was observed through the depth. The aged samples also showed higher hardness due to precipitations. Uniaxial tensile tests were conducted on test coupons by varying powder layer thickness, build direction, and recoater blades. The mechanical properties and microstructure of the specimens were studied before and after the deformation. In the as-built case, horizontal samples showed higher strength and ductility due to lower thermal stress from the manufacturing process. The powder layer thickness showed not to affect the mechanical properties significantly. Besides, the ceramic recoater showed slightly better mechanical properties due to the powder particle's better spreadability over the build plate. The heat-treatment increased the mechanical strength significantly for both horizontal and vertical samples, while the ductility dropped as a payoff. The aged samples showed to have similar strength regarding their building direction with lower ductility of

the vertical samples. Lower ductility was related to the building orientation due to the grain growth direction, while the strength was related to precipitation, regardless of the build orientation. All cases showed a phase transformation through the deformation process. The as-built cases turned into a fully martensitic structure, and the aged samples transformed a portion of the austenite into martensite.

Dedication

To my parents that their memories encourage me every day.

Acknowledgement

I am grateful to Dr. Mohsen Mohammadi, who gave me this opportunity to start my journey as a Ph.D. student and patiently guided me through this process. The Ph.D. was more than a program to me. I learned how to broaden my vision with the existing capabilities and share my knowledge as gratitude.

Heartful thanks go to Dr. Edmund Biden for teaching me how to see the big picture with his thoughtful comments. I want to thank Dr. Clodualdo Aranas for his ideas and comments, bringing insight into this work and Dr. Huining Xiao, and Dr. Amir Mostafaei who kindly agreed to stand on the committee.

I am grateful to the Mechanical Engineering department staff who helped me start my new life as a student at UNB, Paulette Steever, Ann Bye, and Debbie Basque. I am also thankful to the technicians who helped me conduct the experiments, Vince Boardman, Brian Guidry, and Gregory Greer. I should also thank Dr. Zahra Khatami from the Electrical Engineering department, Dr. Dennis Connor from UNB Civil Engineering, Steven Cogswell from UNB's Microscopy and Microanalysis Facility (MMF), Dr. Hamed Asgari from the University of Waterloo, Dr. Amir Hadadzadeh from the University of Memphis, Dr. Babak Shalchi Amirkhiz from the CanmetMATERIALS, Dr. Hadi Pirgazi and Dr. Leo Kestens from Ghent University, Victoria Jarvis, Dr. Jim Britton, and Dr. Zhilin Peng from McMaster University.

My appreciation also extends to all MAMCE members as postdoctoral fellows and students and staff who helped me during my program, especially to Sajad Shakerin, MohammadHossein Ghoncheh, Krista McCarthy, and Dr. Mehdi Sanjari.

I am also thankful to my wonderful friends Dr. Ali Zeighami and Dr. Sara Babaei, who encouraged and helped me start my journey.

Finally, I should thank my brothers Shahin Shamsdini, Afshin Shamsdini, their families, and my friends, especially Ken Yeamans, who always support me and are available whenever I need them.

Table of contents

Abstract ii
List of tables x
List of figures xi
Chapter 1 Introduction 1
1.1 Maraging steels 4
1.2 Additive manufacturing 6
1.3 Literature review 8
1.3.1 Manufacturing process 8
1.3.1.1 History of AM 8
1.3.1.2 Different methods 9
1.3.2 Process parameters 11
1.3.2.1 Energy density and optimization of process parameters 11
1.3.2.2 Porosity and relative density 13
1.3.2.3 Building direction 14
1.3.3 Pre and post-process parameters 16
1.3.3.1 Powder metallurgy and recoating mechanism 16
1.3.3.2 Heat-treatment 17
1.3.4 Mechanical properties 18
1.3.5 Microstructure 20
1.3.6 Crystal structure 21
1.4 Gap of knowledge 24
1.5 Contributions 26
1.6 Comments on the papers 28
1.7 Study outline 30
1.8 Contribution to mechanical engineering 32
1.9 Hypothesis 33
1.10 Funding 34
1.11 References 35
Chapter 2 A trade-off between powder layer thickness and mechanical properties in additively manufactured maraging steels 44
2.1 Introduction 45
2.2 Experimental procedures 47

2.2.1 Materials and LPBF process 47
2.2.2 Characterization 48
2.2.3 Mechanical properties 50
2.3 Results 52
2.3.1 Powder characteristics 52
2.3.2 LPBF-MS1 solidification 55
2.3.3 Characterization and grain structure 60
2.3.4 Mechanical properties 66
2.4 Discussion 82
2.4.1 Properties through the depth 82
2.4.2 Phase change due to additive manufacturing process 83
2.4.3 Grain structure during deformation 84
2.5 Conclusions 85
2.6 References 87
Chapter 3 Plastic deformation throughout strain-induced phase transformation in additively manufactured maraging steels 95
3.1 Introduction 96
3.2 Experimental procedure 99
3.2.1 Material and manufacturing process 99
3.2.2 Sample preparation and tensile testing 100
3.2.3 Phase identification 101
3.2.4 Electron microscopy 101
3.3 Results 102
3.4 Discussion 118
3.4.1 Phase transformation 118
3.4.2 Plastic deformation 119
3.4.3 Strain hardening 120
3.5 Conclusions 122
3.6 References 123
Chapter 4 A relationship between the build and texture orientation in tensile loading of the additively manufactured maraging steels 130
4.1 Introduction 131
4.2 Experimental procedures 134
4.2.1 Manufacturing process 134

4.2.2 Through the depth properties 135
4.2.3 Mechanical properties 136
4.2.4 Electron microscopy and texture analyses 137
4.2.5 X-ray diffraction technique 137
4.3 Results 138
4.4 Discussion 155
4.4.1 Grain structure 155
4.4.2 Phase transformation 155
4.4.3 Mechanical properties 157
4.4.4 Deformation mechanism 158
4.5 Conclusions 159
4.6 References 161
Chapter 5 Effect of recoater-blade type on the mechanical properties and microstructure of additively manufactured maraging steels 168
5.1 Introduction 168
5.2 Experimental procedure 169
5.3 Results 171
5.4 Discussion 177
5.5 Conclusions 179
5.6 References 180
Chapter 6 Summary 182
6.1 Final remarks 182
6.2 Additional information on the published works 184
Chapter 7 Conclusions and future works 186
7.1 Conclusions 186
7.2 Recommendation for future work 190
7.2.1 Tailored mechanical properties 190
7.2.2 Modelling and simulations 192
Appendix A. 193
Curriculum Vitae

List of tables

Table 1.1 Martensite and austenite start and end temperatures for 18Ni-maraging steel (Dos Reis, et al., 2015) 22
Table 2.1 Chemical composition of maraging steel MS1 powder (Material data sheet, 2017) 48
Table 2.2 LPBF process parameters applied in this research..... 48
Table 2.3 Particle size average and cumulative distribution percentage (while μ is the average particle size and σ represents the standard deviation). All data are in μm. 54
Table 3.1 Chemical composition of the powder used in the DMLS process (Material Data sheet, 2017) 100
Table 3.2 The average grain size for each variation of specimens 113
Table 4.1 Chemical composition of the 18Ni-300 maraging steel powder (Material Data sheet, 2017) 135
Table 4.2 LPBF process parameters applied in the current study..... 135
Table 4.3 Uniaxial tensile test specimens' dimensions (Standard, 2015). 137
Table 4.4 Mechanical properties of 18Ni-300 maraging steel, (AB: As-built, HT: Heat-treated, H: horizontal, V: Vertical, ST: Solution-treated), (Becker, et al., 2016), (Vishwakarma, et al., 2020), (Kempen, et al., 2011), and (Handbook, 1990)..... 143
Table 4.5 Austenite phase fraction for various samples (All data in % with ±0.2% error). 149
Table 5.1 Chemical composition of the maraging steel MS1 feedstock powder (sheet, 2017). .. 170

List of figures

Fig. 1-1 Schematic of the Direct Metal Laser Sintering (DMLS) process. 3
Fig. 1-2 Process parameters defined for core and contour of a build (Mohammadi and Asgari, 2018). 12
Fig. 1-3 Porosity due to overlapping (Gong, et al., 2014) 13
Fig. 1-4 Porosity versus scan speed (Gong, et al., 2014) 14
Fig. 1-5 Horizontal vs vertical build in the additive manufacturing process (Hadadzadeh et al., 2018). 16
Fig. 1-6 Three deposition methods (a) scraper blade (b) counter rolling cylinder, (c) slot feeder (Van der Schueren et al., 1995) 17
Fig. 1-7 Fe-Ni system metastable phase diagram (Tan et al., 2017). 22
Fig. 2-1 Schematic of the uniaxial tensile test sample and the cubic samples. 51
Fig. 2-2 SEM image for MS1 powder at two different magnifications for (a-b): morphology, and (c-d): microstructure. 53
Fig. 2-3 The particle size distribution of the MS1 powder. 54
Fig. 2-4 Variation of the porosity through the depth of LPBF-MS1-40 and LPBF-MS1-50 cubes. 56
Fig. 2-5 XRD analysis of the MS1 powder, LPBF-MS1-40, and LPBF-MS1-50 cubes. 58
Fig. 2-6 SEM image at three different magnifications of (a-c): LPBF-MS1-40 cube, and (d-f): LPBF-MS1-50 cube. 59
Fig. 2-7 EBSD mappings showing (a): IPF orientation map of LPBF-MS1-40, (b): IPF orientation map of LPBF-MS1-50, (c): phase map of LPBF-MS1-40, (d): phase map of LPBF-MS1-50. 61
Fig. 2-8 XRD Pole Figures showing Phase maps at (a): LPBF-MS1-40, and (b): LPBF-MS1-50, ODF sections at φ_2=45° shown at (c): LPBF-MS1-40, and (d): LPBF-MS1-50. 62
Fig. 2-9 STEM-HAADF image and the corresponding EDS elemental maps of LPBF-MS1-40. 64
Fig. 2-10 STEM-HAADF image and the corresponding EDS elemental maps of LPBF-MS1-50. 65
Fig. 2-11 Variation of hardness through the depth of LPBF-MS1-40 and LPBF-MS1-50 cubes. 66
Fig. 2-12 Typical uniaxial tensile stress-strain curves of LPBF-MS1-40 and LPBF-MS1-50. 67
Fig. 2-13 Ultimate strength versus elongation in various studies for the as-built additively manufactured 18Ni-300 maraging steel including this study. 68

Fig. 2-14 SEM images of fracture surface at two different magnification for (a, c): LPBF-MS1-40, (b, d): LPBF-MS1-50. 69
Fig. 2-15 Grain color map of deformed samples for (a): LPBF-MS1-40, and (b): LPBF-MS1-50. 70
Fig. 2-16 XRD Pole Figures of deformed samples showing grain orientation (a): LPBF-MS1-40, (b): LPBF-MS1-50, ODF sections at φ_2=45° of deformed samples (c): LPBF-MS1-40, and (d): LPBF-MS1-50. 72
Fig. 3-1 Schematic design of the tensile test sample showing the powder layer thickness. 101
Fig. 3-2 OM micrographs showing porosity in (a): LPBF-40, (b): LPBF-50. 102
Fig. 3-3 Tensile stress-strain curves and the corresponding strain hardening variation 104
Fig. 3-4 Ultimate tensile strength versus fracture strain for 18Ni-300 maraging steels produced using both additive and conventional manufacturing techniques (Tan, et al., 2017), (Dehgahi, et al., 2020), (Kučerová, et al., 2019), and (Bhardwaj, et al., 2018). 104
Fig. 3-5 (a, b): IPF for LPBF-40-A, LPBF-50-A, (c, d): Pole figures for LPBF-40-A and LPBD-50-A, (e, f): ODF for LPBF-40-A, LPBF-50-A, (g): ODF key components (Sanjari, et al., 2017). 106
Fig. 3-6 XRD pattern for the 18Ni-300 deformed and undeformed samples in zones A and C. . 107
Fig. 3-7 (a, b): IPF for LPBF-40-B, LPBF-50-B, (c, d): Pole figures for LPBF-40-B and LPBD-50-B, (e, f): ODF for LPBF-40-B, LPBF-50-B. 108
Fig. 3-8 (a, b): IPF for LPBF-40-C, LPBF-50-C, (c, d): Pole figures for LPBF-40-C and LPBD-50-C, (e, f): ODF for LPBF-40-C, LPBF-50-C. 109
Fig. 3-9 EBSD grain boundary maps in three different zones shown for (a, b): LPBF-40-A, LPBF-50-A, (c, d): LPBF-40-B, LPBF-50-B, and (e, f): LPBF-40-C, LPBF-50-C. 110
Fig. 3-10 EBSD KAM in three different zones shown for (a, b): LPBF-40-A, LPBF-50-A, (c, d): LPBF-40-B, LPBF-50-B, and (e, f): LPBF-40-C, LPBF-50-C. 112
Fig. 3-11 Grain size distribution in different zones of the LPBF-40 and LPBF-50 samples. 113
Fig. 3-12 Misorientation angle distribution in different zones of the LPBF-40 and LPBF-50 samples. 114
Fig. 3-13 STEM-BF image and corresponding elemental distribution maps in the LPBF-40-C sample. 116
Fig. 3-14 STEM-BF image and corresponding elemental distribution maps in the LPBF-50-C sample (i: dislocations). 118
Fig. 4-1 Schematic of the uniaxial tensile test samples. 136
Fig. 4-2 Through the depth porosity and hardness for samples (a): As-built, (b): heat-treated. .. 139

Fig. 4-3 SEM micrographs for samples (a): As-built, horizontally printed (b): As-built, Vertically printed, (c): heat-treated, horizontally printed, and (d): heat-treated, vertically printed..... 140
Fig. 4-4 stress-strain curves for as-built and heat-treated samples on both horizontally and vertically printed samples. 141
Fig. 4-5 Fracture surface for samples (a): as-built, horizontal, (b): as-built, vertical, (c): heat-treated, horizontal, (d): heat-treated, vertical. 144
Fig. 4-6 BF-STEM micrographs for samples (a): as-built, horizontal, (b): as-built, vertical, (c): heat-treated, horizontal, (d): heat-treated, vertical. 145
Fig. 4-7 BF-STEM micrograph, along with the element distribution map for heat-treated samples printed in the horizontal direction. 146
Fig. 4-8 BF-STEM micrograph, along with the element distribution map for heat-treated samples printed in the vertical direction. 147
Fig. 4-9 XRD intensity over 2θ range in the undeformed condition for as-built and heat-treated samples in horizontal and vertical directions. 148
Fig. 4-10 XRD intensity over 2θ range in the deformed condition for as-built and heat-treated samples in horizontal and vertical directions. 149
Fig. 4-11 EBSD plots for as-built vertical samples (a): IPF, undeformed, (b): IPF, deformed, (c): PF, undeformed, (d): PF, deformed. (e): texture simulation based on the FC-Taylor model and uniaxial tensile deformation. 151
Fig. 4-12 EBSD plots for aged, horizontal samples (a): IPF, undeformed, (b): IPF, deformed, (c): PF, undeformed, (d): PF, deformed. 153
Fig. 4-13 EBSD plots for aged vertical samples (a): IPF, undeformed, (b): IPF, deformed, (c): PF, undeformed, (d): PF, deformed. 154
Fig. 5-1 SEM in different magnifications for (a,b,c): *LPBF-Brush*, (d,e,f): *LPBF-Ceramic*. 172
Fig. 5-2 Engineering stress-strain curves comparing *LPBF-Brush* and *LPBF-Ceramic* samples. 173
Fig. 5-3 Porosity and hardness measured through the depth (a): LPBF-Brush sample, (b): LPBF-Ceramic sample (Shamsdini, et al., 2020). 174
Fig. 5-4 SEM at low and high magnifications for (a-b): *LPBF-Ceramic*, and (c-f): *LPBF-Brush.* 175
Fig. 5-5 XRD-ODF graphs for *LPBF-Ceramic* samples (a): undeformed, (b): deformed, *LPBF-Brush* (c): undeformed, (d): deformed, and (e): reference system. 177

Chapter 1

Introduction

Additive manufacturing (AM) adds layers of a substance in powder or wire form through a melting process and builds up a solid volume incrementally. Such a procedure is controlled by computer software, converting a CAD model into a solid object. The additive manufacturing process explained is addressed as 3D-printing in the market. Developments recently can be categorized to wrought materials as the input of the AM process, especially in metal powder quality, the fusion process of the addition such as laser beam or electron beam sintering and melting, and the machine capabilities such as its maximum dimensions. All the mentioned developments result in higher quality products in terms of density and mechanical properties in comparison with conventional manufacturing techniques.

Forming and subtracting procedures have been the leading manufacturing technologies for decades. The concept of adding layers to each other in order to manufacture a 3D object is introduced as the new production technology for agile production purposes. AM is a new and fast-growing technology, which has many advantages compared to forming and subtracting methods. Increasing production speed, fabricating objects with complicated geometries, reducing material waste, and decreasing the production price motivate the manufacturers to invest in and develop this technology.

Additive manufacturing of high-strength steels and stainless steels has received tremendous attention recently due to their superior mechanical properties, versatility, and compatibility with post-processing subtractive techniques. The high-strength alloy steels such as maraging steels are iron-based alloys with low carbon content, and the precipitation

of intermetallic compounds is the strengthening mechanism for such materials. The material discussed in this research has the commercial name 18Ni (300) maraging steel, where the 300-grade index shows the strength range in ksi.

Many industrial sectors, including aerospace, oil and gas, energy, and marine, are currently investigating the use of additive manufacturing techniques in their supply chain and ways their products can compete with conventional counterparts. All industries involved with high-strength materials, including defence, aerospace, marine, subsea oil and gas, and manufacturers in automotive and tooling industries, are currently dealing with this new technology or discussing its adoption.

Fig. 1-1 shows a schematic of the direct metal laser sintering (DMLS) method as one known powder bed fusion technique. In this method, the powder supply container's virgin powder is spread over the build platform using a recoater blade. The recoater blade might be made of ceramic, known as hard recoater, or carbon fibre brush or rubber, known as soft recoater. The powder's height spread over the build plate in each layer is called the powder layer thickness. Receiving input from a computer-aided design (CAD) code, the laser unit applies the energy source. The laser power melts down the powder particles and forms a thin layer. The excess powder, which might contain heat-affected particles, is then collected into the powder collection container. This powder is referred to as condensate or used powder. The whole process repeats, and each layer of powder is sintered into the solidified layers underneath.

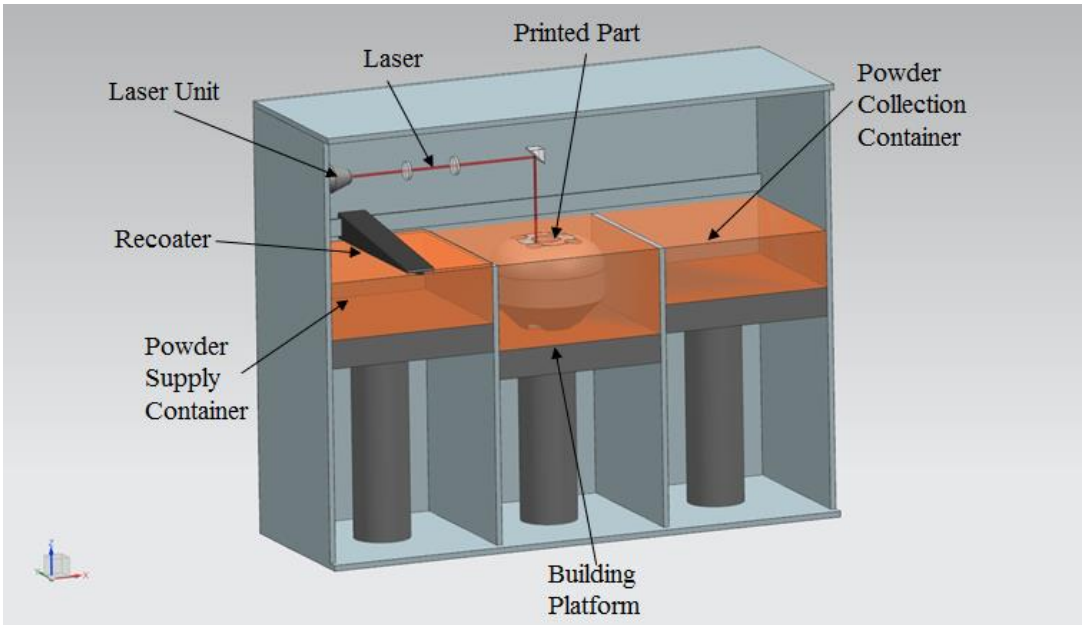

Fig. 1-1 Schematic of the Direct Metal Laser Sintering (DMLS) process.

1.1 Maraging steels

Among alloy steels, maraging steel is well known due to its superior mechanical properties. This high-strength steel class was first introduced and developed during the '50s and is of great importance yet. This alloy consists of high nickel content with a low carbon weight percentage. The martensitic (bcc) structure is formed during a diffusionless transformation from (fcc) crystal structure in maraging steels. The name maraging is based on the aging of martensitic structure in these alloys; see, e.g. (Floreen, 1968), (Sha, et al., 1993), (Belyakov, et al., 1968) for more details.

The three essential alloying elements in this type of material are nickel, cobalt, and molybdenum, followed by titanium and aluminum. Each alloying element has its effect on the material's behavior, and changing the weight balance highly affects the microstructure and mechanical properties. It is worth noting that, the maraging steel contains carbon lower than 0.03% (weight) and the intermetallic precipitates govern the age hardening. The two significant grades of 18% nickel maraging steel are C-grade and T-grade, in which the former contains 4-5% cobalt and a low amount of Titanium, and the latter is free of cobalt with a higher amount of Titanium (Vasudevan et al., 1990). As mentioned earlier, by changing the alloying element weight percentage, the mechanical properties are significantly affected. For example, for 8.5% cobalt, by increasing molybdenum content from 3.3 to 5% and titanium from 0.2 to 0.4%, the yield strength increases from 1400 to 1700 MPa. Higher strength up to 2400 MPa can be reached by having 12.5% cobalt, 4.2% molybdenum, and 1.6% titanium (Sha et al., 2009).

Each alloying element has its footprint in maraging steel. The nickel has two major contributions to the mechanical properties, which are helping to form precipitates as well

as controlling the austenite reversion. Although cobalt forms no precipitates, the cobalt element's existence prevents the formation of molybdenum solution in the matrix and results in the formation of Fe7Mo6 precipitates. As mentioned earlier, titanium and molybdenum form precipitations, which are the main strengthening mechanisms in maraging steel (Sha et al., 1993).

A comprehensive study on high strength maraging steel with different compositions has been done previously, where better mechanical properties of maraging steel were achieved by the precipitation of copper in the microstructure (Li et al., 2017). It was also shown that, the mechanical properties of Mn-based maraging steels are highly affected by different precipitates and aging conditions (Qian et al., 2016). The mechanical properties of maraging stainless steels 13-8 PH Mo change dramatically in high-temperature conditions due to the changes in the microstructure and phases (Huang et al., 2016). This is because the austenite reversion due to temperature increase significantly affects maraging steel's hardness (Dos Reis et al., 2015). High strength maraging steel with Cr-rich composition showed three precipitation phases in the microstructure, including Ni-rich, Mo-rich, and Cr-rich phases (Li et al., 2015). Sha et al. (Sha et al., 2013) showed that various mechanical properties could be achieved for low Ni maraging steels.

1.2 Additive manufacturing

For many years, manufacturing methods were restricted to conventional forming operations and subtractive techniques from an initial shape to the final product. A new method has recently attracted the attention of many researchers and engineers called material accretion manufacturing or rapid prototyping or additive manufacturing (AM) (Kruth, 1991). This method was first introduced in the '80s using the stereolithography process, applicable in polymer production, see e.g., (Kodama, 1981), (Kruth et al., 1998). In general, AM refers to methods by which 3D objects are formed layer by layer from CAD models (Asgari et al., 2017). Of particular interest in this contribution is metal additive manufacturing (MAM), where mainly metal powder or wire is fused using different energy sources, including laser or electron beam.

AM's three main processes are introduced using different machine manufacturers called sintering, melting, and metal deposition processes (Gu et al., 2012). Selective metal sintering (SMS) was one of the initial steps forward to make metal parts using additive procedures. In this method, heat applied to one metal powder layer melts the layer, and after solidification, a new layer is added the same way to the previous one, and this incrementally produces a 3D object, see e.g., (Van der Schueren et al., 1995), (Agarwala, et al., 1995), (Kruth et al., 1996). On the other hand, in the SLS process, the laser beam acts as the heat source on the metal powder to make the 3D object (Kruth et al., 1998). The latter technique and the melting process were then called selective laser melting (SLM) or laser beam melting (LBM). An alternative for laser as the heat source has been the electron beam, which led to another technique parallel to SLM called electron beam melting (EBM) (Murr et al., 2012). The EOS GmbH has introduced its own SLM technique called direct

metal laser sintering (DMLS) process, which was used to produce all the samples for this study. Recent studies show that AM techniques are cost-efficient in small batch production comparing to conventional methods (Atzeni et al., 2012), and they have a great impact on the spare-part supply chain (Khajavi et al., 2014) and repair and maintenance (Cyr et al., 2018).

1.3 Literature review

1.3.1 Manufacturing process

1.3.1.1 History of AM

Additive manufacturing goes back to the time when plastic polymers were first manufactured in three dimensions (Kodama, 1981). In this method, photo-hardening liquid material was exposed to an ultraviolet light layer by layer, and the three-dimensional polymer was solidified. In such a technique, complicated shapes were manufactured for the first time with internal structures. The power source applied was 200-500 W with a 2-3 mm beam diameter. In this technique, the layer thickness was 2-6 mm, with a scanning speed of 0.5-2.5 mm/min. The novel additive manufacturing then expanded into a broader range of material, and different names and techniques were introduced to address the new manufacturing technique based on adding material to building parts. Rapid prototyping, CAD oriented manufacturing, design controlled automated fabrication, direct CAD manufacturing, 3D printing, desktop manufacturing, instant manufacturing, layer manufacturing, laminated object manufacturing, solid free-form fabrication, material deposit manufacturing, material addition manufacturing, material increase manufacturing are all referring to the same concept (Kruth, 1991).

Different techniques were then categorized based on the supply material into solid, liquid, gas, and powder. Laminated object manufacturing uses the deposition of sheet metals to build parts. Chemical vapour deposition produces solid parts by forming gas through chemical reactions. Stereolithography, fuse deposition modelling, and inkjet printing are three techniques that use liquid material to build parts. Three-dimensional print, selective laser sintering, and laser cladding are known to manufacture using powder

(Kruth, et al., 1998). The laser powder sintering was then successful in melting Fe-Cu powder into 55 % relative density in a selective laser sintering process (Kruth, et al., 1996). The laser power used was 90 W with 0.6 mm layer thickness and 50 mm/s scanning speed.

1.3.1.2 Different methods

Wire arc additive layer manufacturing (WAALM) is one of the additive techniques in which large scale components can be manufactured quickly. The energy source in this method is applied through an electric arc to the welding wire (Ding et al., 2011). This technique is shown to produce fully dense 18Ni-maraging steels with higher mechanical properties and anisotropy along the build direction in the as-build condition (Xu et al., 2018). However, in aged condition, the mechanical properties could increase with plastic deformation compared to the wrought maraging steel (Xu et al., 2019). The wire arc additive manufacturing also divides into three gas tungsten, plasma, and gas metal arc welding (GTAW, PAW, and GMAW) techniques. The heat dissipation orientation was modeled by Xiong et al. (Xiong et al., 2018) in GTAW, showing the temperature gradients in different layers. Due to high heating and cooling rates, the heating load cycles significantly affect the mechanical properties of the additively manufactured parts compared to conventionally manufactured ones. A study on GTAW was conducted by Rajkumar et al. (Rajkumar et al., 2014) in continuous current and pulse current variation to weld maraging steel into low alloy steel. The microstructure of the interface zone was studied, showing integrated weldments. In another study conducted by Sakai et al. (Sakai et al., 2015), maraging steel was welded with laser, plasma, and Tungsten Inert Gas (TIG) techniques, and the results were compared, showing similar properties.

The electron beam is another heat source for additive manufacturing. This method applies a higher energy density to melt the material with lower cooling rates than the laser beam. Various materials have been studied and compared in laser and electron beam melting (Murr, et al., 2012). Both techniques result in adding a new dimension of microstructural architecture to the manufacturing world. The electron beam technique was implemented on Inconel 718 by Sun et al. (Sun et al., 2018), and various build orientations were studied. They found that the building height was a more influencing parameter than the build orientation. The Selective laser beam technique versus Electron beam melting was compared in a study on Ti-6Al-4V. The process parameters and the beam melting technique significantly affected the defect generation (Gong et al., 2014).

Laser additive manufacturing is categorized based on partial melting versus complete melting of powder in a study by Gu et al. (Gu et al., 2012). Different material powders were reviewed with the three methods of laser sintering (LS), laser melting (LM), and laser metal deposition (LMD).

Maraging steel is produced through the laser powder bed fusion technique and conventional manufacturing (Jägle et al., 2017). The precipitation hardening is considered through the manufacturing process before aging.

A series of process parameters were introduced by Agarwala et al. (Agarwala et al., 1995) as control parameters, machine-specific, and geometry specifics, and material properties that all affected the additive process. Various materials were then reviewed in terms of mechanical behavior based on the process parameter optimization. A relationship between the thermal history with the mechanical properties and process parameters is investigated for a broad range of materials.

The maraging steel-H13 bimetal interface was studied by Shakerin et al. (Shakerin et al., 2019). The application of building material on top of fractured parts was considered, and the mechanical properties and microstructure of the interface were investigated.

1.3.2 Process parameters

1.3.2.1 Energy density and optimization of process parameters

In the laser powder bed fusion (LPBF) technique, which is the current study's manufacturing method, the energy is applied through a laser beam. The energy density E_d (J/mm^2) can be calculated based on the laser power P (W), scanning speed v (mm/s), and laser spot diameter d (mm) as Eq. (2.1) (Campanelli et al., 2010):

$$E_d = \frac{P}{v.d} \tag{2.1}$$

The above equation shows the energy applied to a single track of the surface. Eq. (2.1) can be modified to the energy density over the volume E_v (J/mm^3) as Eq. (2.2):

$$E_v = \frac{P}{v.h.t} \tag{2.2}$$

where t (mm) is the powder layer thickness and h (mm) is the hatch spacing (the distance between the centre line of the laser track with the parallel track).

Considering the process parameters mentioned in Eq. (2.2), Casalino et al. (Casalino et al., 2015) correlated the mechanical properties and the relative density affected by the process parameters. Bai et al. (Bai et al., 2017) also studied the mechanical properties of 18Ni maraging steel and developed a set of optimized process parameters to reach the highest relative density. Dilip et al. (Dilip et al., 2017) did a similar study and optimized the process parameters to build HY100 steel with the highest relative density. A 65 J/mm3 of energy density resulted in fully dense prints. Mohammadi and Asgari (Mohammadi and

Asgari, 2018) could achieve better surface roughness by changing the process parameters at the builds' surface. A variation of process parameters was introduced for core and contour, and the upskin, downskin parameters were varied to have better surface parameters (See Fig. 1-2). With this technique, the mechanical strength and hardness were addressed in the core, while the surface properties were optimized at the contour.

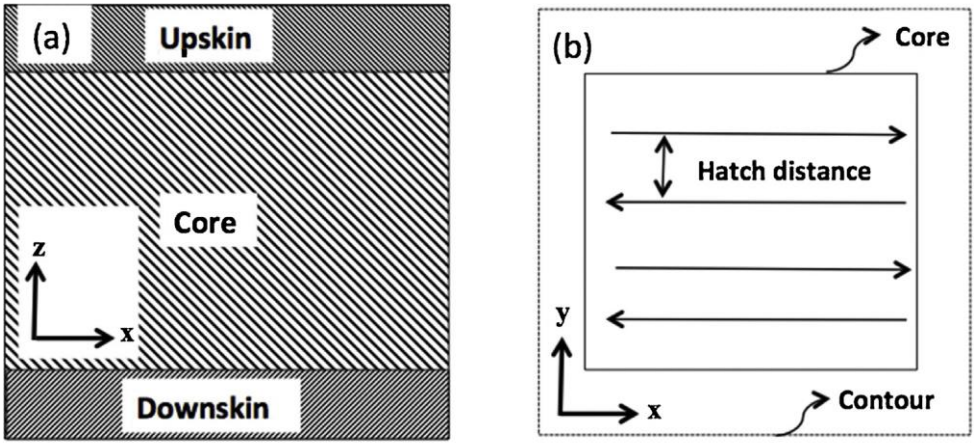

Fig. 1-2 Process parameters defined for core and contour of a build (Mohammadi and Asgari, 2018).

Mutua et al. (Mutua et al., 2018) introduced a process parameter window showing the effect of laser power, scan speed, and energy density. The low energy led to insufficient melting, while too high energy resulted in shrinkage and burnt surface. The results showed a wide range of processing windows to have optimum conditions in terms of relative density and surface quality. In another study performed by Mooney et al. (Mooney et al., 2019), process parameters on the anisotropy of the maraging steel parts were investigated. The scan strategy and the build orientation were considered variables, and the relative density was related to the powder feedstock. The anisotropy was shown to be reduced through heat-treatment. The laser scan strategy was then studied on maraging steel mechanical properties and microstructure (Bhardwaj et al., 2018). The scanning strategy showed to highly affect the texture and grain growth through the solidification process.

1.3.2.2 Porosity and relative density

As mentioned in the previous section, the porosity is the first obstacle that the additive parts need to overcome to be able to be compared with the conventional processes. Various studies have been conducted to relate the porosity to the process parameters and investigate ways they occur through the additive process. A set of process parameters and scan strategy showed by Aboulkhair et al. (Aboulkhair et al., 2014) to reach 99.8% dense AlSi10Mg. The scanning speed showed to determine the pore type. Lower scan speed led to keyhole pores, while lack of fusion resulted from higher speeds. The porosity formed due to the hatch spacing was investigated for Ti-6Al-4V (Gong et al., 2014) and showed that high overlaps led to decreasing the melt-pool depth, resulting in unmelted formation powder (See Fig. 1-3 and Fig. 1-4).

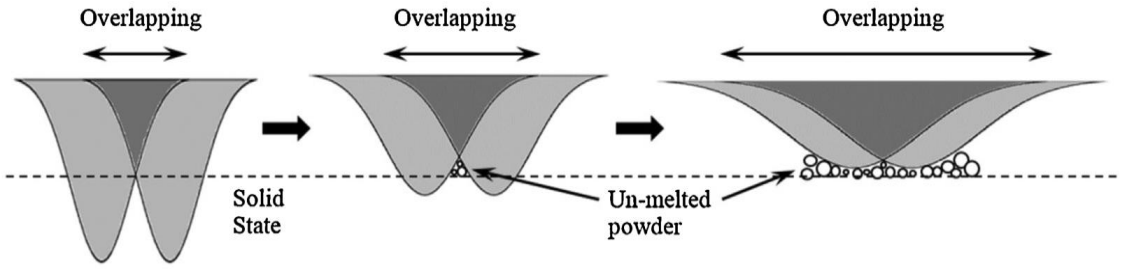

Fig. 1-3 Porosity due to overlapping (Gong, et al., 2014)

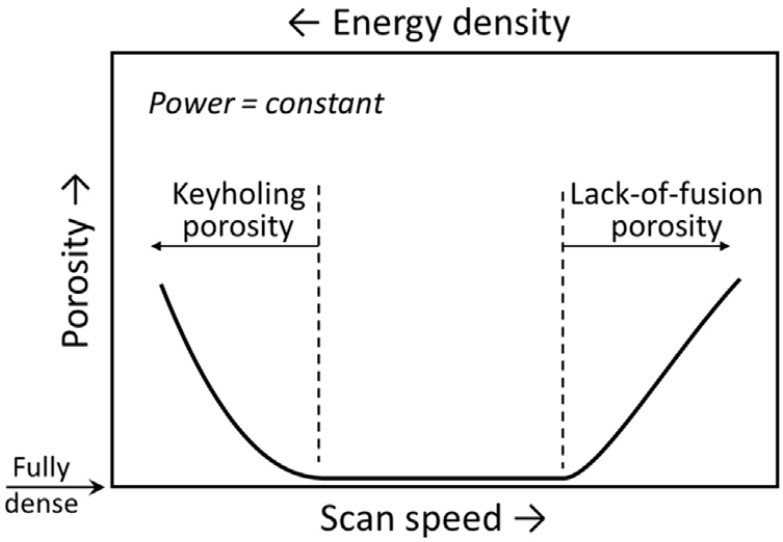

Fig. 1-4 Porosity versus scan speed (Gong, et al., 2014)

The fatigue behaviour of 630 stainless steel was investigated, and the fatigue strength was recognized to be lower compared to conventionally produced samples due to the porosity involved in additive manufacturing (Akita et al., 2016). The energy density was then studied as a measure to design parameters. Low, medium and high energy density values led to different balling regimes, continuous tracks, and keyholes, respectively (Bertoli et al., 2017). A spatial model was developed to predict the porosity as a laser power function and scan speed and validated on 17-4 PH stainless steel (Tapia et al., 2016). Another geometry model was also presented by Tang et al. (Tang et al., 2017) to show the relationship between the porosity and process parameters. The volume fraction of unmelted powder is predicted in this model based on the geometry of melt-pools, hatch spacing, and layer thickness.

1.3.2.3 Building direction

Another parameter recognized to be affecting the mechanical behaviour of the additive manufactured parts is the building direction. There are multiple reasons for such an effect.

One of them is regarding the residual stresses in various directions. Considering that each layer consists of a fixed thickness, parts built in the horizontal direction are made of fewer stacks, while vertically printed samples are exposed to higher layers. Each layer can be considered a heat load impulsively applied to the material through the laser beam. These heat loads apply residual stresses each, and as a result, a vertical build is experiencing higher residual stresses than the horizontal ones. In a study conducted by Croccolo et al. (Croccolo et al., 2016), the effect of build orientation was investigated on the maraging steel's fatigue behaviour. They concluded that the building direction has a low effect on fatigue strength. However, Kuo et al. (Kuo et al., 2017) studied Ni-base alloys' creep properties and found a low creep life and ductility in the horizontal builds. The main reason for such behaviour was then related to the intermetallic precipitations grown in a specific orientation. The grain orientation can be considered then as another reason for different mechanical properties in different build directions. Tan et al. (Tan et al., 2018) investigated the mechanical properties of maraging steel build in different orientations and concluded that it could be reduced effectively through the heat-treatment process despite a difference in the mechanical properties. In a similar study, plastic anisotropy was investigated, and an optimized heat-treatment plan on reducing the strain anisotropy was suggested (Mooney et al., 2019). In another study conducted by Hadadzadeh et al. (Hadadzadeh et al., 2018), AlSi10Mg was built in different build directions, and the microstructure evolution was examined. The horizontal direction showed to induce more equiaxed grains while columnar grain was grown in the vertical builds (See Fig. 1-5). This transition from equiaxed to columnar was related to the solidification process due to local thermal boundary conditions.

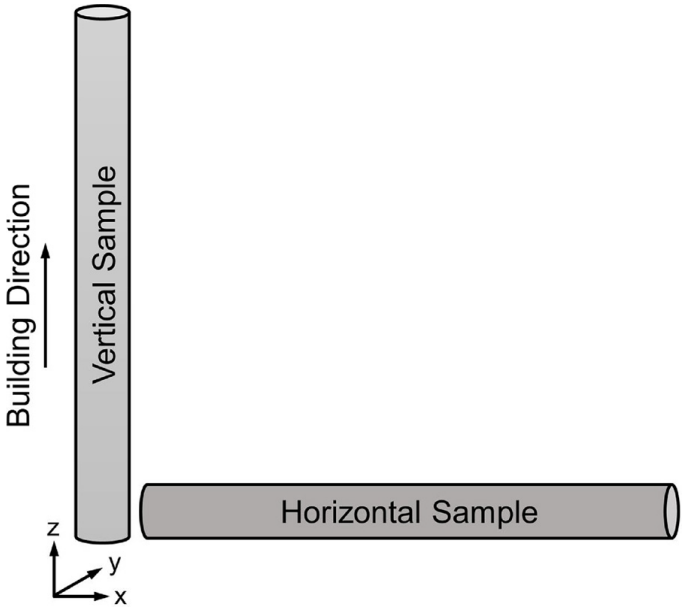

Fig. 1-5 Horizontal vs vertical build in the additive manufacturing process (Hadadzadeh et al., 2018).

1.3.3 Pre and post-process parameters

1.3.3.1 Powder metallurgy and recoating mechanism

Metal powder is the input to the powder bed fusion technique, and consequently, the powder properties can directly affect the manufactured parts. The powder and packing density spread can determine other process parameters such as powder layer thickness and the recoater mechanism (Snow et al., 2019). Powder spreadability has been studied recently, and three quantitive parameters were recognized to be (1) the powder deposition rate, (2) the avalanching angle rate change, and (3) the covered percentage of the build plate. Another powder property is recognized to be the particle size, as well as adhesion. A model was presented and concluded that with very fine particle size, the gravity force is dominated by the cohesion, and consequently, the powder quality reduces in terms of spreadability. The layer thickness was then recommended to be over two to three times the maximum powder particle size (Meier et al., 2019). Different powders are used in the

powder bed fusion technique, and the gas atomized powder is showing better properties due to its fine size and spherical morphology (Joly et al., 1974).

Powder deposition mechanisms were studied by Schueren et al. (Van der Schueren et al., 1995), showing that powder properties affect the deposition mechanism's selection. Scraper blade deposits a layer of powder by sweeping over the build plate. A counter-rolling cylinder rolls and moves the powder to deposit over the build plate. The third method is to use a slot feeder in which the powder is deposited incrementally over the build plate (See Fig. 1-6). The effect of using a ceramic recoater blade is then investigated by Dana et al. (Dana et al., 2019). The build plate's vibration was considered a considerable disadvantage, while a soft recoater would not spread the powder particles effectively over the build plate.

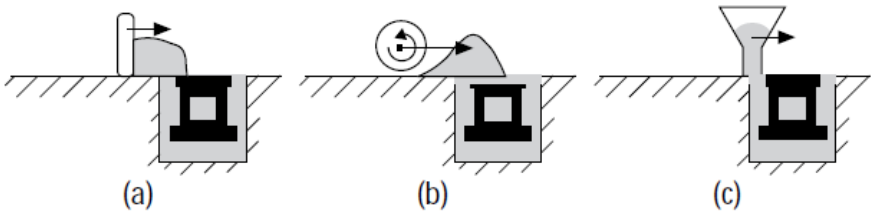

Fig. 1-6 Three deposition methods (a) scraper blade (b) counter rolling cylinder, (c) slot feeder (Van der Schueren et al., 1995)

1.3.3.2 Heat-treatment

As discussed earlier, maraging steel is first introduced by its martensitic structure due to ageing (Sha et al., 2009). The mechanical strength of 18Ni-300 maraging steel can increase from around 1200 Mpa in the as-built additive manufactured samples up to 2000 MPa. This vast increase is mainly due to intermetallic precipitations of Ni, Ti and Mo alloy elements available in the material composition. Fine intercellular spacing is also recognized as a reason for the higher strength of additively manufactured maraging steel

than conventionally produced ones (Kempen et al., 2011). The payoff for increased strength is a reduction of ductility in the aged samples. The heat-treatment was studied and shown to transform a portion of martensite into austenite (Casati et al., 2016). However, the same study suggested that the phase transformation still had a lower effect than the precipitation hardening.

Precipitations were observed to form during the additive manufacturing of 19Ni maraging steel in an intrinsic heat-treatment process (Kürnsteiner et al., 2017). This new method was suggested to combine the manufacturing and heat-treatment processes in order to reach a high density of precipitations without further ageing. The ageing of 18Ni-300 maraging steel was then investigated, and the solution treatment showed to result in an entirely martensitic structure after the ageing process (Mutua et al., 2018).

1.3.4 Mechanical properties

After the relative density of additive parts reaches the conventionally manufactured ones, the first measure to compare the performance is mechanical properties. The additive manufacturing technique has tried to build parts comparable to older techniques. In some cases, it has also been successful in producing parts with higher properties. One example of higher mechanical properties is the AlSi10Mg studied by Asgari et al. (Asgari et al., 2017). Strength and ductility were investigated to be much higher in the additive build compared to die-cast ones.

Studies on maraging steel show that different build directions and scanning strategies can result in various strengths and ductility in the as-built cases (Becker et al., 2016). Different process parameters result in a range of strength from 950-1200 MPa and ductility from 8.3-13.5%. By applying the heat-treatment, strength increases to 1840-2300 MPa,

and the elongation drops to 2-7%. However, a comparison between additive manufacturing and wrought products is more complicated. Increased strength results in reduced ductility in the as-built case, while the aged samples show similar strength and lower ductilities (Becker et al., 2016) (Dehgahi et al., 2020).

Mechanical strength of maraging steels is attributed to the strength of lath martensite σ_{Mart}, intermetallic precipitations σ_p, and solid solution hardening σ_{ss} as shown in Eq. (2.3) (Galindo-Nava et al., 2016):

$$\sigma_Y = \sigma_{Mart} + \sigma_P + \sigma_{ss} \qquad (2.3)$$

However, the mechanisms mentioned above are governed by the dislocation density, alloying elements, and grain size (Galindo-Nava et al., 2016). The reverted austenite phase has shown not to affect the aged samples' mechanical properties (Casati et al., 2016). Different heat-treatment time is studied by Mooney et al. (Mooney et al., 2019) to investigate the mechanical properties of additively manufactured maraging steels, and scan rotation degree has been recognized to excessively affect mechanical properties. Variation of ageing time and temperature on the hardness is also studied by Mutua et al. (Mutua et al., 2018). Tensile properties of AM maraging steel are studied for different build orientations by Suryawanshi et al. (Suryawanshi et al., 2017), and slightly different properties in different build directions were reported. Mechanical properties of wire arc manufactured maraging steels were also studied, and similar properties were reported with wrought material (Xu et al., 2018), while mechanical properties showed to improve after cold rolling (Xu et al., 2019).

1.3.5 Microstructure

The microstructure of the additive manufactured parts has been studied via various microscopy techniques. Scanning electron microscopy (SEM) is typically used to investigate the cellular structure and possible inclusions, while transmission electron microscopy (TEM) studies the microstructure in higher magnifications to depict fine precipitations. The electron backscattered diffraction technique is also a very useful tool to investigate grain orientations and texture.

Using the SEM technique, Ti and Al inclusions were depicted in the AM maraging steel by Thijs et al. (Thijs et al., 2011). By using a finite element model, the solidification process was predicted. The grains were shown to grow along with the maximum heat flux (Wang et al., 2016). The cellular structure was predicted to form at the melt-pools' core while the columnar dendrites formed at the melt-pool boundaries (Tan et al., 2017). The models agreed with the micrography presented in various studies (Tan et al., 2018), (Suryawanshi et al., 2017) and (Takata et al., 2018).

Fractography of the as-built and aged maraging steel samples via the SEM graphs were shown to form dimples and inter-, trans-granular fracture, respectively (Kempen, et al., 2011). Failure progression in various tensile deformation stages was studied, and cavity and unmelted powder were depicted in the SEM micrographs by Kucerova et al. (Kučerová et al., 2019).

Dislocations were depicted in the bright-field TEM graphs, while the STEM-EDX showed element distribution maps along with the microstructure (Tan et al., 2017). Lath martensite was also depicted in the maraging steel studies, and the precipitate morphologies were investigated by Li et al. (Li et al., 2017). The austenite phase was observed in line-

tracks in the STEM-BF by Dehgahi et al. (Dehgahi et al., 2020), which was in agreement with the formation of reverted austenite between the martensite laths (Galindo-Nava et al., 2016). Using the STEM-BF maps, Hadadzadeh et al. (Hadadzadeh et al., 2019) recognized a hierarchical microstructure affecting the dynamic behaviour of AlSi10Mg.

Grains were observed in the EBSD inverse pole figure (IPF) maps to orient perpendicular to the melt-pool boundaries (Suryawanshi et al., 2017). High-, low- angle grain boundaries (HAGB/LAGB) were correlated to the local misorientation in a study on additively manufactured stainless steel (Wang et al., 2018). The maraging steel texture affecting the impact properties were investigated by Masoumi et al. (Masoumi et al., 2016), and the fibre textures along with the bcc lattice structure normal directions such as {112}, {113}, and {110} were showing increased toughness.

1.3.6 Crystal structure

Crystal structure of maraging steels mainly consists of body-centred cube (bcc) crystals in the form of martensite ($\acute{\alpha}$) phase, and face-centred cube (fcc) crystal of austenite (γ) phase. The fcc phase is a packed structure compared to bcc. Thus, a deformation can result in phase transformation from martensite to austenite. The martensite forms in a diffusionless transformation, while austenite forms in a diffusion-controlled process (Floreen, 1968). The metastable phase diagram of Fe-Ni is shown in Fig. 1-7. Heating 18Ni maraging steel from room temperature, the material goes through austenite reversion. At austenite formation start temperature (A_s), the austenite fraction is 10% and increases to 90% by heating to austenite formation finish (A_f) temperature. By cooling the material, transformation starts at a relatively cooler temperature (M_s). Martensite forms in a diffusionless transformation process, and by reaching (M_f), 90% transformation has

occurred. The martensite and austenite start and end temperatures are shown in Table 1.1 (Dos Reis et al., 2015).

Table 1.1 Martensite and austenite start and end temperatures for 18Ni-maraging steel (Dos Reis, et al., 2015)

	M_s	M_f	A_s	A_f
Temperature (°C)	194	62	623	801

As a result, it is essential to consider the evolution of microstructure regarding its phase change during the manufacturing process. It is known that the material goes through a series of reheating and cooling with very high heating and cooling rates in the additive process. Thus, a different phase fraction in the additively manufactured maraging steel compared to conventional builds is expected, as observed in the literature (Xu et al., 2018). Besides, the ageing process increases the austenite through austenite reversion, which has been reported (Xu et al., 2018) (Suryawanshi et al., 2017) (Tan et al., 2017) previously.

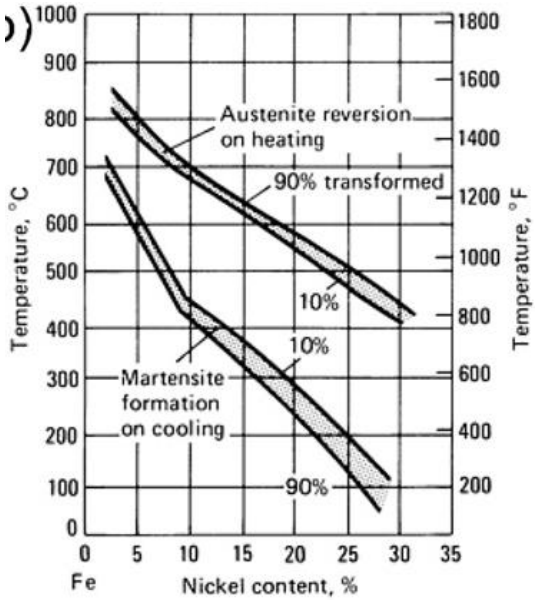

Fig. 1-7 Fe-Ni system metastable phase diagram (Tan et al., 2017).

It is noteworthy that austenite has a lower hardness and is more prone to deform than martensite under tensile stress. Two mechanisms introduced to explain the deformation-induced phase transformation are known as Greenwood-Johnson and Magee mechanisms. In the former mechanism, transformation occurs due to the difference between the packing density of two crystal structures. In the austenite-martensite dual-phase structure, the austenite transforms into martensite during deformation so that the structure can expand and compensate for the deformation. In the latter mechanism, plastic deformation leads to the formation of martensitic variants in preferred orientations (Leblond et al., 1989) and (Taleb et al., 2003).

In order to investigate the austenite and martensite phases, Shakerin et al. (Shakerin et al., 2020) conducted an X-ray diffraction (XRD) test to study the interface of maraging steel-H13 bimetal samples. Dehgahi et al. (Dehgahi et al., 2020) used the same technique to investigate the martensite/austenite phase fractions of additively manufactured C300 maraging steel with high and low titanium. A higher austenite fraction in the high Ti maraging steel was reported. Superior mechanical properties were associated with the retained austenite in the horizontal builds as well. In another study, texture evolution was studied using the XRD technique in C300 maraging steel with high and low Ti content, and the TRIP effect was investigated (Dehgahi et al., 2021).

1.4 Gap of knowledge

In previous sections, different aspects of the additive manufacturing process were presented. Despite various studies conducted so far on 18Ni-300 maraging steels, some fields are still overlooked, which were covered in the current thesis.

Multiple studies on the mechanical properties and microstructure of additively manufactured 18Ni-300 maraging steel showed that the additive technique can produce parts with comparable mechanical properties to conventional techniques. Different process parameters have been investigated, and the effect of each had been reported (Bai et al., 2017) (Becker et al., 2016) (Bhardwaj et al., 2018) (Casalino et al., 2015) (Mooney et al., 2019) (Thijs et al., 2011). However, the powder layer thickness was overlooked in the studies mentioned above, and a comparison of mechanical properties and microstructure between builds with lower and higher powder layer thickness was missing. The first paper in chapter two covers this part, starting with a study on the powder morphology and comparing the mechanical behaviour of builds with 40- and 50-µm powder layers.

Despite the vast research on the AM-18Ni maraging steel's mechanical properties in the literature (Dehgahi et al., 2020), (Kempen et al., 2011), (Rajkumar et al., 2014), (Suryawanshi et al., 2017), (Takata et al., 2018), and (Tan et al., 2017), the author found the necessity to investigate such material's deformation behaviour. The second paper's subject in chapter three is a comprehensive study on the deformation and phase transformation of the 18Ni-300 maraging steel through a quasi-static uniaxial tensile test. This paper sheds light on the microstructure evolution throughout the additive process as well as the deformation process.

Comprehensive studies have been conducted previously on the effect of building direction and heat-treatment on AM-18Ni maraging steels (Mutua et al., 2018), (Croccolo et al., 2016), (Tan et al., 2018), (Mooney et al., 2019), (Casati et al., 2016), and (Meneghetti et al., 2017). However, the hierarchical microstructure has not been recognized before. The third paper in chapter four aimed to investigate the microstructural differences in different building directions in different scales. Besides, phase transformation studied in chapter three was extended to different building directions and the ageing process in this chapter.

The fifth chapter was formed in a short communication paper discussing the effect of the recoater blade. Despite multiple studies on additive parts produced with a hard ceramic recoater (Dos Reis et al., 2015), (Saka et al., 2015), (Jägle et al., 2017), (Kučerová et al., 2019), (Jägle et al., 2014), and (Fortunato et al., 2018), using a soft recoater has not been investigated in the literature. Mechanical properties and microstructure of 18Ni-300 maraging steels with hard and soft recoater blades are presented in this chapter.

1.5 Contributions

Different chapters of this thesis were written in collaboration with different research teams. For clarification, the contribution of the author of this thesis is specified in each paper separately.

Paper one in chapter two was written in collaboration with Sajad Shakerin, Dr. Amir Hadadzadeh, Dr. Babak Shalchi Amirkhiz, and Dr. Mohsen Mohammadi. The first author (author of this thesis) conducted all the experimental tests except the TEM and XRD studies. Moreover, the author of this thesis interpreted and wrote the manuscript of the paper. The co-authors helped with the interpretation of the data and TEM analysis.

The second paper in chapter three was written in collaboration with M.H. Ghoncheh, Dr. Mehdi Sanjari, Dr. Hadi Pirgazi, Dr. Babak Shalchi Amirkhiz, Dr. Leo Kestens, and Dr. Mohsen Mohammadi. The first author (author of this thesis) conducted all the experimental tests except the TEM and XRD studies. The author of the thesis interpreted and wrote the manuscript of the paper, and the co-authors helped with the interpretation of the data and TEM and EBSD analysis.

The third paper in chapter four was written in collaboration with Dr. Hadi Pirgazi, M.H. Ghoncheh, Dr. Mehdi Sanjari, Dr. Babak Shalchi Amirkhiz, Dr. Leo Kestens, and Dr. Mohsen Mohammadi. The first author (author of this thesis) conducted all the experimental tests except the TEM and XRD studies and the numerical modelling. The first author interpreted and wrote the manuscript of the paper. The co-authors helped with the interpretation of the data as well as the TEM, EBSD and numerical modelling.

The fourth and last paper in chapter five was written in collaboration with M.H. Ghoncheh and Dr. Mohsen Mohammadi. The author of the thesis conducted all the studies

except the XRD tests and interpreted and wrote the paper's manuscript. The co-authors helped with the interpretation of the data.

1.6 Comments on the papers

Studies in this thesis were conducted in different times and facilities. The following comments are added to help the reader have more consistent insight into the work.

In chapter two, Fig. 2-15(a,b) shows the EBSD study on deformed samples. The map is showing the grains while the colours are randomly selected and do not represent the orientations.

Studies in chapters two, three, four, and five show texture in the pole figure maps and orientation distribution functions. It is worth mentioning that <100> texture was measured normal to the building direction in all cases. In other words, the grains were elongated along the building direction. The <111> texture was also measured from the same reference system. On the other hand, the <110> texture measured in the deformed cases was depicted normal to the loading direction.

In chapter three, Fig 3-5(g) shows the key components for the ODF maps. The key component is depicted from a study on rolled steel in which the reference system is based on the rolling and transverse directions. Despite the differences between rolling and the additive manufacturing process, the map helps the reader better understand the fibre textures. The θ-fibre and γ-fibre in rolled steel are similar in <100>-fibre and <111>-fibre normal to building direction in additive specimens. Similarly, the α-fibre defined in the rolled steel is similar to the <110>-fibre normal to the additive parts' load direction.

The 67° layer rotation in the additive manufacturing process is one of the additive technique's scanning strategies. The laser-track rotates 67° every layer in this method resulting in more consistent melt-pools with fewer defects. All samples in the current study were built using this scanning strategy.

The SEM micrographs representing the microstructure were studied from different areas and different layers. The images used in this thesis are the typical ones showing similar features to most of the graphs depicted from different samples.

The depth measurements were conducted on cubic samples built with various process parameters discussed in chapters two, four and five. The additive samples' repeatability was investigated on the top layer for three samples, and the results were identical. Then, each test of hardness and porosity was conducted on one test specimen through the depth. The hardness was repeated at least three times, while the porosity was conducted on a minimum of fifteen images from various surface areas.

Deformation studies were conducted on the undeformed and deformed specimens in all four studies in this thesis. The undeformed specimen was taken off from the end of the uniaxial tensile specimen beyond the tensile grip. The deformed specimen was picked from the fracture area. In chapter three, an area far from the fracture inside the gauge length was also studied, which showed similar behaviour to the undeformed area. The three specimens were designated as zones A, B and C, as shown in Fig. 3-1 in chapter three.

1.7 Study outline

A comprehensive study on the mechanical properties and microstructure of additively manufactured 18Ni-300 maraging steel (MS1) was performed in this research. A study on the variation of mechanical properties through the depth of samples is presented in this research. The effects of process parameters, including the recoater blade type, powder layer thickness, and build orientation and the interaction of these parameters on the mechanical properties and microstructure of DMLS-MS1, were studied. Finally, the combination of a heat treatment cycle as a post-processing procedure with AM process parameters is investigated in this work.

Initially, the characteristics of MS1 feedstock powder, including shape, size, and morphology, as the DMLS process input were studied. Solid cubes and bars were then additively manufactured to study the microstructure and mechanical properties of DMLS-MS1. In addition, solid cubes were then polished layer by layer, and the variation of relative density and hardness were measured through the depth of the printed samples. Phase analysis was conducted using X-ray diffraction techniques both on the MS1 powder and all printed samples to investigate the phase transformation. Several uniaxial tensile tests were performed on the MS1 bars to study the effects of different process parameters on the mechanical properties. The deformation and fracture mechanisms were studied through SEM, EBSD, and TEM techniques to investigate the effect of process parameters on the mechanical behavior of the additively manufactured material.

This thesis is presented in a paper-based format in 6 chapters. Chapter 1 contains an introduction to additive manufacturing as well as the maraging steel material. Chapter 2 presents a study on powder characterization and the effect of powder layer thickness on

mechanical properties and microstructure. In chapter 3, a more in-depth study is presented on the deformation behavior of AM material with various powder layer thicknesses. Chapter 4 discusses the building orientation as well as the heat treatment effects on maraging steel. Chapter 5 shows the effect of using a soft recoater blade in the additive manufacturing process. Finally, in chapter 6, this study is summed and concluded.

1.8 Contribution to mechanical engineering

The main contribution to mechanical engineering in this research is studying the effect of the additive manufacturing process parameters on maraging steel's mechanical properties. On the macroscopic scale, the strength, ductility, elasticity, hardness, and porosity are studied for various manufacturing parameters. On the microscopic scale, throughout different analytical techniques, including OM, SEM, EBSD, XRD, and TEM, the strengthening mechanisms along with the deformation and fracture mechanisms are studied for the same variation of manufacturing parameters.

1.9 Hypothesis

The result of this research might be used as a guide for mechanical engineers to be able to have an efficient design procedure to use AM techniques. Increasing the production speed by increasing the powder layer thickness is the first step in increasing AM processes' productivity. In order to examine this hypothesis, a study is conducted on the variation of powder layer thickness affecting mechanical properties and microstructure.

Being able to print an additive part in the horizontal direction with better mechanical properties can increase the production speed while minimizing the metal powder consumption during the manufacturing process at the same time. A series of experiments are designed to investigate the effect of building direction on mechanical properties and microstructure of additively manufactured samples.

Changing the recoater blade type is expected to change the powder distribution pattern on the building platform. Using soft versus hard recoater blades are examined to study the properties of the manufactured maraging steels.

The effect of heat treatment is dominant among all the parameters mentioned above. The heat treatment is expected to reduce the additively manufactured part's anisotropy and give the studied material superior tensile properties close to 2 GPa. This hypothesis is examined through experiments with different process parameters.

1.10 Funding

This project was funded by the Natural Science and Engineering Research Council of Canada with grant number RGPIN-2016-04221, the New Brunswick Innovation Foundation with grant number RIF2017-071, Atlantic Canada Opportunities Agency (ACOA)-Atlantic Innovation Fund (AIF) with project number 210414, and Mitacs Accelerate Program with grant number IT10669.

1.11 References

Aboulkhair N. T. [et al.] Reducing porosity in AlSi10Mg parts processed by selective laser melting [Journal] // Additive Manufacturing. - 2014. - Vol. 1. - pp. 77-86.

Agarwala M. [et al.] Direct selective laser sintering of metals [Journal] // Rapid Prototyping Journal. - 1995.

Akita M. [et al.] Defect-dominated fatigue behavior in type 630 stainless steel fabricated by selective laser melting [Journal] // Materials Science and Engineering: A. - 2016. - Vol. 666. - pp. 19-26.

Asgari H. [et al.] On microstructure and mechanical properties of additively manufactured AlSi10Mg_200C using recycled powder [Journal] // Materials Science and Engineering: A. - 2017. - Vol. 707. - pp. 148-158.

Atzeni E. and Salmi A. Economics of additive manufacturing for end-usable metal parts [Journal] // The International Journal of Advanced Manufacturing Technology. - 2012. - Vols. 62(9-12). - pp. 1147-1155.

Bai Y. [et al.] Influence mechanism of parameters process and mechanical properties evolution mechanism of maraging steel 300 by selective laser melting [Journal] // Materials Science and Engineering: A. - 2017. - Vol. 703. - pp. 116-123.

Becker T. H. and Dimitrov D. The achievable mechanical properties of SLM produced Maraging Steel 300 components [Journal] // Rapid Prototyping Journal. - 2016.

Belyakov L. N., Nikol'skaya V. L. and Ryzhak S. S. The α→ γ transformation in maraging steel N18K9M5T [Journal] // Metal Science and Heat Treatment. - 1968. - Vol. 10(6). - pp. 438-442.

Bertoli U. S. [et al.] On the limitations of volumetric energy density as a design parameter for selective laser melting [Journal] // Materials & Design. - 2017. - Vol. 113. - pp. 331-340.

Bhardwaj T. and Shukla M. Effect of laser scanning strategies on texture, physical and mechanical properties of laser sintered maraging steel [Journal] // Materials Science and Engineering: A. - 2018. - Vol. 734. - pp. 102-109.

Campanelli S. L., Contuzzi N. and Ludovico A. D. Manufacturing of 18 Ni Marage 300 steel samples by selective laser melting [Journal] // Advanced Materials Research. - 2010. - Vol. 83. - pp. 850-857.

Casalino G. [et al.] Experimental investigation and statistical optimisation of the selective laser melting process of a maraging steel [Journal] // Optics & Laser Technology. - 2015. - Vol. 65. - pp. 151-158.

Casati R. [et al.] Aging behaviour and mechanical performance of 18-Ni 300 steel processed by selective laser melting [Journal] // Metals. - 2016. - Vol. 6(9). - p. 218.

Croccolo D. [et al.] Influence of the build orientation on the fatigue strength of EOS maraging steel produced by additive metal machine [Journal] // Fatigue & Fracture of Engineering Materials & Structures. - 2016. - Vol. 39(5). - pp. 637-647.

Cyr E. [et al.] Fracture behaviour of additively manufactured MS1-H13 hybrid hard steels [Journal] // Materials Letters. - 2018. - Vol. 212. - pp. 174-177.

Daňa M., Zetková I. and Hanzl P. The Influence of a Ceramic Recoater Blade on 3D Printing using Direct Metal Laser Sintering [Journal]. - 2019.

Dehgahi S. [et al.] Concurrent improvement of strength and ductility in heat-treated C300 maraging steels produced by laser powder bed fusion technique [Journal] // Additive Manufacturing. - 2021. - Vol. 39. - p. 101847.

Dehgahi S. [et al.] The role of titanium on the microstructure and mechanical properties of additively manufactured C300 maraging steels [Journal] // Materials & Design. - 2020. - Vol. 194. - p. 108965.

Dilip J. J. S. [et al.] Selective laser melting of HY100 steel: process parameters,

microstructure and mechanical properties [Journal] // Additive Manufacturing. - 2017. - Vol. 13. - pp. 49-60.

Ding J. [et al.] Thermo-mechanical analysis of Wire and Arc Additive Layer Manufacturing process on large multi-layer parts [Journal] // Computational Materials Science. - 2011. - Vol. 50(12). - pp. 3315-3322.

Dos Reis A. G. [et al.] High-temperature creep resistance and effects on the austenite reversion and precipitation of 18 Ni (300) maraging steel [Journal] // Materials Characterization. - 2015. - Vol. 107. - pp. 350-357.

Floreen S. The physical metallurgy of maraging steels [Book]. - [s.l.] : Metallurgical Reviews, 1968. - 13(1), 115-128.

Fortunato A. [et al.] Milling of maraging steel components produced by selective laser melting [Journal] // The International Journal of Advanced Manufacturing Technology. - 2018. - Vols. 94(5-8). - pp. 1895-1902.

Galindo-Nava E. I., Rainforth W. M. and Rivera-Díaz-del-Castillo P. E. J. Predicting microstructure and strength of maraging steels: Elemental optimisation [Journal] // Acta Materialia. - 2016. - Vol. 117. - pp. 270-285.

Gong H. [et al.] Analysis of defect generation in Ti–6Al–4V parts made using powder bed fusion additive manufacturing processes [Journal] // Additive Manufacturing. - 2014. - Vol. 1. - pp. 87-98.

Gu D. D. [et al.] Laser additive manufacturing of metallic components: materials, processes and mechanisms [Journal] // International materials reviews. - 2012. - Vol. 57(3). - pp. 133-164.

Hadadzadeh A. [et al.] Columnar to equiaxed transition during direct metal laser sintering of AlSi10Mg alloy: effect of building direction [Journal] // Additive Manufacturing. - 2018. - Vol. 23. - pp. 121-131.

Hadadzadeh A. [et al.] Role of hierarchical microstructure of additively manufactured AlSi10Mg on dynamic loading behavior [Journal] // Additive Manufacturing. - 2019. - Vol. 28. - pp. 1-13.

Huang Z. [et al.] A high temperature mechanical study on PH 13-8 Mo maraging steel [Journal] // Materials Science and Engineering: A. - 2016. - Vol. 651. - pp. 574-582.

Jägle E. A. [et al.] Comparison of maraging steel micro-and nanostructure produced conventionally and by laser additive manufacturing [Journal] // Materials. - 2017. - Vol. 10(1). - p. 8.

Jägle E. A. [et al.] Precipitation and austenite reversion behavior of a maraging steel produced by selective laser melting [Journal] // Journal of Materials Research. - 2014. - Vol. 29(17). - p. 2072.

Joly P. A. and Mehrabian R. Complex alloy powders produced by different atomization techniques: relationship between heat flow and structure [Journal] // Journal of materials science. - 1974. - Vol. 9(9). - pp. 1446-1455.

Kempen K. [et al.] Microstructure and mechanical properties of Selective Laser Melted 18Ni-300 steel [Journal] // Physics Procedia. - 2011. - Vol. 12. - pp. 255-263.

Khajavi S. H., Partanen J. and Holmström J. Additive manufacturing in the spare parts supply chain [Journal] // Computers in industry. - 2014. - Vol. 65(1). - pp. 50-63.

Kodama H. Automatic method for fabricating a three-dimensional plastic model with photo-hardening polymer [Journal] // Review of scientific instruments. - 1981. - Vol. 52(11). - pp. 1770-1773.

Kruth J. P. [et al.] Basic powder metallurgical aspects in selective metal powder sintering [Journal] // CIRP annals. - 1996. - Vol. 45(1). - pp. 183-186.

Kruth J. P. Material incress manufacturing by rapid prototyping techniques [Journal] // CIRP annals. - 1991. - Vol. 40(2). - pp. 603-614.

Kruth J. P., Leu M. C. and Nakagawa T. Progress in additive manufacturing and rapid prototyping [Journal] // CIRP Annals-Manufacturing Technology. - 1998. - Vol. 47(2). - pp. 525-540.

Kučerová L. [et al.] Microstructural characterisation and in-situ straining of additive-manufactured X3NiCoMoTi 18-9-5 maraging steel [Journal] // Materials Science and Engineering: A. - 2019. - Vol. 750. - pp. 70-80.

Kuo Y. L., Horikawa S. and Kakehi K. Effects of build direction and heat treatment on creep properties of Ni-base superalloy built up by additive manufacturing [Journal] // Scripta Materialia. - 2017. - Vol. 129. - pp. 74-78.

Kürnsteiner P. [et al.] Massive nanoprecipitation in an Fe-19Ni-xAl maraging steel triggered by the intrinsic heat treatment during laser metal deposition [Journal] // Acta Materialia. - 2017. - Vol. 129. - pp. 52-60.

Leblond J. B., Devaux J. and Devaux J. C. Mathematical modelling of transformation plasticity in steels I: Case of ideal-plastic phases [Journal] // International journal of plasticity. - 1989. - Vol. 5(6). - pp. 551-572.

Li K. [et al.] The role of copper in microstructures and mechanical properties of laser-welded Fe-19Ni-3Mo-1.5 Ti maraging steel joint [Journal] // Materials Science and Engineering: A. - 2017. - Vol. 681. - pp. 41-49.

Li Y. [et al.] A new 1.9 GPa maraging stainless steel strengthened by multiple precipitating species [Journal] // Materials & Design. - 2015. - Vol. 82. - pp. 56-63.

Masoumi M. [et al.] Effect of microstructure and crystallographic texture on the Charpy impact test for maraging 300 steel [Journal] // Materials Characterization. - 2016. - Vol. 120. - pp. 203-209.

Meier C. [et al.] Critical influences of particle size and adhesion on the powder layer uniformity in metal additive manufacturing [Journal] // Journal of Materials

Processing Technology. - 2019. - Vol. 266. - pp. 484-501.

Meneghetti G. [et al.] Influence of build orientation on static and axial fatigue properties of maraging steel specimens produced by additive manufacturing [Journal] // Procedia Structural Integrity. - 2017. - Vol. 7. - pp. 149-157.

Mohammadi M. and Asgari H. Achieving low surface roughness AlSi10Mg_200C parts using direct metal laser sintering [Journal] // Additive Manufacturing. - 2018. - Vol. 20. - pp. 23-32.

Mooney B. [et al.] Process phenomena influencing the tensile and anisotropic characteristics of additively manufactured maraging steel [Journal] // Materials Science and Engineering: A. - 2019. - Vol. 745. - pp. 115-125.

Mooney B., Kourousis K. I. and Raghavendra R. Plastic anisotropy of additively manufactured maraging steel: Influence of the build orientation and heat treatments [Journal] // Additive Manufacturing. - 2019. - Vol. 25. - pp. 19-31.

Murr L. E. [et al.] Metal fabrication by additive manufacturing using laser and electron beam melting technologies [Journal] // Journal of Materials Science & Technology. - 2012. - Vol. 28(1). - pp. 1-14.

Mutua J. [et al.] Optimization of selective laser melting parameters and influence of post heat treatment on microstructure and mechanical properties of maraging steel [Journal] // Materials & Design. - 2018. - Vol. 139. - pp. 486-497.

Qian F., Sharp J. and Rainforth W. M. Microstructural evolution of Mn-based maraging steels and their influences on mechanical properties [Journal] // Materials Science and Engineering: A. - 2016. - Vol. 674. - pp. 286-298.

Rajkumar V. and Arivazhagan N. Role of pulsed current on metallurgical and mechanical properties of dissimilar metal gas tungsten arc welding of maraging steel to low alloy steel [Journal] // Materials & Design. - 2014. - Vol. 63. - pp. 69-82.

Sakai P. R. [et al.] Comparison of mechanical and microstructural characteristics in maraging 300 steel welded by three different processes: LASER, PLASMA and TIG [Journal] // Procedia Engineering. - 2015. - Vol. 114. - pp. 291-297.

Sha W. [et al.] Tensile and impact properties of low nickel maraging steel [Journal] // Materials Science and Engineering: A. - 2013. - Vol. 587. - pp. 301-303.

Sha W. and Guo Z. Maraging Steels: Modelling of Microstructure, Properties and Applications [Book]. - [s.l.] : Elsevier, 2009.

Sha W., Cerezo A. and Smith G. D. W. Phase chemistry and precipitation reactions in maraging steels: Part I. Introduction and study of Co-containing C-300 steel [Journal] // Metallurgical and Materials Transactions A. - 1993. - Vol. 24(6). - pp. 1221-1232.

Sha W., Cerezo A. and Smith G. D. W. Phase chemistry and precipitation reactions in maraging steels: Part IV. Discussion and conclusions [Journal] // Metallurgical and Materials Transactions A. - 1993. - Vol. 24(6). - pp. 1251-1256.

Shakerin S. [et al.] Additive manufacturing of maraging steel-H13 bimetals using laser powder bed fusion technique [Journal] // Additive Manufacturing. - 2019. - Vol. 29. - p. 100797.

Shakerin S. [et al.] Interface engineering of additively manufactured maraging steel-H13 bimetallic structures [Journal] // Materials Characterization. - 2020. - Vol. 170. - p. 110728.

Snow Z., Martukanitz R. and Joshi S. On the development of powder spreadability metrics and feedstock requirements for powder bed fusion additive manufacturing [Journal] // Additive Manufacturing. - 2019. - Vol. 28. - pp. 78-86.

Sun S. H. [et al.] Electron beam additive manufacturing of Inconel 718 alloy rods: Impact of build direction on microstructure and high-temperature tensile properties [Journal] // Additive Manufacturing. - 2018. - Vol. 23. - pp. 457-470.

Suryawanshi J., Prashanth K. G. and Ramamurty U. Tensile, fracture, and fatigue crack growth properties of a 3D printed maraging steel through selective laser melting [Journal] // Journal of alloys and compounds. - 2017. - Vol. 725. - pp. 355-364.

Takata N. [et al.] Crystallographic features of microstructure in maraging steel fabricated by selective laser melting [Journal] // Metals. - 2018. - Vol. 8(6). - p. 440.

Taleb L. and Sidoroff F. A micromechanical modeling of the Greenwood–Johnson mechanism in transformation induced plasticity [Journal] // International Journal of Plasticity. - 2003. - Vol. 19(10). - pp. 1821-1842.

Tan C. [et al.] Microstructural characterization and properties of selective laser melted maraging steel with different build directions [Journal] // Science and Technology of Advanced Materials. - 2018. - Vol. 19(1). - pp. 746-758.

Tan C. [et al.] Microstructural evolution, nanoprecipitation behavior and mechanical properties of selective laser melted high-performance grade 300 maraging steel [Journal] // Materials & Design. - 2017. - Vol. 134. - pp. 23-34.

Tang M., Pistorius P. C. and Beuth J. L. Prediction of lack-of-fusion porosity for powder bed fusion [Journal] // Additive Manufacturing. - 2017. - Vol. 14. - pp. 39-48.

Tapia G., Elwany A. H. and Sang H. Prediction of porosity in metal-based additive manufacturing using spatial Gaussian process models [Journal] // Additive Manufacturing. - 2016. - Vol. 12. - pp. 282-290.

Thijs L. [et al.] Investigation on the inclusions in maraging steel produced by Selective Laser Melting [Journal] // Innovative Developments in Virtual and Physical Prototyping. - 2011. - pp. 297-304.

Van der Schueren B. and Kruth J. P. Powder deposition in selective metal powder sintering [Journal] // Rapid Prototyping Journal. - 1995.

Vasudevan V. K., Kim S. J. and Wayman C. M. Precipitation reactions and strengthening

behavior in 18 Wt Pct nickel maraging steels [Journal] // Metallurgical Transactions A. - 1990. - Vol. 21(10). - pp. 2655-2668.

Wang D. [et al.] Investigation of crystal growth mechanism during selective laser melting and mechanical property characterization of 316L stainless steel parts [Journal] // Materials & Design. - 2016. - Vol. 100. - pp. 291-299.

Wang Y. M. [et al.] Additively manufactured hierarchical stainless steels with high strength and ductility [Journal] // Nature materials. - 2018. - Vol. 17(1). - pp. 63-71.

Xiong J. [et al.] Heat propagation of circular thin-walled parts fabricated in additive manufacturing using gas metal arc welding [Journal] // Journal of Materials Processing Technology. - 2018. - Vol. 251. - pp. 12-19.

Xu X. [et al.] Improving mechanical properties of wire plus arc additively manufactured maraging steel through plastic deformation enhanced aging response [Journal] // Materials Science and Engineering: A. - 2019. - Vol. 747. - pp. 111-118.

Xu X. [et al.] Microstructural evolution and mechanical properties of maraging steel produced by wire+ arc additive manufacture process [Journal] // Materials Characterization. - 2018. - Vol. 143. - pp. 152-162.

Chapter 2

A trade-off between powder layer thickness and mechanical properties in additively manufactured maraging steels

Abstract

In this paper, a comprehensive study on the microstructure and mechanical properties of an additively manufactured 18Ni-300 maraging steel (with the brand name MS1), fabricated through the laser-powder bed fusion (LPBF) technique is presented. The influence of powder layer thickness and the characteristics of feedstock powder as the input in the LPBF process is investigated on the microstructure and mechanical properties of solid cubes and cylindrical rods. Relative density and hardness are measured through the depth of the manufactured cubes. The study of porosity and hardness through the depth of LPBF-MS1 cubes proves homogeneous properties in the core of the material in comparison with more heterogeneous properties closer to the subsurface layers. X-ray diffraction techniques both on the powder and the as-built samples are then performed to identify phases in the fabricated samples. A correlation between lower austenite content and higher strength is observed for the tensile samples manufactured with lower powder layer thickness. Texture analysis shows a directional grain growth along the building direction resulting in a weak texture, while the material induces a stronger texture with an increased amount of austenite after the deformation. Studying the effects of powder layer thickness shows slightly lower strength and ductility for the samples manufactured with higher powder layer thickness, while the energy consumption, as well as the manufacturing time, are reduced.

Keywords: Maraging steel; laser-powder bed fusion; microstructure; powder layer thickness; mechanical properties.

2.1 Introduction

For many years, manufacturing methods were restricted to conventional processes such as casting, metal forming, welding, etc to develop the final product from an initial shape. A new method has recently attracted the attention of many researchers and engineers called additive manufacturing (AM). This family of manufacturing methods, in general, refers to procedures by which 3D objects are formed layer by layer from CAD models (Asgari, et al., 2017), (Kruth, 1991), (Kodama, 1981), (Kruth, et al., 1998), and (Hadadzadeh, et al., 2019). Of particular interest in this contribution is metal additive manufacturing (MAM), where metal powder or filament is fused using different energy sources, including laser or electron beam (Gu, et al., 2012), (Van der Schueren, et al., 1995), and (Kruth, et al., 1996). One of the main uncertainties with the AM technology is the mechanical and physical properties of the parts, which is expected to be similar or even higher compared to those created using conventional methods.

Maraging steels are attractive alloys for engineers and scientists due to their superior mechanical properties such as high strength as well as excellent toughness compared to other high strength steels (Rajkumar, et al., 2007), (Joshi, et al., 2016). Many industries including defense, nuclear, and the aviation sector have been utilizing maraging steels as strategic parts such as landing gears, rocket motor casings, and submarine hulls (Niu, et al., 2019), (Rajkumar, et al., 2014), and (Chakravarthi, et al., 2018).

Recently, maraging steels have become the materials of interest in the field of additive manufacturing due to low carbon content and their low susceptibility to solidification

cracking (Kürnsteiner, et al., 2017), (Lang, et al., 1971). Also, the martensite transformation is fully satisfied due to the high cooling rate inherent in additive manufacturing. In this regard, process parameters significantly affect the final characteristics of additively manufactured maraging steels. Most of the recent studies were dedicated to processing parameters such as laser power, scanning speed, spot diameter and scanning space in order to reach the lowest porosity levels for maraging steels (Bai, et al., 2017), (Mutua, et al., 2018), (Kempen, et al., 2011), (Casalino, et al., 2015), (Tapia, et al., 2016), and (Tang, et al., 2017). For example, it was shown that changing the laser power and scanning speed to a specific range can increase the relative density of 18Ni-300 maraging steel (Bai, et al., 2017), and (Mutua, et al., 2018). A comparison between the microstructure of conventional and LPBF fabricated maraging steels showed a higher fraction of the austenite phase in the AM part (Jägle, et al., 2016). Similar mechanical properties to conventional parts can be achieved by modifying process parameters and implementing appropriate heat-treatments (Mutua, et al., 2018), (Tan, et al., 2017), and (Suryawanshi, et al., 2017).

Kempen et al. (Kempen, et al., 2011) investigated the effect of layer thickness on the density of LPBF-maraging steels and found out higher density can be achieved at lower layer thicknesses. However, the use of lower layer thickness results in a longer time and higher production cost. It was also proven that the layer thickness is by far more influential on manufacturing time than other process parameters such as laser power, where the increase of layer thickness by 66% resulted in the reduction of manufacturing time by 40% (de Souza, et al., 2019). In this regard, layer thickness plays a significant role in the efficiency of the LPBF process. The effect of the powder layer thickness on the

microstructural characteristics of additively manufactured maraging steels has been overlooked in the literature. As a result, this study aims to thoroughly investigate the role of layer thickness on the microstructure, grain morphology, and texture, as well as the mechanical response of LPBF-maraging steel. Furthermore, this study sheds some light on the possibility of using higher powder layer thicknesses, while keeping the microstructure and mechanical properties consistent, and consequently make the LPBF method more affordable.

2.2 Experimental procedures

2.2.1 Materials and LPBF process

Gas atomized maraging steel powder with the brand name MS1 and chemical composition shown in Table 2.1 was used as the feedstock material (Material data sheet, 2017). This powder was virgin (never used) and supplied by EOS GmbH (Material data sheet, 2017). An EOS M290 machine was used to additively manufacture all the LPBF-MS1 samples. This machine was equipped with a 400 W Yb-fiber laser with a spot size of 100 μm. Nitrogen gas was blown over the build plate during the LPBF process, where the bed was preheated to 40 °C. Table 2.2 shows the laser power p (W), laser scan speed v (mm/s), hatch spacing h (mm), and powder layer thickness t (mm) used to produce two sets of samples along with associated simplified volume energy densities E (J/mm^3) defined as follows:

$$E = \frac{p}{v.t.h} \tag{1}$$

Table 2.1 Chemical composition of maraging steel MS1 powder (Material data sheet, 2017)

Element	Ni	Co	Mo	Ti	Al	Cr	Cu	C	Mn	Si	P	S
Max %	19.00	9.50	5.20	0.80	0.15	0.50	0.50	0.03	0.10	0.10	0.01	0.01
Min %	17.00	8.50	4.50	0.60	0.05	-	-	-	-	-	-	-

The effect of laser spot size to calculate the energy density is not considered in this equation, where it was kept constant in this study. A set of solid cubes with 10 mm×10 mm×10 mm dimensions along with cylindrical bars with 120 mm height and 12 mm diameter were built with layer thicknesses of 40 and 50 µm. Stripe scanning strategy was employed using a 10 mm length of stripes and 67° layer rotation to manufacture the samples. All the cylindrical bars were printed in the horizontal direction, as their longitudinal axes were perpindicular to the building direction. From now on, all the cubes and bars build with 40µm powder layer thickness are referred to as LPBF-MS1-40 and the ones produced using 50µm powder layer thickness as LPBF-MS1-50.

Table 2.2 LPBF process parameters applied in this research

p (W)	v (mm/s)	t (µm)	h (µm)	E (j/mm^3)
285	960	40	110	67.47
305	1010	50	110	54.90

2.2.2 Characterization

The morphology and size distribution of the MS1 powder were studied using microscopy and image processing procedures. Mapping techniques (Saha, et al., 2011) were used to measure the particle size distribution through the ImageJ software (Schneider, et al., 2012), where a mean value of over 200 particles was measured as a representative of the size distribution. MS1 powder particles were then mounted, polished, and etched to study the microstructure of the powder. The MS1 Powder particles were cold mounted first and then polished by a Nano 1000T Grinder-Polisher using SiC sand papers starting from FEPA grade 300 to 4000. The surface finishing was implemented via polish cloths along

with 6μm, 3μm, and 1μm diamond suspension. To elucidate the microstructural features for scanning electron microscope (SEM) observations, the samples were etched in Nital 3% ($3\ cm^3 HNO_3 + 97\ cm^3 Ethyl\ alcohol$) for 120 seconds (Murty, et al., 2016), (Small, et al., 2008), and (Sakai, et al., 2015). A Jeol 6400 SEM was used to study the powder characteristics, the LPBF-MS1 microstructure, and the fracture surfaces of the tensile samples. The SEM was also equipped with a Genesis Energy Dispersive X-Ray Spectrometer (EDS) to perform a quantitative compositional analysis of the LPBF-MS1 samples. The LPBF-MS1 samples were cut using an electrical discharge machining (EDM) equipment and polished for microscopic investigations. The LPBF-MS1 samples were hot mounted and the image processing was also conducted using a Zeta-20 optical microscope (OM) to measure the porosity fraction. For this purpose, the collected images were analyzed using a mapping technique, *i.e.* the porosities were detected based on the difference in the contrast, where the average value of the porosity fraction of 50 images was reported (Asgari, et al., 2017). In order to perform the SEM and EBSD studies of LPBF-MS1 samples, the last step of polishing using the 0.05μm OPS suspension was also added to the procedure previously explained. The Microstructure of LPBF-MS1 samples was further analyzed using a Hikari electron backscatter diffraction (EBSD) detector mounted on a field emission gun scanning electron microscope (FEG-SEM) FEI Nova NanoSEM-650. The EBSD samples were analyzed with 20nm and 70nm step sizes at ×5000 and ×2000 magnifications, respectively.

X-ray Diffraction (XRD) technique was then carried out to identify the phases. The Rietveld analysis was employed to measure the weight percentage of body-, and face-centered cubic (BCC-FCC) phases representing the martensite-austenite fraction. Data was

then collected using a Brucker D8 instrument equipped with a Co-Kα radiation source over a 2θ range of 45-105°at 45mA and 35kV. The same XRD instrument equipped with a VANTEC 500 area detector was used to measure the texture in all bulk samples. The texture measurement with 5 mm oscillation along the building direction was implemented to conduct the experiments. Pole figures were then calculated and developed using MTex software. Transmission electron microscopy (TEM) analysis was performed using an FEI Tecnai Osiris TEM equipped with a 200keV X-FEG gun to further study the precipitates in LPBF-MS1 samples. A Super-EDS detector set on the TEM apparatus was capable of probing down to 1 nm elemental mapping by means of a sub-nanometer electron probe. An FEI Helios NanoLab 650 dual-beam instrument was used to prepare the TEM samples using lift-out techniques where the thickness of the TEM samples was 50 nm.

2.2.3 Mechanical properties

A CRM Clark Rockwell hardness machine equipped with a diamond indenter head and 150kg load were used for hardness measurements in the HRC scale. At least three data were recorded to meet the repeatability requirements, where the average value was calculated and reported. A surface grinder was used for removing 1mm layers off of the surface of the LPBF-MS1 cubes to reach a new layer for measuring hardness as well as the porosity explained in the previous section. The process was repeated for each sample layer by layer to record hardness values for each layer.

The LPBF cylindrical bars deposited with two different powder layer thicknesses (40μm and 50μm) were used for uniaxial tensile tests. The test bars were machined into uniaxial tensile test configurations according to ASTM standard E8/E8M round tensile test specimens with a gage length of 30mm (Standard, 2015). Uniaxial tensile tests were

performed using a universal hydraulic Instron 1332 machine with a 25mm extensometer at quasi-static strain rates of 9×10^{-3} s^{-1}. Three tensile tests were performed for each sample set and the mechanical properties were derived from the tensile test data, where a typical graph for each set of samples was presented. The fracture surface along with the deformation region was subjected to further deformation studies using SEM and XRD techniques.

Fig. 2-1 shows the schematic of the uniaxial tensile test samples as well as the cubic samples. The building direction was toward the z-axis, while the side surface of the cubic sample is shown as the x-z and y-z surfaces. The EBSD and TEM were performed on the x-y plane passing through the center of the tensile sample.

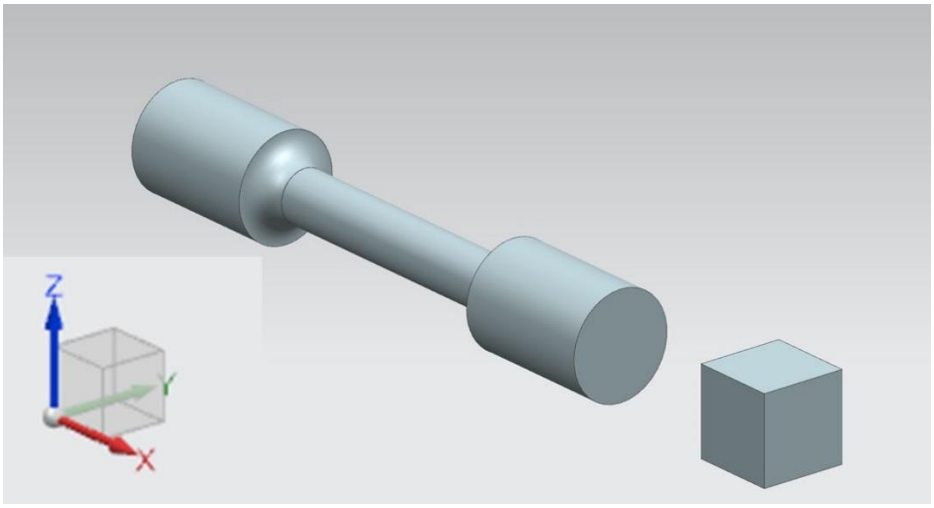

Fig. 2-1 Schematic of the uniaxial tensile test sample and the cubic samples.

2.3 Results

2.3.1 Powder characteristics

Fig. 2-2 shows the morphology and cross-section microstructure of the MS1 powder at high and low magnifications. Fig. 2-2 (a)-(b) presents the typical morphology and shape of the virgin powder used in this study. In Fig. 2-2 (a), a globular morphology consisting of spherical, oval, dumbell, and satellite-like powder particles can be observed. The spherical particles with smoother surfaces are dominant since the virgin powder was used, although the oval and dumbell-like particles were also found. It was stated that the best melting characteristics belong to small spherical particles with smooth surfaces due to a good combination of flowability and powder packing (Tan, et al., 2017), (Aboulkhair, et al., 2014), and (Asgari, et al., 2018). Besides, some ultrafine particles were also found in the powder, where the particle size is as small as 1μm (Fig. 2-2 (b)).

Fig. 2-2 (c)-(d) shows the cross-sectional microstructure of the virgin powder in two magnifications. The MS1 powder is featured with a dendritic structure where the dendrites are almost fully equiaxed, as seen in Fig. 2-2 (d). Such a fine cellular structure is related to the rapid cooling inherent to the gas atomization process (Chen, et al., 2018).

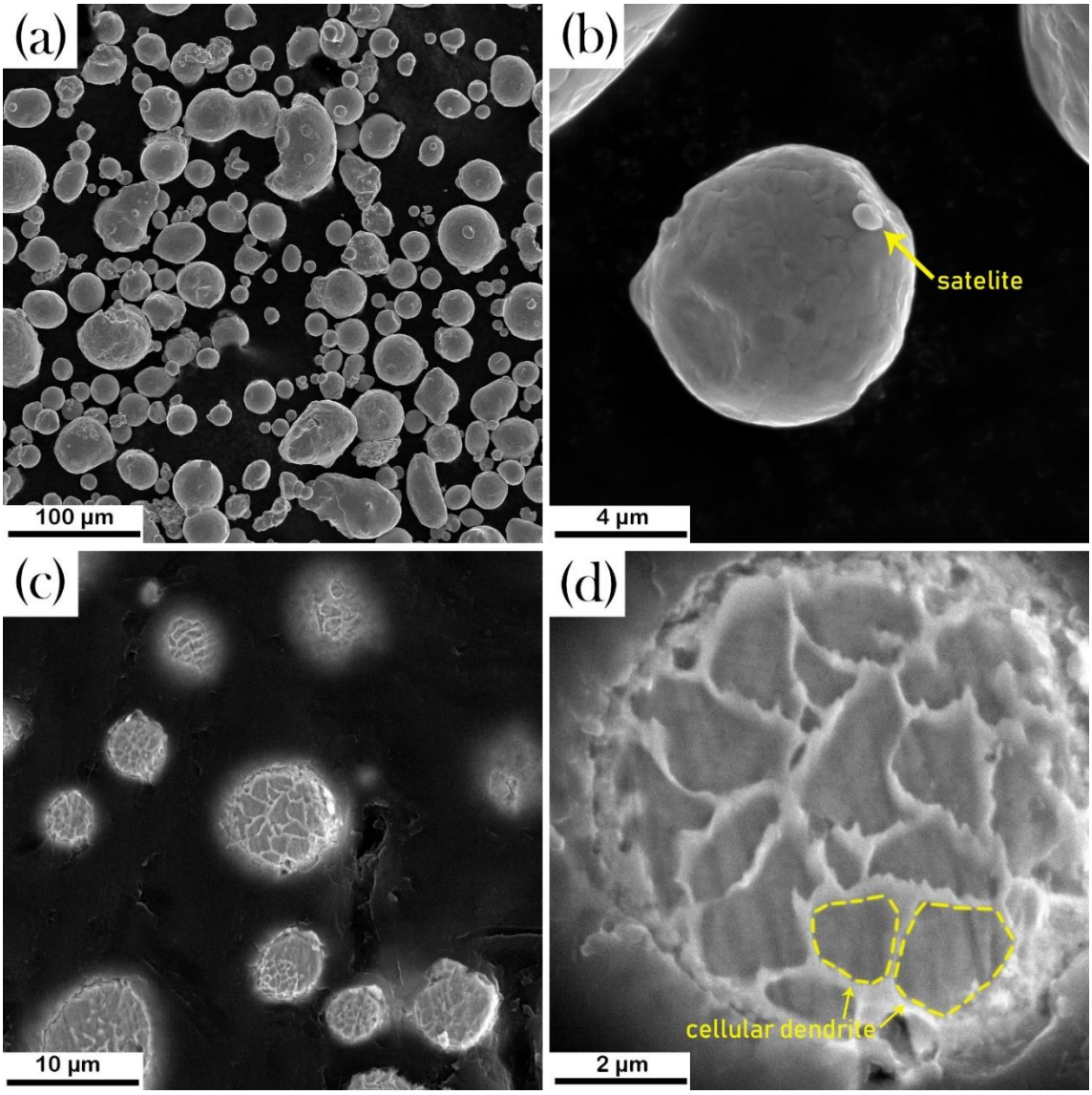

Fig. 2-2 SEM image for MS1 powder at two different magnifications for (a-b): morphology, and (c-d): microstructure.

A study on the MS1 particle size distribution is shown in Fig. 2-3. The average particle size of the virgin powder was less than 20µm, which was in agreement with the literature (Mutua, et al., 2018). In another detailed study, gas atomized 18Ni-300 maraging steel powder with an average particle size of 41.62µm and spherical morphology was used to build test samples (Tan, et al., 2017). Recent studies showed a similar cellular structure and particle size distribution for LPBF-maraging steels (Shakerin, et al., 2019), (Kučerová,

et al., 2019). As a comparison, the average particle size along with the cumulative distribution percentage for d_{10}, d_{50}, and d_{90} of the powder is presented in Table 2.3. The particle size average is measured to be 17.40μm with 8.46μm standard deviation shown in Table 2.3. Gas atomized powder particles of 18Ni-300 maraging steel with an average size of 35μm with a d_{90} equal to 54μm was reported in the literature as well (Casati, et al., 2016) and (Bhardwaj, et al., 2018), while similar powder with 15-45μm particle size distribution was used in another work (Bai, et al., 2017).

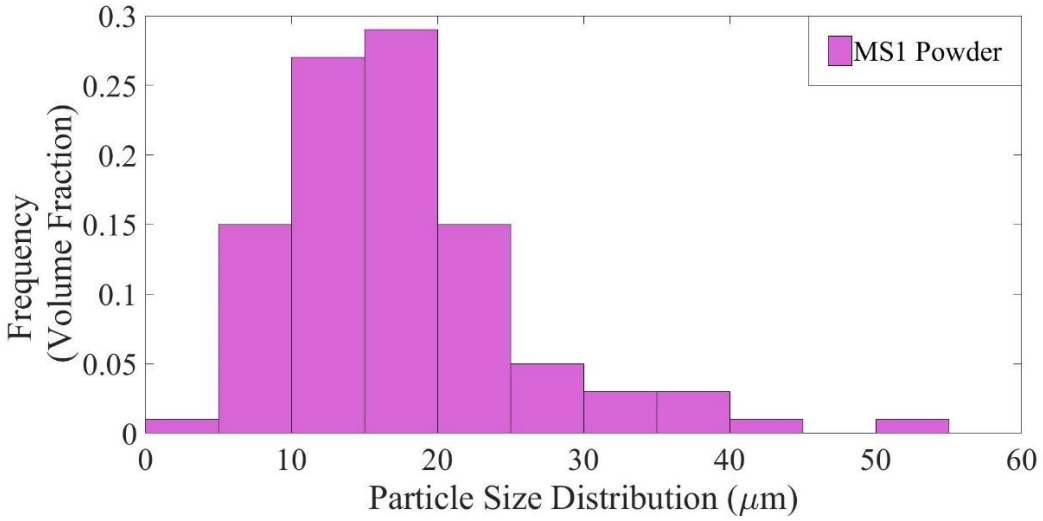

Fig. 2-3 The particle size distribution of the MS1 powder.

Table 2.3 Particle size average and cumulative distribution percentage (while μ is the average particle size and σ represents the standard deviation). All data are in μm.

Powder	μ ± σ	d_{10} (10%)	d_{50} (50%)	d_{90} (90%)
Gas atomized	17.40 ± 8.46	8.22	15.62	26.30

2.3.2 LPBF-MS1 solidification

Fig. 2-4 illustrates the variations of the porosity level through the depth of the cube samples. At the surface, the porosity level of 0.45% and 0.34% were calculated for the LPBF-MS1-40 and LPBF-MS1-50 cubic samples, respectively. By moving towards the depth, this value decreases more rapidly for the LPBF-MS1-40 cube than the LPBF-MS1-50 sample. Finally, both samples leveled off around 0.1% porosity value at the depth of 2.5mm. The measurements were conducted for over 3.5mm inside the core considering the symmetry and similar properties for the side faces. Contour process parameters used on the sides of the cubes for better surface finish are the main reasons for such variation of porosity (Mohammadi, et al., 2018). The rapid drop of porosity for the LPBF-MS1-40 cube can be due to heat dissipation at the edge of the sample in addition to the numerous heating and cooling cycles applied to the melt pools. On the side of the samples the heat dissipates through the powder bed from one side and to the solid block on the other side during the production. These factors affect the homogeneity of the material prompting changes in porosity for the first few millimeters. The powder layer thickness shows no effect on the heating dissipation at the core of the material (See Fig. 2-4). This can be simply due to the overlap of layers during the deposition process forming the melt pools. In other words, each time the laser is applied, a certain depth of material remelts (which is more than the height of the powder layer thickness) and is a function of the applied energy (Gong, et al., 2014).

Porosity as a function of scan speed has been studied previously for 18Ni-300 maraging steel. The macro-hardness and relative density (as a measure of porosity) were reported to be interconnected (Kempen, et al., 2011), while the relationship between the microhardness

and porosity was not depicted in the same research. Relative density was measured in the literature for various energy densities showing that the highest relative density of 99.9% can be achieved at a certain energy density (Casalino, et al., 2015). A more detailed study on the parameters affecting the relative density showed the conjoint effect of laser power, scan speed, and scanning space on the relative density (Bai, et al., 2017). In another study, the image analysis method (IAM) showed a higher porosity compared to the Archimedes method for the same material (Suryawanshi, et al., 2017). In the current literature, the variation of porosity throughout the bulk material has been overlooked. In the current study, the process parameters have been set in order to reach the highest relative density based on the recommendation of the manufacturer as well as the literature and then the porosity has been measured through the depth of the material as far as the change was observed.

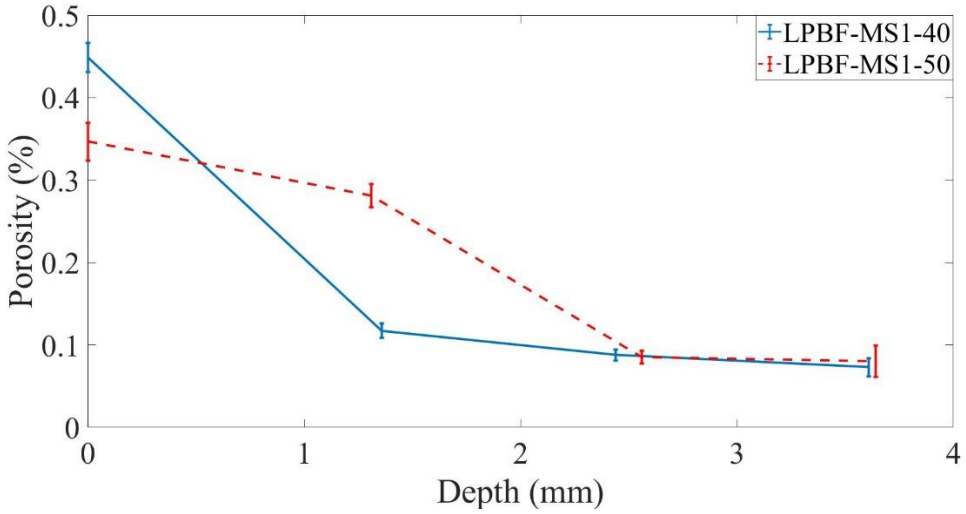

Fig. 2-4 Variation of the porosity through the depth of LPBF-MS1-40 and LPBF-MS1-50 cubes.

Phase studies on metal powders in AM were done on AlSi10Mg (Asgari, et al., 2017) and stainless steel CX (Asgari, et al., 2018) previously, as well as 18Ni-300 maraging steel (Mutua, et al., 2018). X-ray diffraction patterns of the MS1 powder and the LPBF-MS1-

40 and LPBF-MS1-50 cubes are shown in Fig. 2-5, where austenite (γ) and a combination of ferrite (α) and martensite (α′) volume fractions are also presented. The virgin powder contains a 7.37% austenite phase, while this amount decreases to 2.33% and 2.27% after printing the LPBF-MS1-40 and LPBF-MS1-50 cubes, respectively. Numerous heating/cooling cycles during the sintering process resulted in the final reduction of the austenite fraction in these samples. The laser processing of the gas atomized maraging steel powder affects the microstructure of LPBF-MS1. The high solidification rate during the printing process seems to prevent the formation of the austenite. Moreover, increasing the powder layer thickness has no effect on the final phases. Changing other process parameters resulted in austenite volume fraction ranging from 4 to 10% in previous studies (Bhardwaj, et al., 2018). In a recent study on the wire arc additive manufacturing (WAAM) of maraging steel, 8.3% austenite fraction was reported (Xu, et al., 2018). The 2.33% and 2.27% austenite reported in the current study is the lowest achieved compared to the literature. The difference between the austenite volume fraction in WAAM and LPBF processed maraging steels is due to the different solidification rates inherent in these two methods (Dharmendra, et al., 2019).

Similar to any other high nickel steel alloy, transformation in maraging steels from austenite to martensite occurs in a shear-type diffusionless mechanism, and martensite is reported to be the only product of austenite transformation (Hall, et al., 1968). The crystal structure of iron-nickel martensite is the same as ferrite (BCC), where their differences are related to the higher dislocation density of martensite (Hall, et al., 1968).

The martensite phase grew initially inside the prior-austenite grains (PAG) during the solidification forming packets of martensite. The reverted austenite layers then started to

form along the PAG and martensite packet boundaries. They were reported to grow longitudinally keeping the lateral dimension less than 200nm (Qian, et al., 2016) and (Galindo-Nava, et al., 2016)).

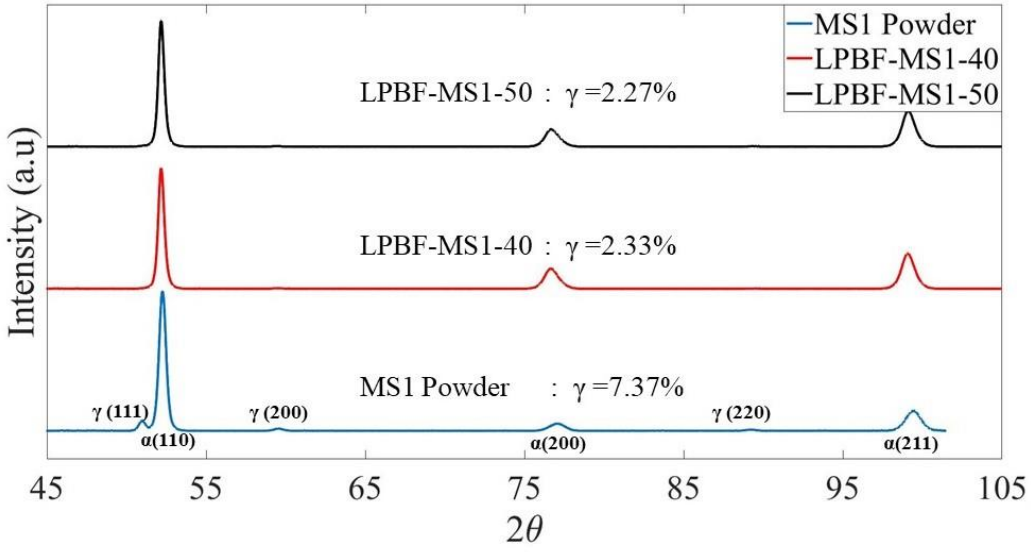

Fig. 2-5 XRD analysis of the MS1 powder, LPBF-MS1-40, and LPBF-MS1-50 cubes.

Fig. 2-6 (a)-(f) compares the SEM microstructures of the LPBF-MS1-40 and LPBF-MS1-50 samples at different magnifications. For both samples, well-ordered melt pools can be found in Fig. 2-6 (a) and (d), where fish scale marks were highlighted showing consistent melting patterns in almost all deposition layers. The melt pools are almost identical in size and shape resulting in a more homogeneous microstructure. The parabolic melt pool boundary was related to the solidification and re-solidification of the under layers (Casalino, et al., 2015). As can be seen, the solidification structure of both samples consists of overlapped melt pools in semi-elliptical shape. At higher magnification shown, the solidification structure consists of very fine columnar and equiaxed cells for both LPBF-MS1-40 and LPBF-MS1-50 samples. Indeed, the dendritic solidification structure of the manufactured cubes is similar to the feedstock powder as shown in Fig. 2-2 and Fig. 2-6.

The evolution of such a fine solidification morphology is due to the high cooling rate of the LPBF process (Bodziak, et al., 2019). The dendritic columnar cells grew perpendicular to the melt pool boundaries due to the heat flux direction, although the crystal structure seemed to force its preference to incline the dendritic direction from the perpendicular line (Wang, et al., 2016). This cellular-dendritic morphology is typical of additively manufactured maraging steels and attributed to the elemental microsegregation at the cell boundaries (Kučerová, et al., 2019), (Shakerin, et al., 2019). Above all, the solidification morphology of the LPBF-MS1-40 and LPBF-MS1-50 samples are almost identical, and layer thickness seems not to affect the solidification behavior of the LPBF-MS1.

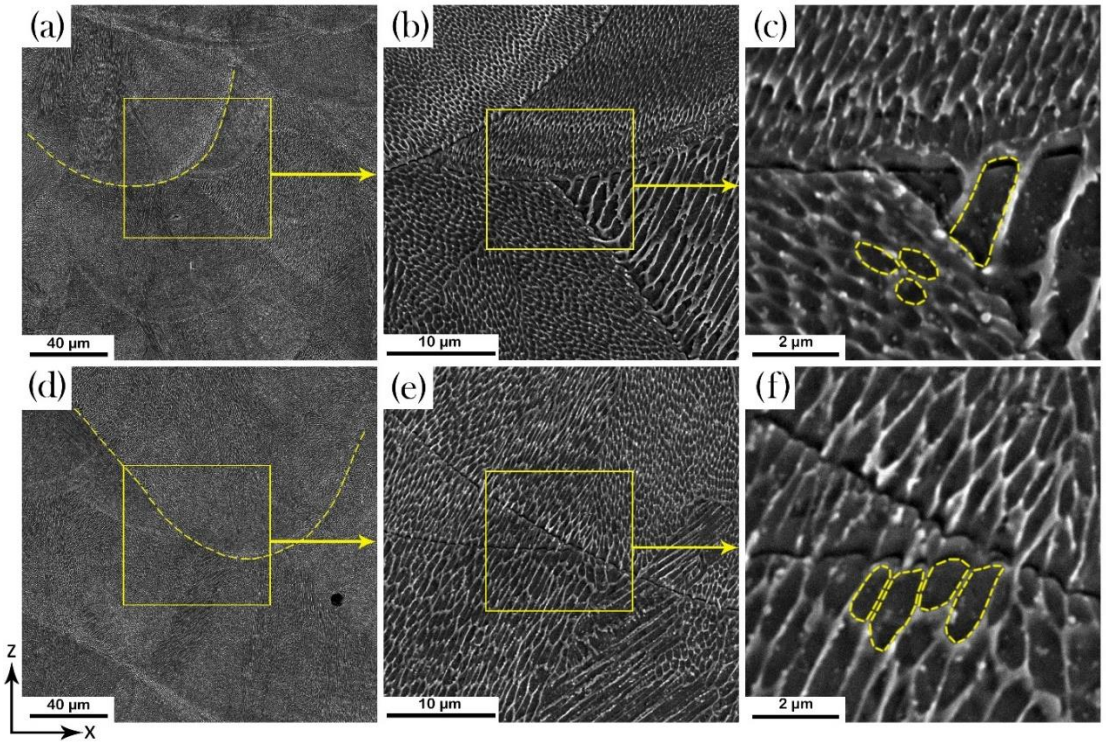

Fig. 2-6 SEM image at three different magnifications of (a-c): LPBF-MS1-40 cube, and (d-f): LPBF-MS1-50 cube.

2.3.3 Characterization and grain structure

Fig. 2-7 shows the EBSD-inverse pole figure (IPF) and the EBSD-phase maps for both LPBF-MS1-40 and LPBF-MS1-50 samples. The crystallographic planes oriented in the same direction are presented in the IPF maps with the building direction along the z-axis. As shown in Fig. 2-7 (a)-(b), the LPBF-MS1 is consisted of mostly columnar grains evolved epitaxially along a preferred orientation in both LPBF-MS1-40 and LPBF-MS1-50 samples. The grains in bundles of solidified cells oriented in the same crystallographic direction. The bundle structure was also reported for the laser metal deposited maraging steels (Kürnsteiner, et al., 2017). The phase maps show a very low amount of austenite for the LPBF-MS1-40 and LPBF-MS1-50 samples. However, the latter has slightly higher. The presence of austenite at the grain boundaries was also reported in the literature (Kučerová, et al., 2019) and (Kürnsteiner, et al., 2017). Martensite and ferrite are the main phases observed on EBSD maps. Although the scanning strategy can affect the crystal growth direction, it is shown previously that the grain growth is perpendicular to the scanning plane (Bhardwaj, et al., 2018). Moreover, the epitaxial grain growth along the building direction is depicted in the EBSD maps as well, which is in the direction of the heat flux.

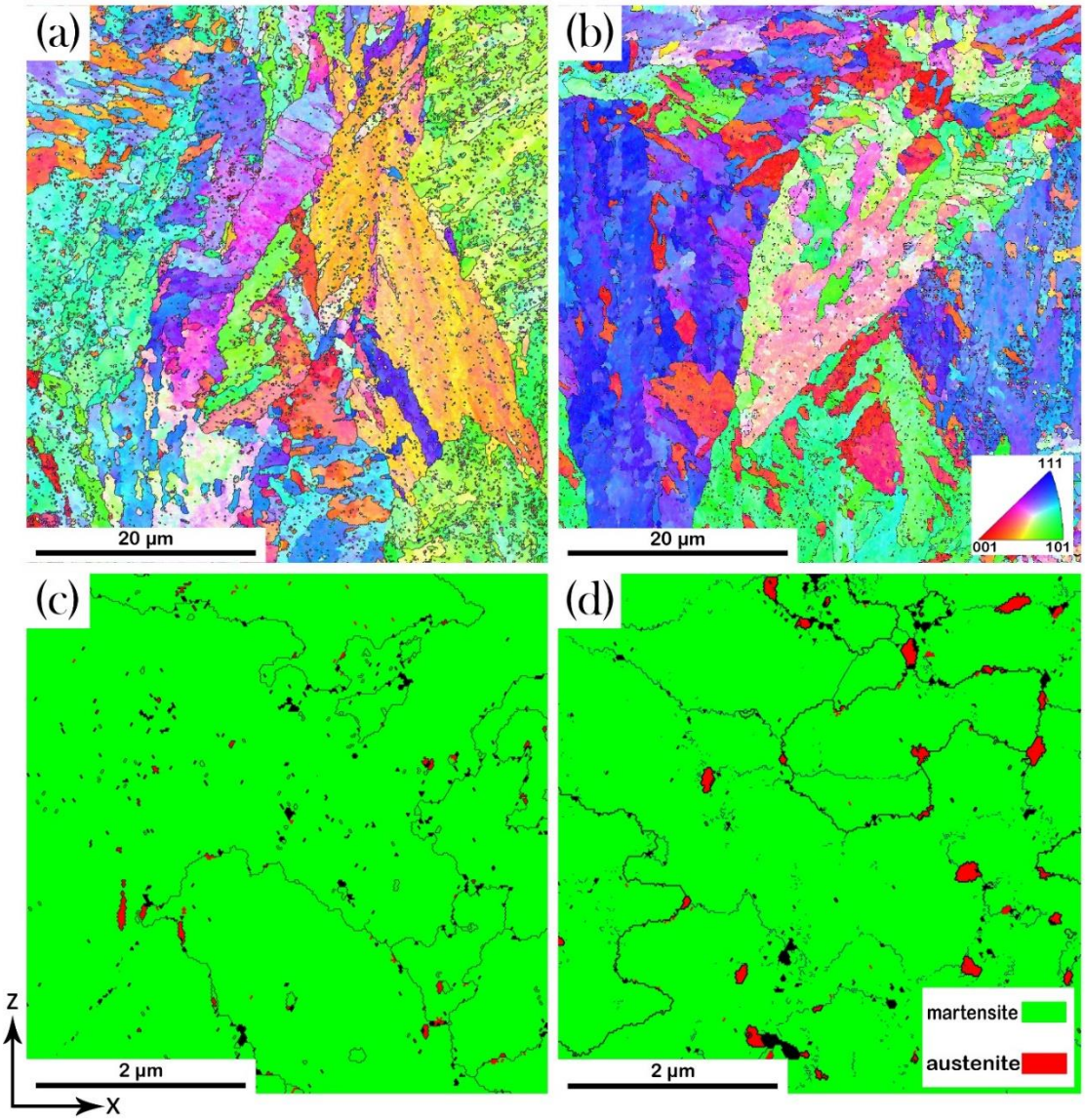

Fig. 2-7 EBSD mappings showing (a): IPF orientation map of LPBF-MS1-40, (b): IPF orientation map of LPBF-MS1-50, (c): phase map of LPBF-MS1-40, (d): phase map of LPBF-MS1-50.

Fig. 2-8 (a), (b) shows the XRD texture analysis for the as-built samples with the building direction along the z-axis. The pole figures depicted through XRD show a very weak fiber texture in both cases. Moreover, the epitaxial growth of the crystal structure during the manufacturing process in the building direction is in accordance with the literature (Suryawanshi, et al., 2017) and (Bhardwaj, et al., 2018). In Fig. 2-8 (c), (d), the

orientation distribution function (ODF) graphs are illustrated at different layer thicknesses, indicating the typical γ fiber texture with very low intensity at φ_2=45° section. Thus, the as-built LPBF-MS1 texture is almost random either for LPBF-MS1-40 or LPBF-MS1-50. Bhardwaj et al. (Bhardwaj, et al., 2018) also reported the absence of a strong texture in LPBF-maraging steels.

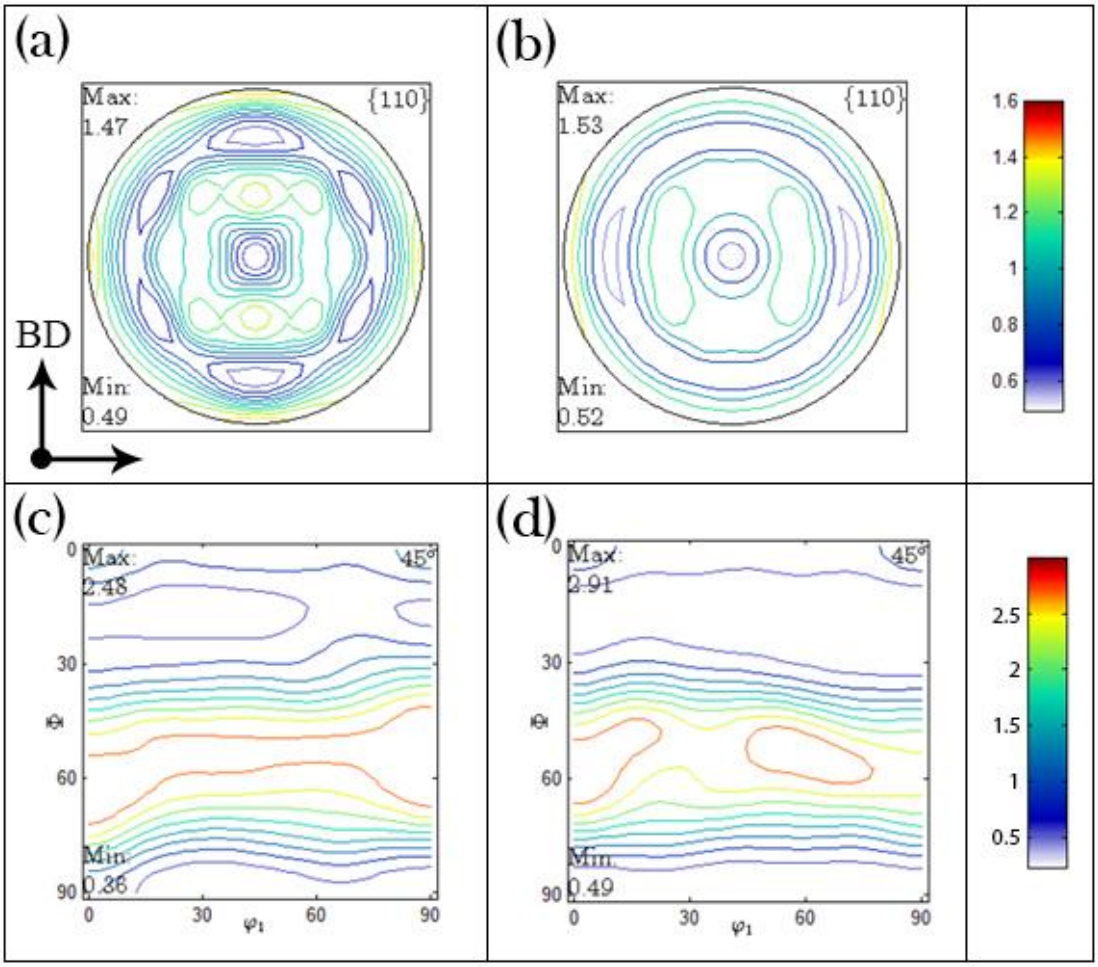

Fig. 2-8 XRD Pole Figures showing Phase maps at (a): LPBF-MS1-40, and (b): LPBF-MS1-50, ODF sections at φ_2=45° shown at (c): LPBF-MS1-40, and (d): LPBF-MS1-50.

In order to characterize the fine precipitates and secondary phases in LPBF-MS1 samples, TEM analysis was conducted to study the distribution of alloying elements. The STEM high angle annular dark -field (HAADF) image along with the EDS elemental maps

are shown in Fig. 2-9 and Fig. 2-10 for the LPBF-MS1-40 and LPBF-MS1-50 samples, respectively. As can be seen, both samples contain globular particles within the matrix, which are rich in Ti, Al, N, and O. These particles are core-shell structures with aluminum oxide in the core and titanium nitride (TiN) in the shell. Ti/Al-rich nanoparticles were previously observed in LPBF- maraging steel grade 300 (Tan, et al., 2017). Due to the manufacturing process, the entrapped nitrogen forms the TiN in spherical shape surrounded by Al_2O_3 shell through the Marangoni effect, which is in accordance with the literature as well (Kempen, et al., 2011). The LPBF-MS1-50 sample contains more of these core-shell particles than the LPBF-MS1-40 sample. This means that the layer thickness can affect the microstructure in terms of the density of nanoparticles. This is expected since more powder is deposited in the LPBF-MS1-50 case compared to the LPBF-MS1-40 one resulting in a higher degree of entrapped gas along the powder bed, while the size of the nanoparticles is finer in the LPBF-MS1-50 samples.

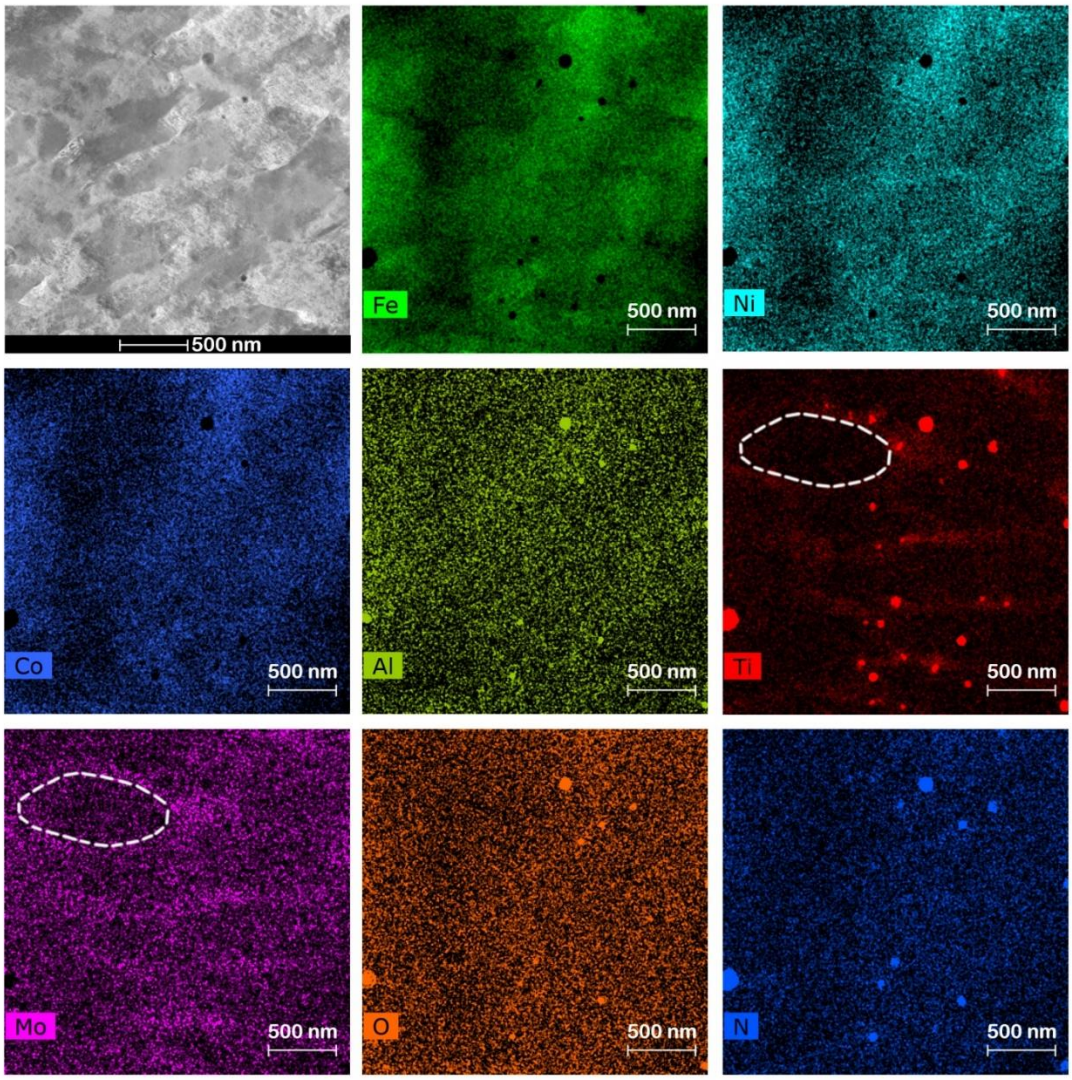

Fig. 2-9 STEM-HAADF image and the corresponding EDS elemental maps of LPBF-MS1-40.

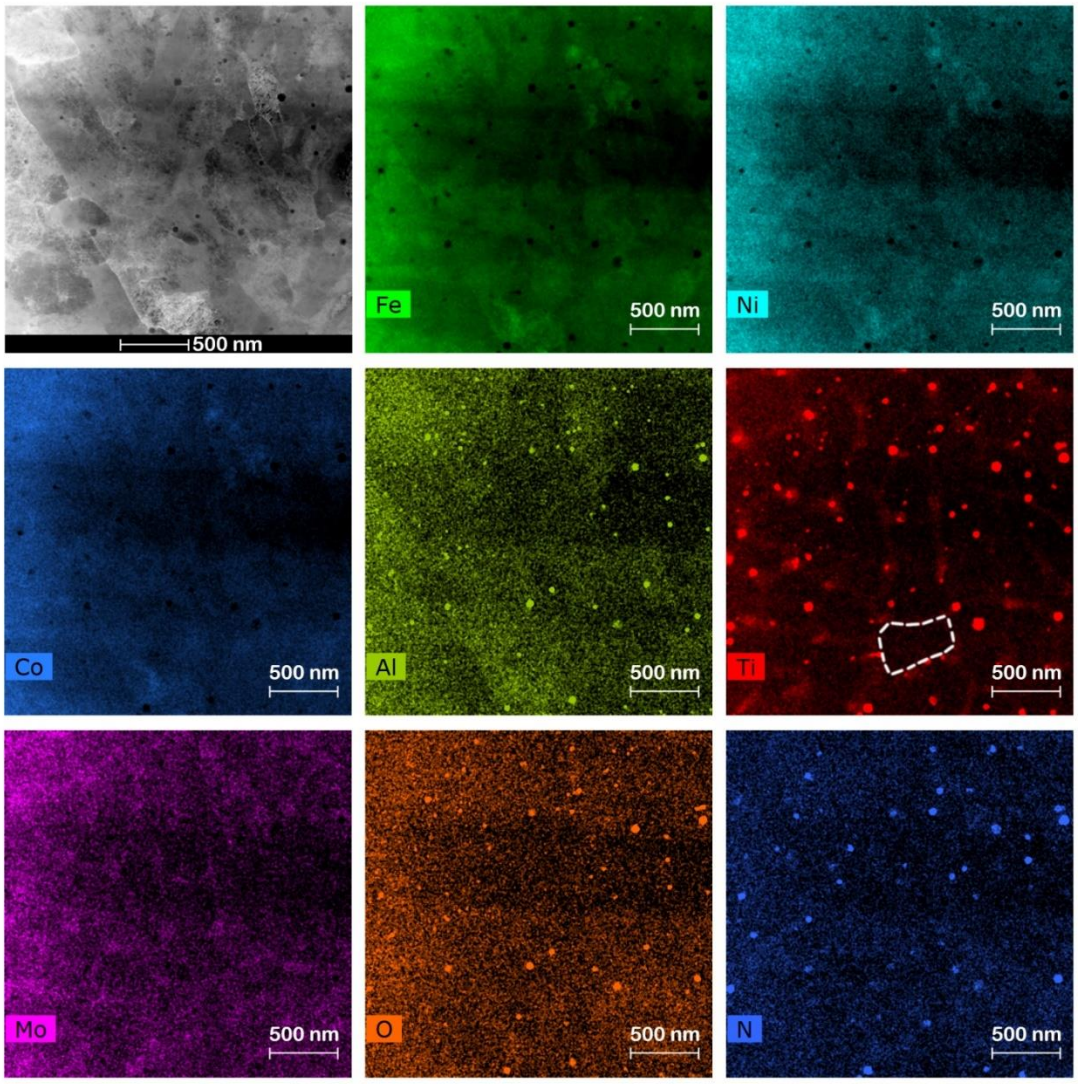

Fig. 2-10 STEM-HAADF image and the corresponding EDS elemental maps of LPBF-MS1-50.

2.3.4 Mechanical properties

Fig. 2-11 shows the hardness variations through the depth of the LPBF-MS1 cubes. The hardness values were measured in the HRC scale ranging from 37-39 and 38.5-40 for the LPBF-MS1-40 and LPBF-MS1-50 samples, respectively. The hardness increases from the surface to the depth of 2.5mm for both the LPBF-MS1-40 and LPBF-MS1-50 samples. Furthermore, the hardness value levels off for the LPBF-MS1-50 case, while it slightly decreases for the LPBF-MS1-40 cube.

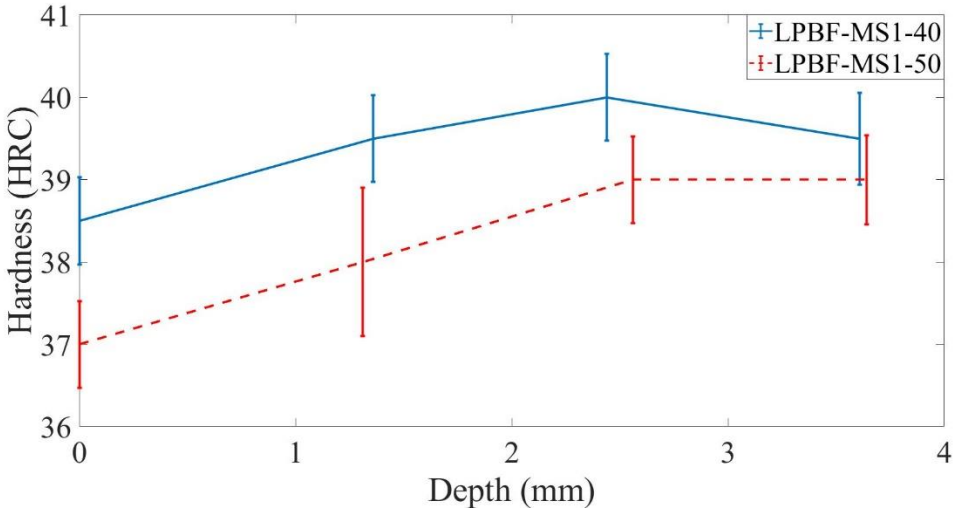

Fig. 2-11 Variation of hardness through the depth of LPBF-MS1-40 and LPBF-MS1-50 cubes.

Uniaxial tensile properties are shown in Fig. 2-12 to study the effect of the powder layer thickness on the mechanical properties. Both sets of samples behaved similarly under uniaxial tensile loading involving almost the same stress-strain curves. Yield strength of 1084 ± 10 and 1126 ± 31 MPa and ultimate tensile strength of 1222 ± 4 and 1221 ± 2 MPa were measured for the LPBF-MS1-40 and LPBF-MS1-50 samples, respectively. In the necking zone, there was a divergence in the mechanical responses of the two sets of samples as they fractured at different elongations. The LPBF-MS1-40 sample elongated at 14.6%, while the elongation of the LPBF-MS1-50 sample was measured to be 12.9%. The

higher ductility of the LPBF-MS1-40 samples can be attributed to the lower nanoparticle content (see Fig. 2-9 and Fig. 2-10). Fig. 2-13 represents a summary of the fracture strain and yield and ultimate strength of the as-built additive manufactured maraging steels in the literature as well as in this research. The highest strength was acquired by the result of the current research compared to the literature. The elongation is also high compared to most cases in previous studies, (Bai, et al., 2017), (Casalino, et al., 2015), (Tan, et al., 2017), (Kučerová, et al., 2019), (Casati, et al., 2016) and (Bhardwaj, et al., 2018).

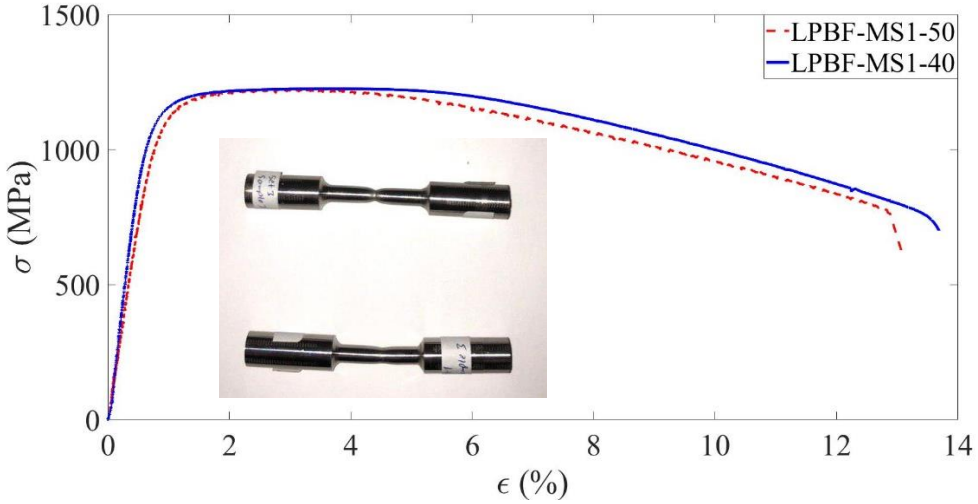

Fig. 2-12 Typical uniaxial tensile stress-strain curves of LPBF-MS1-40 and LPBF-MS1-50.

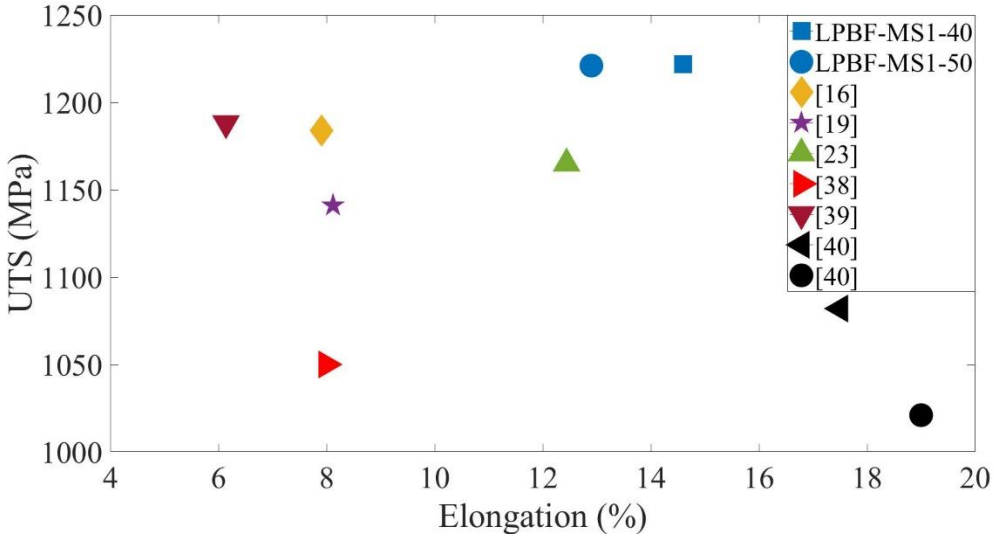

Fig. 2-13 Ultimate strength versus elongation in various studies for the as-built additively manufactured 18Ni-300 maraging steel including this study.

Fig. 2-14 shows the SEM fracture surface of the uniaxial tensile samples at high and low magnifications. At the macroscopic scale, the fracture surfaces of both samples seem to be identical containing a peripheral shear zone along with a central fibrous zone. This is the classic cup and cone fracture type, where voids nucleate and grow at the center and finally coalesce leading to the separation of the central region. Thereafter, shear-mode fracture occurs on the periphery of the sample at approximately 45° to the loading axis (Meyers, et al., 2008). The number of voids at the central zone is considerably higher for the LPBF-MS1-50 samples rather than the LPBF-MS1-40 ones (see Fig. 2-14 (a)-(b)). Particularly, large voids are more concentrated in the LPBF-MS1-50 sample. This could be related to the higher concentration of TiO_2 inclusion in the microstructure of the LPBF-MS1-50 samples. Incomplete melting sites and unmelted powders were also reported to act as the origin of large voids (Casati, et al., 2016). The high magnification features of fracture surfaces at the central zone are presented in Fig. 2-14 (c) and (d). Scan tracks pulled out of the surface are marked in Fig. 2-14 (c) and (d) as well (Asgari, et al., 2017). The typical

dimple rupture with relatively similar size and shape can be observed for both samples indicating an identical ductile fracture of both samples at the micro-scale. The equiaxed and C-shaped dimples were also observed for 18Ni-300 maraging steels (Dos Reis, et al., 2015). Another potential for initiating fracture is the PAG boundaries as a softer part of the matrix (Viswanathan, et al., 2005). Three weak points starting the fracture were to be the melt pool boundaries, grain boundaries, and intragranular boundaries (Zhong, et al., 2016) (Guan, et al., 2013) (Mills, et al., 1987).

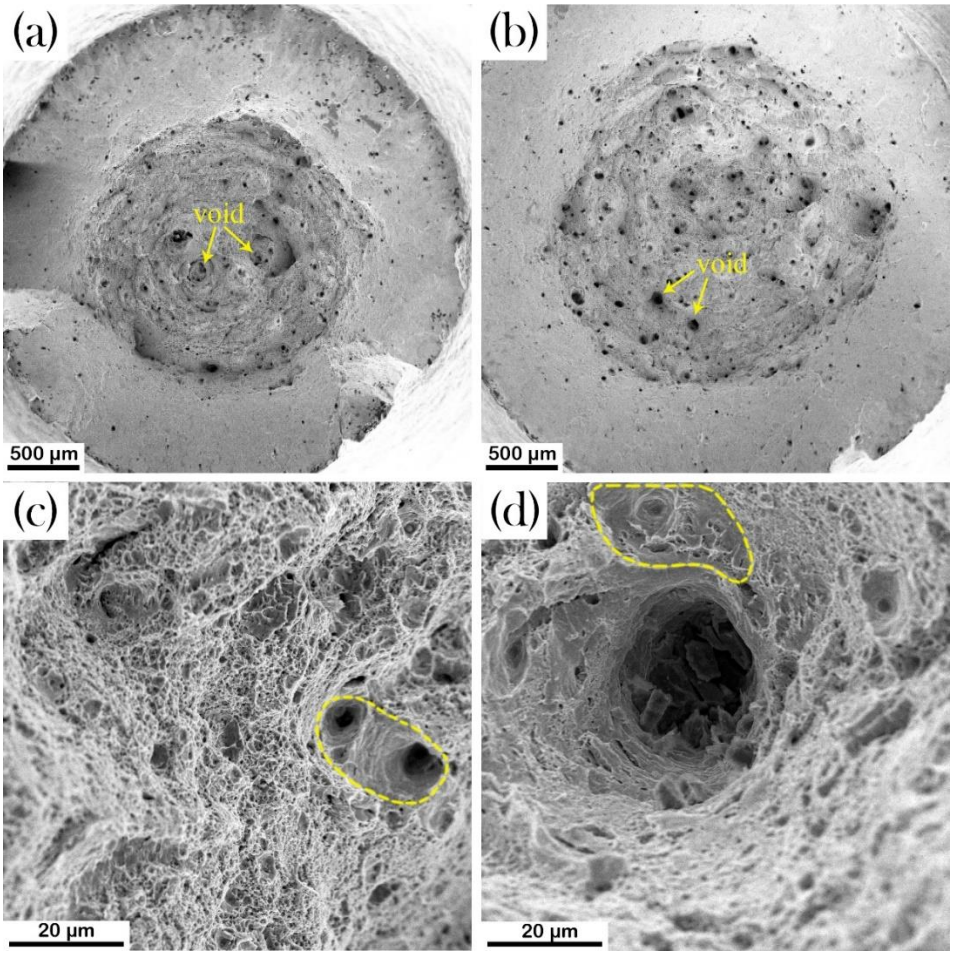

Fig. 2-14 SEM images of fracture surface at two different magnification for (a, c): LPBF-MS1-40, (b, d): LPBF-MS1-50.

The deformed samples were cut along the loading direction to perform a deformation analysis. Fig. 2-15 depicts the unique color grain maps for both deformed samples with the building and loading directions along the z and x axes, respectively. Compared to the as-built condition (Fig. 2-7 (a)-(b)), the grains were elongated along the loading direction regardless of the AM building direction, see Fig. 2-15 (a)-(b). It is noted that, despite the presence of some zero solutions in the LPBF-MS1-40 sample, still elongated grains are obvious in Fig. 2-15 (a). The 40 × 40 μm scan area showed a similar grain width for both LPBF-MS1-40 and LPBF-MS1-50 cases with more elongated grains in the latter along the loading direction. Mutua et al. (Mutua, et al., 2018) reported an average grain size of less than 1μm for the as-built condition, which is obviously finer than the deformed samples in the current study.

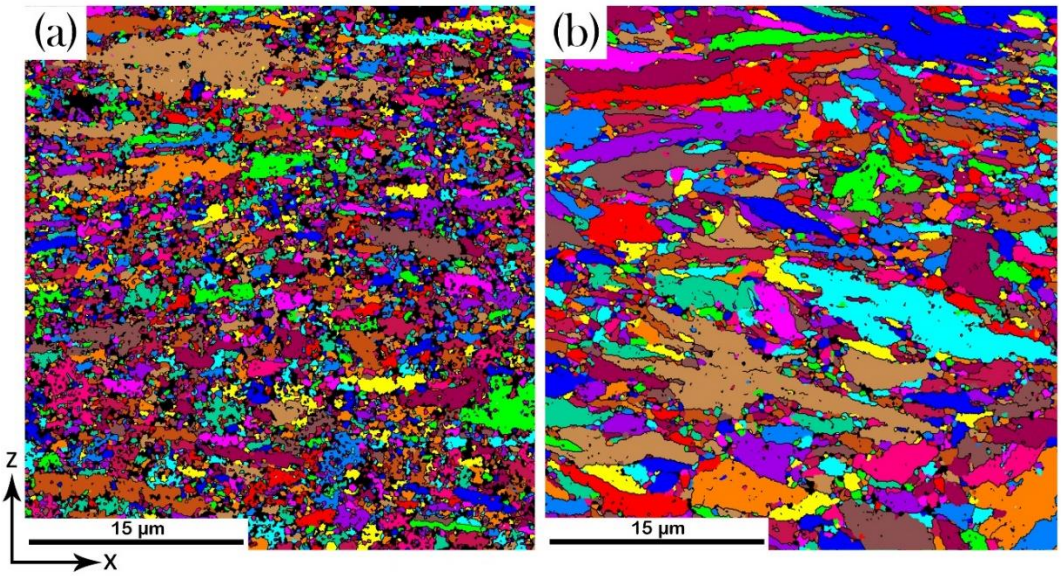

Fig. 2-15 Grain color map of deformed samples for (a): LPBF-MS1-40, and (b): LPBF-MS1-50.

Texture analysis of the deformed samples carried out using XRD texture analysis and it is shown in Fig. 2-16 (a)-(b). Similar pole figure patterns can be observed for both samples

with higher intensity for the LPBF-MS1-40 case, see Fig. 2-16 (a)-(b). It is obvious from the {110} pole figure that, the high-intensity points are located at the north and south poles, implying a preferred texture along the <110> direction. Although the intensities were close for the LPBF-MS1-40 and LPBF-MS1-50 in the as-built samples (1.47 and 1.53), the increase was more significant for the former compared to the latter case (3.2 and 2.6) after the deformation (See Fig. 2-8 and Fig. 2-16). In other words, the deformed LPBF-MS1-40 samples showed a stronger texture compared to other cases. The ODF results are shown in Fig. 2-16 (c)-(d) and reveals a weakened γ fiber texture, while a rotated cube appeared for both samples. The Crystalographic texture of (001)[$1\bar{1}0$] and (001)[$\overline{1}\overline{1}0$] with a maximum intensity of 5.34 for LPBF-MS1-40 and 4.95 for LPBF-MS1-50 was observed in addition to the weak γ fibers observed in Fig. 2-8.

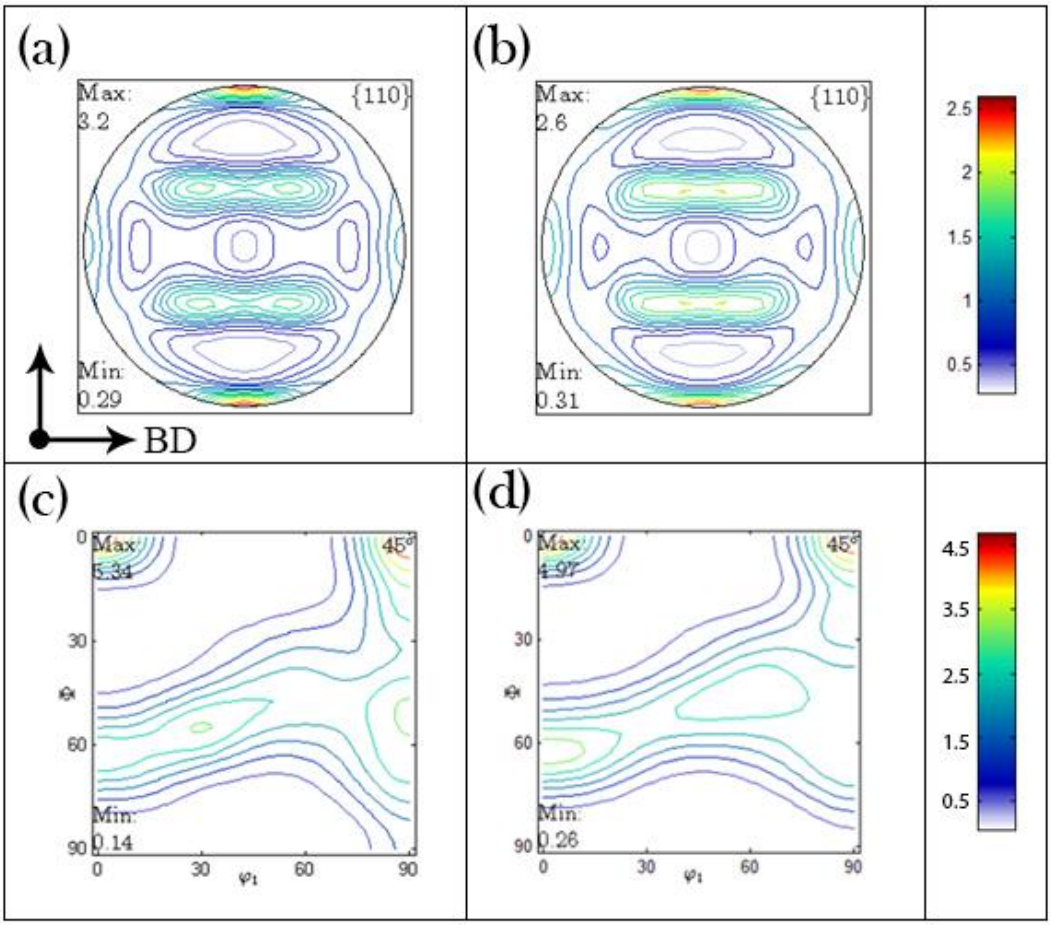

Fig. 2-16 XRD Pole Figures of deformed samples showing grain orientation (a): LPBF-MS1-40, (b): LPBF-MS1-50, ODF sections at φ_2=45° of deformed samples (c): LPBF-MS1-40, and (d): LPBF-MS1-50.

2.4 Discussion

Using fine MS1 powder with an average particle size below 20μm in addition to proper process parameters resulted in higher mechanical properties compared to previous studies (see Fig. 2-3 and Fig. 2-13) (Tan, et al., 2017). This is due to having lower porosity (Fig. 2-4) as well as lower austenite fraction (Fig. 2-5). The powder layer thickness seems to have less influence on the mechanical properties if the process parameters are selected cautiously. As shown in Equation 1, the energy density applied through the additive manufacturing process is affected by the powder layer thickness, hatch distance, scanning speed and laser power. The energy density applied was 67.47 J/mm^3 for the LPBF-MS1-40 and 54.90 J/mm^3 for the LPBF-MS1-50. Although the energy densities reported in previous studies were much higher (95 J/mm^3 (Suryawanshi, et al., 2017), 198 J/mm3 (Kempen, et al., 2011) and a range of 75-132 J/mm^3 (Casalino, et al., 2015)), better mechanical properties were not reported. The lower energy density results in cheaper products and the higher powder layer thickness results in faster prints. Changing the powder layer thickness from 30μm ((Casalino, et al., 2015), (Kempen, et al., 2011), and (Suryawanshi, et al., 2017)) to 40μm in the current study means 33% faster print while changing to 50μm is 66% quicker.

2.4.1 Properties through the depth

The primary investigation on the LPBF-MS1 showed that the core porosity level was almost the same for both LPBF-MS1-40 and LPBF-MS1-50 samples. This means that the porosity level can be kept the same by applying proper process parameters and increasing the powder layer thickness. However, the sub-surface porosity level was slightly higher for the LPBF-MS1-50 samples. The hardness variation was well consistent with the porosity

gradient through the depth, where the hardness values dropped with the increase of porosity (see Fig. 2-4 and Fig. 2-11). The same hardness-porosity correlation was previously observed in the 18Ni-300 maraging steel (de Souza, et al., 2019).

2.4.2 Phase change due to additive manufacturing process

Both samples contained almost the same amount of austenite in the martensitic matrix as well as solidification structure, identical grain morphology, and crystallographic texture (see Fig. 2-6, Fig. 2-7, and Fig. 2-8). The solidification structure of the powder looked similar to the as-built additively manufactured samples. However, the distinction between the two samples was detected via the STEM results in Fig. 2-9 and Fig. 2-10, where the LPBF-MS1-50 sample was more concentrated in Al/Ti-rich nanoparticles. The formation of these particles was reported to be a result of high precipitation kinetics (Bodziak, et al., 2019). The LPBF process is intrinsically fast in cooling, which can satisfy the fast formation kinetics of Al/Ti-rich nanoparticles. Due to the thinner layer thickness of LPBF-MS1-40, the sample was exposed to more heating/cooling cycles, and thus apparently a fraction of the nanoparticles dissociated and dissolved in the matrix. As a result, the layer thickness can affect the microstructure of LPBF-MS1 at the nanoscale.

The martensitic structure is the main reason for high strength and hardness for this material in the as-build condition due to its high dislocation density (Galindo-Nava, et al., 2016)) (Sha, et al., 2009). Lath martensite with submicron width was reported previously as the main phase to be observed in the TEM micrographs, while the austenite along with the precipitates was also tracked in the dark field graphs. The latter phases mainly formed and located inside the martensite laths. Globular and Widmanstatten austenite morphologies were both reported for additively manufactured maraging steels in the

literature (Viswanathan, et al., 2005). The grain size of the martensite packets is a function of martensite start (M_s) temperature, while the packets are grown inside the PAGs with high angle misorientations (Qian, et al., 2016). Therefore, the coarser martensitic microstructure was observed in the EBSD orientation maps, while the austenite was finer and located in the boundaries (Casati, et al., 2016). Besides, martensite laths can be observed across the coarse grains, which is typical in LPBF-maraging steel (Shakerin, et al., 2019).

The elastic-plastic behavior under uniaxial tensile loading was relatively analogous for both samples, which is consistent with the microstructural similarities mentioned earlier. More interestingly, the LPBF-MS1-50 samples reached an identical UTS value to that of the LPBF-MS1-40 ones. The independency of tensile strength with the variation of layer thickness was also reported for the LPBF 304 stainless steel (Guan, et al., 2013). The only noticeable difference appeared in the necking zone, where the LPBF-MS1-50 case failed at slightly lower elongation than the LPBF-MS1-40 one. According to the cup & cone fracture mechanism, the nanoparticles embedded in the matrix can act as the nucleation sites for void formation (Bertoli, et al., 2017) (Croccolo, et al., 2016) (Cyr, et al., 2018). Thus, the higher concentration of nanoparticles (see Fig. 2-10) can be responsible for the negligible lower ductility in the LPBF-MS1-50 samples. The sub-surface porosity can also assist rupture in the shear zone (see Fig. 2-4) (Dilip, et al., 2017) (Ebrahimi, et al., 2018)..

2.4.3 Grain structure during deformation

The study on the deformation behavior of the LPBF-MS1 shows a very weak fiber texture in the as-built condition. The absence of a strong texture is mainly related to the rotation of laser source between layers, and subsequently the rotation of heat flow, resulting

in the almost random orientation of grains (Suryawanshi, et al., 2017). Upon tensile loading, a preferred texture was developed as a rotated cube texture. The texture development was identically observed in both cases of powder layer thickness, and the deformation behavior was independent of the layer thickness in the LPBF-MS1. Therefore, the same deformation behavior can also be achieved by increasing the layer thickness to LPBF-MS1-50; see (Hadadzadeh, et al., 2018) (Thijs, et al., 2011) (Jia, et al., 2014) (Jägle, et al., 2014). As mentioned above, the grain morphology and orientation, as well as the solidification structure, were not altered by changing the layer thickness to 50µm. Indeed, the microstructural features were preserved at higher layer thicknesses resulting in similar mechanical properties along with deformation behavior under uniaxial tensile loading. Consequently, using the 50µm layer thickness can be considered as the modification of process parameters since a more efficient LPBF process can be conducted in terms of manufacturing time and cost, while keeping microstructural and mechanical properties the same (Xu, et al., 2019) (Masoumi, et al., 2016) (Figueiredo, et al., 2019) (Hadadzadeh, et al., 2020).

2.5 Conclusions

In this paper, a thorough investigation of the characteristics of gas atomized maraging steel (MS1) powder was studied as well as the additively manufactured cubes and bars with two powder layer thicknesses. The following conclusions based on the experimental results obtained in this investigation can be drawn:

Porosity and hardness study showed a steady property beneath the outer layer of the additively manufactured core section. The results showed consistent and similar properties for both powder layer thicknesses.

Austenite percentage decreased during the manufacturing process, while the phases seemed to be less affected by powder layer thickness.

The deformed samples showed a textured matrix and the grains were elongated in the same direction of deformation, while directional growth of grains was observed for the as-built samples.

Martensite laths observed in the TEM micrographs showed no evidence of segregation of alloying elements at the cell boundaries. Instead, spherical shaped oxide and nitride of aluminum and titanium were observed in the matrix, respectively.

The use of optimum process parameters including the laser scan speed, laser power, hatch distance as well as powder layer thickness resulted in uniform melt pools along with consistent grains in terms of shape and size in all the LPBF-MS1 samples. Columnar dendrites were observed around the melt pool boundaries and equiaxed cells in the core of the melt pools.

In all aspects of this study, the change in powder layer thickness resulted in either identical properties or slightly different with a higher advantage of lower powder layer thickness. By increasing the powder layer thickness from 40μm to 50μm, the manufacturing process is much faster, and the resulting product is cheaper at the same time. Although, the mechanical properties can be kept almost the same with this increase.

2.6 References

Aboulkhair N. T. [et al.] Reducing porosity in AlSi10Mg parts processed by selective laser melting [Journal] // Additive Manufacturing. - 2014. - Vol. 1. - pp. 77-86.

Asgari H. [et al.] On microstructure and mechanical properties of additively manufactured AlSi10Mg_200C using recycled powder [Journal] // Materials Science and Engineering: A. - 2017. - Vol. 707. - pp. 148-158.

Asgari H. and Mohammadi M. Microstructure and mechanical properties of stainless steel CX manufactured by Direct Metal Laser Sintering [Journal] // Materials Science and Engineering: A. - 2018. - Vol. 709. - pp. 82-89.

Bai Y. [et al.] Influence mechanism of parameters process and mechanical properties evolution mechanism of maraging steel 300 by selective laser melting [Journal] // Materials Science and Engineering: A. - 2017. - Vol. 703. - pp. 116-123.

Bertoli U. S. [et al.] On the limitations of volumetric energy density as a design parameter for selective laser melting [Journal] // Materials & Design. - 2017. - Vol. 113. - pp. 331-340.

Bhardwaj T. and Shukla M. Effect of laser scanning strategies on texture, physical and mechanical properties of laser sintered maraging steel [Journal] // Materials Science and Engineering: A. - 2018. - Vol. 734. - pp. 102-109.

Bodziak S. [et al.] Precipitation in 300 grade maraging steel built by selective laser melting: Aging at 510 C for 2 h [Journal] // Materials Characterization. - 2019. - Vol. 151. - pp. 73-83.

Casalino G. [et al.] Experimental investigation and statistical optimisation of the selective laser melting process of a maraging steel [Journal] // Optics & Laser Technology. - 2015. - Vol. 65. - pp. 151-158.

Casati R. [et al.] Aging behaviour and mechanical performance of 18-Ni 300 steel

processed by selective laser melting [Journal] // Metals. - 2016. - Vol. 6(9). - p. 218.

Chakravarthi K. V. A. [et al.] Microstructure, properties and hot workability of M300 grade maraging steel [Journal] // Defence technology. - 2018. - Vol. 14(1). - pp. 51-58.

Chen G. [et al.] A comparative study of Ti-6Al-4V powders for additive manufacturing by gas atomization, plasma rotating electrode process and plasma atomization [Journal] // Powder technology. - 2018. - Vol. 333. - pp. 38-46.

Croccolo D. [et al.] Influence of the build orientation on the fatigue strength of EOS maraging steel produced by additive metal machine [Journal] // Fatigue & Fracture of Engineering Materials & Structures. - 2016. - Vol. 39(5). - pp. 637-647.

Cyr E. [et al.] Fracture behaviour of additively manufactured MS1-H13 hybrid hard steels [Journal] // Materials Letters. - 2018. - Vol. 212. - pp. 174-177.

de Souza A. F. [et al.] Effect of laser speed, layer thickness, and part position on the mechanical properties of maraging 300 parts manufactured by selective laser melting [Journal] // Materials Science and Engineering: A. - 2019. - Vol. 767.

Dharmendra C. [et al.] Microstructural evolution and mechanical behavior of nickel aluminum bronze Cu-9Al-4Fe-4Ni-1Mn fabricated through wire-arc additive manufacturing [Journal] // Additive Manufacturing. - 2019. - Vol. 30. - p. 100872.

Dilip J. J. S. [et al.] Selective laser melting of HY100 steel: process parameters, microstructure and mechanical properties [Journal] // Additive Manufacturing. - 2017. - Vol. 13. - pp. 49-60.

Dos Reis A. G. [et al.] High-temperature creep resistance and effects on the austenite reversion and precipitation of 18 Ni (300) maraging steel [Journal] // Materials Characterization. - 2015. - Vol. 107. - pp. 350-357.

Ebrahimi A. and Mohammadi M. Numerical tools to investigate mechanical and fatigue properties of additively manufactured MS1-H13 hybrid steels [Journal] // Additive

Manufacturing. - 2018. - Vol. 23. - pp. 381-393.

Figueiredo N. C. [et al.] Microstructural variations at different distance from the surface in forged 18 Ni C300 maraging steel [Journal] // Journal of Materials Research and Technology. - 2019. - Vol. 8(1). - pp. 284-291.

Galindo-Nava E. I. and Rivera-Díaz-del-Castillo P. E. J. Understanding the factors controlling the hardness in martensitic steels [Journal] // Scripta Materialia,. - 2016). - Vol. 110. - pp. 96-100.

Gong H. [et al.] Analysis of defect generation in Ti–6Al–4V parts made using powder bed fusion additive manufacturing processes [Journal] // Additive Manufacturing. - 2014. - Vol. 1. - pp. 87-98.

Gu D. D. [et al.] Laser additive manufacturing of metallic components: materials, processes and mechanisms [Journal] // International materials reviews. - 2012. - Vol. 57(3). - pp. 133-164.

Guan K. [et al.] Effects of processing parameters on tensile properties of selective laser melted 304 stainless steel [Journal] // Materials & Design. - 2013. - Vol. 50. - pp. 581-586.

Hadadzadeh A. [et al.] Microstructural investigation and mechanical behavior of a two-material component fabricated through selective laser melting of AlSi104Mg on an Al-Cu-Ni-Fe-Mg cast alloy substrate [Journal] // Additive Manufacturing. - 2019. - p. 100937.

Hadadzadeh A. [et al.] Strengthening mechanisms in direct metal laser sintered AlSi10Mg: Comparison between virgin and recycled powders [Journal] // Additive Manufacturing. - 2018. - Vol. 23. - pp. 108-120.

Hadadzadeh C. Dharmendra A. [et al.] Deformation mechanisms and fracture of electron beam melted Ti–6Al–4V [Journal] // Materials Science and Engineering: A. - 2020. - Vol. 771. - p. 138652.

Hall A. M. and Slunder C. J. The metallurgy, behavior, and application of the 18-percent nickel maraging steels [Journal] // BATTELLE MEMORIAL INST COLUMBUS OH COLUMBUS LABS. - 1968. - Vols. No. NASA-SP-5051.

Jägle E. [et al.] Comparison of maraging steel micro-and nanostructure produced conventionally and by laser additive manufacturing [Journal] // Materials,. - 2016. - Vol. 10(1). - p. 8.

Jägle E. A. [et al.] Precipitation and austenite reversion behavior of a maraging steel produced by selective laser melting [Journal] // Journal of Materials Research. - 2014. - Vol. 29(17). - pp. 2072-2079.

Jia Q. and Gu D. Selective laser melting additive manufacturing of Inconel 718 superalloy parts: Densification, microstructure and properties [Journal] // Journal of Alloys and Compounds. - 2014. - Vol. 585. - pp. 713-721.

Joshi J. R. [et al.] A comparative evaluation of microstructural and mechanical behavior of fiber laser beam and tungsten inert gas dissimilar ultra high strength steel welds [Journal] // Defence Technology. - 2016. - Vol. 12(6). - pp. 464-472.

Kempen K. [et al.] Microstructure and mechanical properties of Selective Laser Melted 18Ni-300 steel [Journal] // Physics Procedia. - 2011. - Vol. 12. - pp. 255-263.

Kodama H. Automatic method for fabricating a three-dimensional plastic model with photo-hardening polymer [Journal] // Review of scientific instruments. - 1981. - Vol. 52(11). - pp. 1770-1773.

Kruth J. P. [et al.] Basic powder metallurgical aspects in selective metal powder sintering [Journal] // CIRP annals. - 1996. - Vol. 45(1). - pp. 183-186.

Kruth J. P. Material incress manufacturing by rapid prototyping techniques [Journal] // CIRP annals. - 1991. - Vol. 40(2). - pp. 603-614.

Kruth J. P., Leu M. C. and Nakagawa T. Progress in additive manufacturing and rapid

prototyping [Journal] // Cirp Annals. - 1998. - Vol. 47(2). - pp. 525-540.

Kučerová L., Zetková, I., Jandová A. and Bystrianský M. Microstructural characterisation and in-situ straining of additive-manufactured X3NiCoMoTi 18-9-5 maraging steel [Journal] // Materials Science and Engineering: A. - 2019. - Vol. 750. - pp. 70-80.

Kürnsteiner P. [et al.] Massive nanoprecipitation in an Fe-19Ni-xAl maraging steel triggered by the intrinsic heat treatment during laser metal deposition [Journal] // Acta Materialia. - 2017. - Vol. 129. - pp. 52-60.

Lang F. H. and Kenyon N. Welding of maraging steels [Book]. - [s.l.] : Welding Research Council, 1971.

Masoumi M. [et al.] Effect of microstructure and crystallographic texture on the Charpy impact test for maraging 300 steel [Journal] // Materials Characterization. - 2016. - Vol. 120. - pp. 203-209.

Material data sheet EOS Maraging Steel MS1 [Journal] // EOS GmbH - Electro Optical Systems. - München : [s.n.], 2017.

Meyers M. A. and Chawla K. K. Mechanical behavior of materials [Book]. - [s.l.] : Cambridge university press, 2008.

Mills K., Davis J. R. and Destefani J. D. Metals Handbook, Vol. 12. Fractography [Book]. - [s.l.] : ASM International, 1987.

Mohammadi M. and Asgari H. Achieving low surface roughness AlSi10Mg_200C parts using direct metal laser sintering [Journal] // Additive Manufacturing. - 2018. - Vol. 20. - pp. 23-32.

Murty S. N., Manwatkar S. K. and Narayanan P. R. Metallurgical analysis of a failed maraging steel shear screw used in the band separation system of a satellite launch vehicle [Journal] // Defence technology. - 2016. - Vol. 12(5). - pp. 380-387.

Mutua J. [et al.] Optimization of selective laser melting parameters and influence of post heat treatment on microstructure and mechanical properties of maraging steel [Journal] // Materials & Design. - 2018. - Vol. 139. - pp. 486-497.

Niu M. [et al.] Precipitate evolution and strengthening behavior during aging process in a 2.5 GPa grade maraging steel [Journal] // Acta Materialia. - 2019. - Vol. 179. - pp. 296-307.

Qian F., Sharp J. and Rainforth W. M. Microstructural evolution of Mn-based maraging steels and their influences on mechanical properties [Journal] // Materials Science and Engineering: A. - 2016. - Vol. 674. - pp. 286-298.

Rajkumar K. V. [et al.] Characterization of aging behaviour in M250 grade maraging steel using eddy current non-destructive methodology [Journal] // Materials Science and Engineering: A. - 2007. - Vols. 464(1-2). - pp. 233-240.

Rajkumar V., Arivazhagan N. and Ramkumar K. D. Studies on welding of maraging steels [Journal] // Procedia Engineering. - 2014. - Vol. 75. - pp. 83-87.

Saha G. C. and Khan T. I. Comparative abrasive wear study of HVOF coatings obtained by spraying WC-17Co microcrystalline and duplex near-nanocrystalline cermet powders [Journal] // Journal of Engineering Materials and Technology. - 2011. - Vol. 133(4). - p. 041002.

Sakai P. R. [et al.] Comparison of Mechanical and Microstructural Characteristics in Maraging 300 Steel Welded by three different processes: LASER, PLASMA and TIG [Journal] // Procedia Engineering. - 2015. - Vol. 114. - pp. 291-297.

Schneider C. A., Rasband W. S. and Eliceiri K. W. NIH Image to ImageJ: 25 years of image analysis [Journal] // Nature methods. - 2012. - Vol. 9(7). - p. 671.

Sha Wei and Guo Zhanli Maraging Steels, Modeling of Microstructure, Properties and Applications [Book]. - [s.l.] : Woodhead Publishing, 2009.

Shakerin S. [et al.] Additive manufacturing of maraging steel-H13 bimetals using laser powder bed fusion technique [Journal] // Additive Manufacturing. - 2019. - Vol. 100797.

Small K. B., Englehart D. A. and Christman T. A. Etching specialty alloys [Journal] // Advanced materials & processes. - 2008. - Vol. 33.

Standard A. S. T. M. ASTM E8/E8M-15a [Journal] // Standard Test Methods for Tension Testing of Metallic Materials. - 2015.

Suryawanshi J., Prashanth K. G. and Ramamurty U. Tensile, fracture, and fatigue crack growth properties of a 3D printed maraging steel through selective laser melting [Journal] // Journal of Alloys and Compounds. - 2017. - Vol. 725. - pp. 355-364.

Tan C. [et al.] Microstructural evolution, nanoprecipitation behavior and mechanical properties of selective laser melted high-performance grade 300 maraging steel [Journal] // Materials & Design,. - 2017. - Vol. 134. - pp. 23-34.

Tang M., Pistorius P. C. and Beuth J. L. Prediction of lack-of-fusion porosity for powder bed fusion [Journal] // Additive Manufacturing. - 2017. - Vol. 14. - pp. 39-48.

Tapia G., Elwany A. H. and Sang H. Prediction of porosity in metal-based additive manufacturing using spatial Gaussian process models [Journal] // Additive Manufacturing. - 2016. - Vol. 12. - pp. 282-290.

Thijs L. [et al.] Investigation on the inclusions in maraging steel produced by Selective Laser Melting [Journal] // Innovative Developments in Virtual and Physical Prototyping. - 2011. - pp. 297-304.

Van der Schueren B. and Kruth J. P. Powder deposition in selective metal powder sintering [Journal] // Rapid Prototyping Journal. - 1995. - Vol. 1(3). - pp. 23-31.

Viswanathan U. K., Dey G. K. and Sethumadhavan V. Effects of austenite reversion during overageing on the mechanical properties of 18 Ni (350) maraging steel [Journal] //

Materials Science and Engineering: A. - 2005. - Vols. 398(1-2). - pp. 367-372.

Wang D. [et al.] Investigation of crystal growth mechanism during selective laser melting and mechanical property characterization of 316L stainless steel parts [Journal] // Materials & Design. - 2016. - Vol. 100. - pp. 291-299.

Xu X. [et al.] Improving mechanical properties of wire plus arc additively manufactured maraging steel through plastic deformation enhanced aging response [Journal] // Materials Science and Engineering: A. - 2019. - Vol. 747. - pp. 111-118.

Xu X. [et al.] Microstructural evolution and mechanical properties of maraging steel produced by wire+ arc additive manufacture process [Journal] // Materials Characterization. - 2018. - Vol. 143. - pp. 152-162.

Zhong Y. [et al.] Intragranular cellular segregation network structure strengthening 316L stainless steel prepared by selective laser melting [Journal] // Journal of Nuclear Materials. - 2016. - Vol. 470. - pp. 170-178.

Chapter 3

Plastic deformation throughout strain-induced phase transformation in additively manufactured maraging steels

Abstract

A comprehensive study was intended to show the microstructural features of additively manufactured (AM) 18Ni-300 maraging steel. Uniaxial tensile tests were conducted on specimens built using laser powder bed fusion (LPBF) technique for two different powder layer thicknesses. The specimens were built to have the lowest possible porosity, and tensile tests showed two stages of strain hardening. In stage I, the dislocation density increased, leading to a positive strain hardening rate. A negative strain hardening rate due to the necking effect was then followed in stage II. X-ray diffraction (XRD) analyses revealed a phase transformation through the deformation. Various analyses via electron backscattered diffraction (EBSD) technique was then conducted with large scans over three different zones representing undeformed, deformed, and severely deformed close to the fracture area. The pole figures and orientation distribution functions (ODF) revealed a texture evolving through the deformation process in agreement with the kernel average misorientation (KAM) and grain boundary maps. Transmission electron microscopy (TEM) was used to detect the inclusions and segregated alloying elements adjacent to the fractured surfaces. Results indicated that the deformation led to diminishing the austenite (γ) phase, while the transformed austenite sourced the high dislocation density area at cell boundaries.

Keywords: 18Ni-300 Maraging steel; Laser powder bed fusion (LPBF); layer thickness; austenite (γ); martensite ($\acute{\alpha}$)

3.1 Introduction

Additively manufactured (AM) maraging steels have been recently received considerable attention due to their superior mechanical properties as well as their excellent manufacturability (Sha, et al., 2009). Coexistence of the martensite (ά) phase and well-dispersed nano-precipitates results in ultra-high-strength and hardenability accompanied by a high level of machinability, which is attractive to the automotive and aerospace industries (Rajkumar, et al., 2014). Over the last couple of years, the progress in laser additive manufacturing in terms of machine capabilities and process parameters has led to the development of products with exceptional mechanical properties compared to conventional counterparts (Shamsaei, et al., 2015). In this regard, optimization of the process parameters brings a higher probability of soundness in the product by lowering the volume fraction of structural defects, e.g. hot cracking, keyholes, shrinkage, and gas porosities (Mohammadi, et al., 2018).

In AM maraging steels, reheating cycles during consecutive powder layer depositions induces a quasi-dynamic aging phenomenon (Tan, et al., 2017). This artificial aging results in the formation of fine precipitates through the heat-affected zones, and subsequently, higher strength of the as-built AM product compared to the conventionally cast parts (Suryawanshi, et al., 2017). Despite the comprehensive studies on the heat-treated AM samples (Tan, et al., 2017), (Suryawanshi, et al., 2017), (Cyr, et al., 2018) and (Xu, et al., 2018), the microstructural and mechanical behavior of the as-built products has been overlooked. The as-built product mainly contains the body-centred cubic (BCC) martensite (ά) and a small fraction of the face-centred cubic (FCC) austenite (γ) phase (Tan, et al., 2017). According to the Fe-Ni phase diagram, at almost 18 wt% Ni, γ is thermodynamically

stable over a wide temperature range between the peritectic (1716°C) and eutectoid (688°C) transformations, while the ά phase is expected to athermally form from γ at temperatures below 870°C (Dos Reis, et al., 2015) and (ASM, 1991). Due to the high contents of Ni as a strong γ-stabilizer and ultra-high cooling rate during laser powder bed fusion (LPBF), a small portion of retained γ is always expected to remain at ambient temperatures (Xu, et al., 2018). This phase can be nucleated and grown during the aging process as well, known as reverted γ (Jägle, et al., 2014). The higher amount of reverted austenite results in higher ductility and toughness and prevents premature failure (Yuan, et al., 2012). The amount of retained γ inversely affects the strength and hardness of the as-built maraging steel, increases its ductility (Wang, et al., 2014) (Shamsdini, et al., 2020). The plastic deformation, on the other side, can also cause γ→ά transformation (Martin, et al., 2016) (Emadoddin, et al., 2011). The strain-induced phase change, also known as transformation induced plasticity (TRIP), was previously studied in the Fe-Cr-C system, and the role of reverted austenite on stopping cracks from penetrating the martensite laths was discussed (Yuan, et al., 2012).

The AM maraging steels typically show a hierarchical grain structure, where the ά laths form inside the prior austenite grains (PAG) in the style of blocks and packets (Galindo-Nava, et al., 2015) (Morsdorf, et al., 2015). Besides, a synergy between consecutive reheating cycles and rapid cooling during the LPBF process leads the grains to grow along the build direction and perpendicular to the melt-pool boundaries (Shakerin, et al., 2019) (Asgari, et al., 2017). This directional growth leads to anisotropy, which is another reason for higher mechanical strength perpendicular to the building direction compared to the conventional manufacturing methods (Hadadzadeh, et al., 2018). The plastic deformation

as another factor affecting the grain structure is also needed to take into account. Multiple studies have been conducted to discuss the effects of texture evolution during deformation in 18Ni maraging steels (Dos Reis, et al., 2015) (Ahmed, et al., 1994) (Béreš, et al., 2017) (Figueiredo, et al., 2019). Reis et al. (Dos Reis, et al., 2015) observed the martensite to austenite phase transformation due to creep for 18Ni maraging steel resulting in ductile failure. Ahmed et al. (Ahmed, et al., 1994) performed a deformation study on cold-rolled 18Ni maraging steel studying the magnetic properties due to phase transformation. Beres et al. (Béreš, et al., 2017) investigated the hydrogen embrittlement of maraging steels and concluded that the austenite grain size affects the failure mechanism. Figueiredo et al. (Figueiredo, et al., 2019) studied the texture of the forged 18Ni maraging steel in different depths from the forged surface. They observed an increase in the α and γ fibres with increasing depth as well as the lowest strain in the surface.

Due to the novelty of the AM process compared to conventional manufacturing methods, a thorough study on the deformation of additively manufactured products is needed. The mutual effect of the AM process and plastic deformation on the strain-induced phase transformation and mechanical behavior of the as-built AM 18Ni-300 maraging steel has been conducted in the current study. In order to investigate the role of the AM process, the powder layer thickness is chosen as a variable parameter, while the effect of plastic deformation is recognized by employing the uniaxial tensile testing. Since the volume fraction of retained γ is different between the AM and conventionally cast steels (Xu, et al., 2018), the TRIP effect of the AM 18Ni-300 maraging steel is necessary to be evaluated. Thus, a thorough study on the strain-induced phase transformation in the as-built 18Ni-300 maraging steel is investigated in this research.

3.2 Experimental procedure

3.2.1 Material and manufacturing process

Gas atomized 18Ni-300 maraging steel powder was deposited to produce horizontally printed cylindrical bars via an EOS M290 machine. The chemical composition of the powder is given in Table 3.1. A scanning beam with 100 µm spot size was emitted by a 400 W Yb-fiber gun during the manufacturing process, and pure nitrogen gas (99.999 %) was continuously purged into the chamber. The LPBF technique was chosen to deposit and fuse powder layers on a build plate preheated at 40°C, where a 67° strip scanning strategy was applied between successive layers. Powder deposition was carried out at two powder layer thicknesses of 40 µm and 50 µm (designated as LPBF-40 and LPBF-50) to fabricate the cylindrical bars with 12 mm and 120 mm in diameter and length, respectively. The laser power and scanning speed used for LPBF-40 samples were 285 W and 960 mm/s, while the LPBF-50 samples were made using 305 W power and 1010 mm/s scanning speed. The hatch distancing of 110 µm was used for both cases.

A mapping technique was used to measure the porosity. In this method, the polished surface's optical microscopy (OM) image was analyzed and based on the contrast between the base metal and the pores, the porosity fraction was calculated. High magnification images were collected through a Zeta-20 OM, and the area fraction was measured over the entire surface. The top surface was ground and polished, and the measurement was conducted over multiple layers through the depth. The average value was reported as the overall porosity level.

Table 3.1 Chemical composition of the powder used in the DMLS process (Material Data sheet, 2017)

Element	Fe	Ni	Co	Mo	Ti	Al	Cr	Cu	C	Mn	Si	P	S
Max %	Bal.	19	9.5	5.2	0.8	0.15	0.5	0.5	0.03	0.1	0.1	0.01	0.01
Min %	Bal.	17	8.5	4.5	0.6	0.05							

3.2.2 Sample preparation and tensile testing

Specimens for the uniaxial tensile testing were machined according to the E8/E8M ASTM standard (Standard, 2015). Through a quasi-static strain rate, the tensile tests were performed using a universal hydraulic Instron 1332 machine. The elongation was measured using a 25mm extensometer at a 9×10-3 s-1 strain rate, and the tests were conducted at room temperature. As shown in Fig. 3-1, the building direction along the z-axis was perpendicular to the loading direction. Samples were cross-sectionally cut into three pieces of undeformed (zone A), deformed (zone B), and severely deformed (zone C) via an electrical discharge machine (EDM). In this regard, the undeformed piece was collected from the part fixed within the grips, while the deformed and severely deformed pieces were taken from locations near the gauge shoulder and fracture area. Afterward, samples were mounted, ground through 300-4000 grits SiC sandpapers, and regularly polished using 6.0-0.05 μm polish cloths.

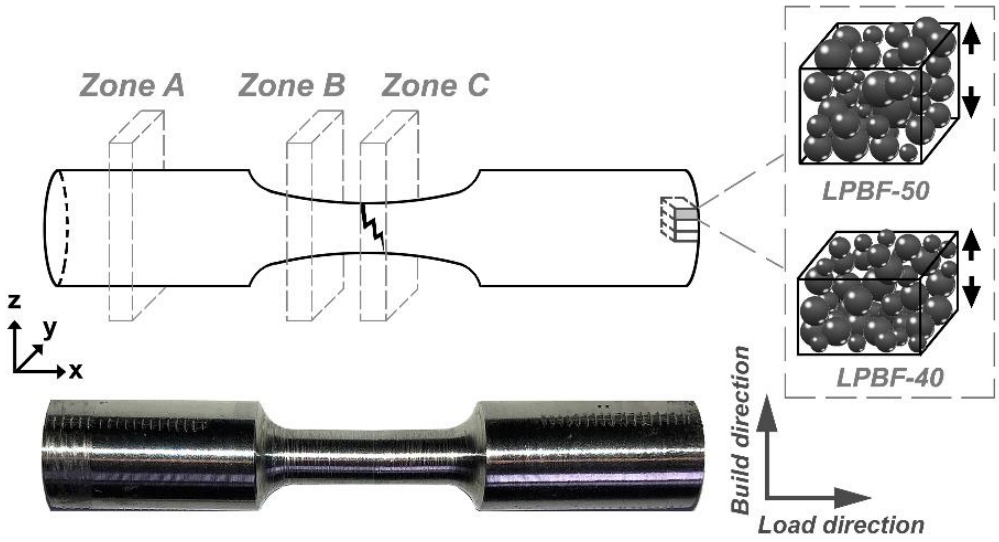

Fig. 3-1 Schematic design of the tensile test sample showing the powder layer thickness.

3.2.3 Phase identification

X-ray diffraction (XRD) technique was used to identify phases in the samples collected from A and C zones. A Brucker D8 instrument with a Co-K_α radiation source working at 45 mA and 35 kV was used to collect the data over $45<2\theta<130°$ with a rotation speed of 60 deg./min, and the intensity of peaks was measured using the Rietveld analysis technique.

3.2.4 Electron microscopy

EBSD measurements were conducted using an FEI QuantaTM 450 FEG-SEM microscope to study the grain size and orientation and the area fraction of low- and high-angle grain boundaries (LAGBs and HAGBs) in zones A, B, and C. The EBSD studies were carried over a zone within $1400 \times 500\ \mu m^2$ with a step size of 500 nm located at the x-y plane specified in Fig. 3-1. The diffraction patterns were also collected using the TSL® OIM data collection software and were post-processed by the OIM data analysis software. The crystallographic textures were calculated by harmonic series expansion with truncation at L=16. Regarding the transmission electron microscopy (TEM), an FEI Helios NanoLab

650 dual beam instrument was utilized to collect a thin piece of the sample at the vicinity of the fracture area (zone C). The effect of plastic deformation on the volume fraction of the γ phase was assessed in detail with an FEI Tecnai Osiris TEM apparatus that was equipped with a 200keV X-FEG gun.

3.3 Results

Fig. 3-2 shows the OM micrographs of the polished surfaces along with the average porosity levels. Fig. 3-2 (a) shows the LPBF-40 sample with a low fraction of porosity, while Fig. 3-2 (b) shows the LPBF-50 sample with a higher average porosity level compared to the former case. In both cases, the pores sizes are very small (under 50 µm), and the overall porosity level shows an almost fully dense material.

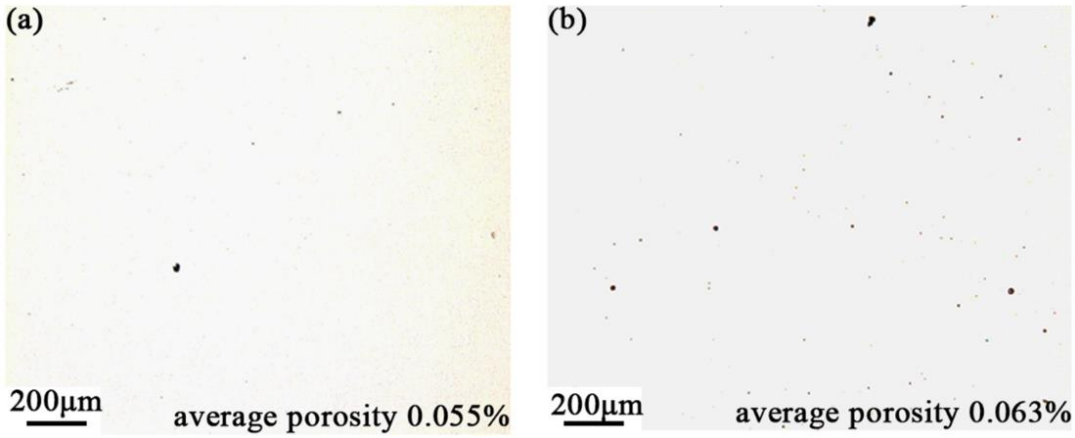

Fig. 3-2 OM micrographs showing porosity in (a): LPBF-40, (b): LPBF-50.

Fig. 3-3 shows the true stress-strain and strain hardening curves for the LPBF-40 and LPBF-50 samples. The LPBF-40 sample elucidates a combination of the higher ultimate tensile strength (UTS) and better ductility, which brings higher energy absorption before failure. The total strain and UTS values in the LPBF-40 and LPBF-50 are almost 14.39% - 1278 MPa and 11.76% - 1265 MPa, respectively. However, their stress-strain curves present a consistency within the initial 4 % elongation, where the materials are exposed to

elastic-homogeneous plastic loading condition. The difference in elongation percentage has mostly occurred after the peak stress, where the structural defects such as porosities and microcracks start to nucleate, coalesce and grow. It seems that the LPBF-40 structure is more integrated than the LPBF-50 one. As another observation, the LPBF-50 sample shows a sharp drop in its stress values right before the fracture. This trend was reported by Rusinek and Martinez (Rusinek, et al., 2009) as a deformation step in which a high volume fraction of porosities is being coalesced to form micro-voids. In the current study, a slight increase in the tensile strength compared to the literature was achieved, which is presented in Fig. 3-4 (Tan, et al., 2017), (Dehgahi, et al., 2020), (Kučerová, et al., 2019), and (Bhardwaj, et al., 2018). In this Figure, ultimate tensile strength versus the fracture strain is presented for 18Ni-300 maraging steels produced using both additive and conventional manufacturing techniques.

Due to the highly anisotropic texture resulted from the directional grain structure, the AM products typically show higher strength than those conventionally cast and solidified (Kučerová, et al., 2019). By focusing on the strain hardening curves, it is confirmed that change in the powder layer thickness does not affect the rate of strain hardening; however, it just shifts the critical point of $d\sigma/d\varepsilon = 0$ from 6 % strain in the LPBF-40 sample to 4 % in the LPBF-50 one. This point is following the peak stress where a balance between strain hardening and geometric softening takes place.

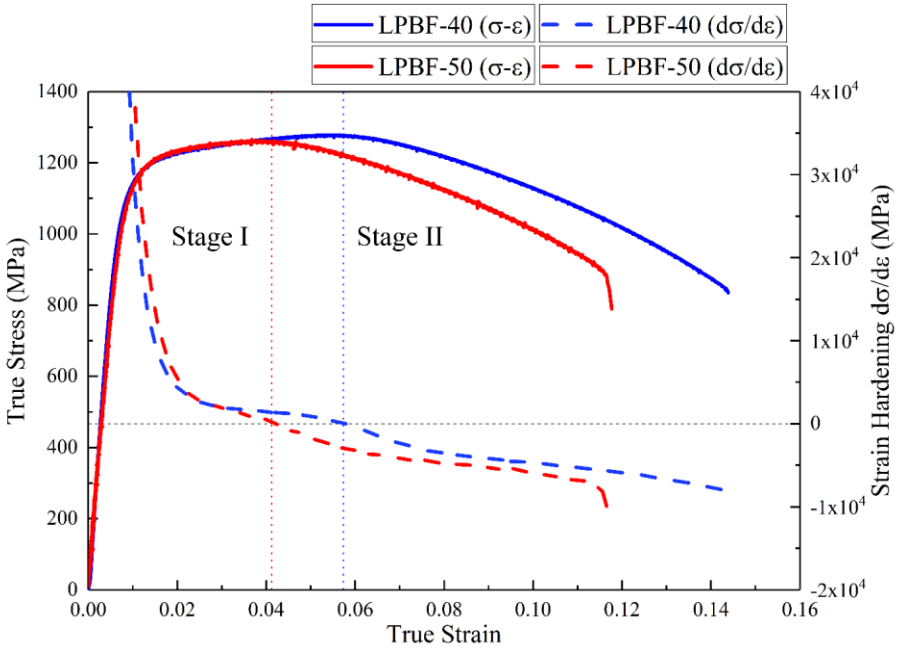

Fig. 3-3 Tensile stress-strain curves and the corresponding strain hardening variation

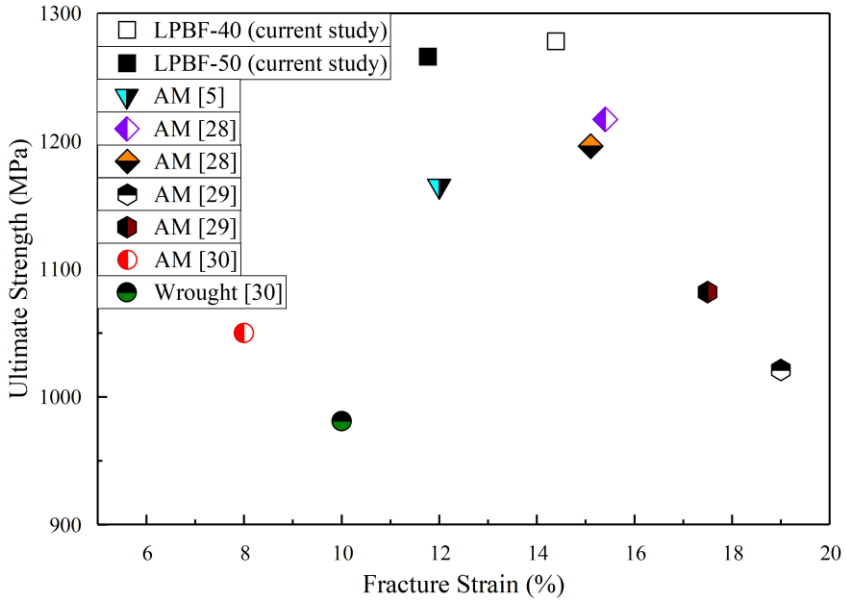

Fig. 3-4 Ultimate tensile strength versus fracture strain for 18Ni-300 maraging steels produced using both additive and conventional manufacturing techniques (Tan, et al., 2017), (Dehgahi, et al., 2020), (Kučerová, et al., 2019), and (Bhardwaj, et al., 2018).

Fig. 3-5 illustrates the EBSD results of the LPBF-40-A and LPBF-50-A samples, including inverse pole figures, orientation distribution function (ODF), and pole figures (PF) of the texture analyses. The inverse pole figures show the melt-pool boundaries (curved dash lines) and the crystallographic orientation of grains over a large scan area. The orientation is random for both cases, which can be attributed to grains renucleation during repetitive reheating cycles. As a comparison between two structures, the LPBF-40-A contains a combination of grains oriented along the <100> and <111> directions, while the LPBF-50-A reveals a higher fraction of grains preferentially oriented along the <001> direction. The (001) pole figures in Fig. 3-5 (c, d) show peaks in the center in both cases. The pole figures are in agreement with the ODF plots shown in Fig. 3-5 (e, f). In Fig. 3-5 (e, f), highly intensified components of {100} θ-fibre are observed. The {111} γ-fibre components are intensified in the LPBF-40-A samples. However, the LPBF-50-A shows weaker γ-fibre components comparatively.

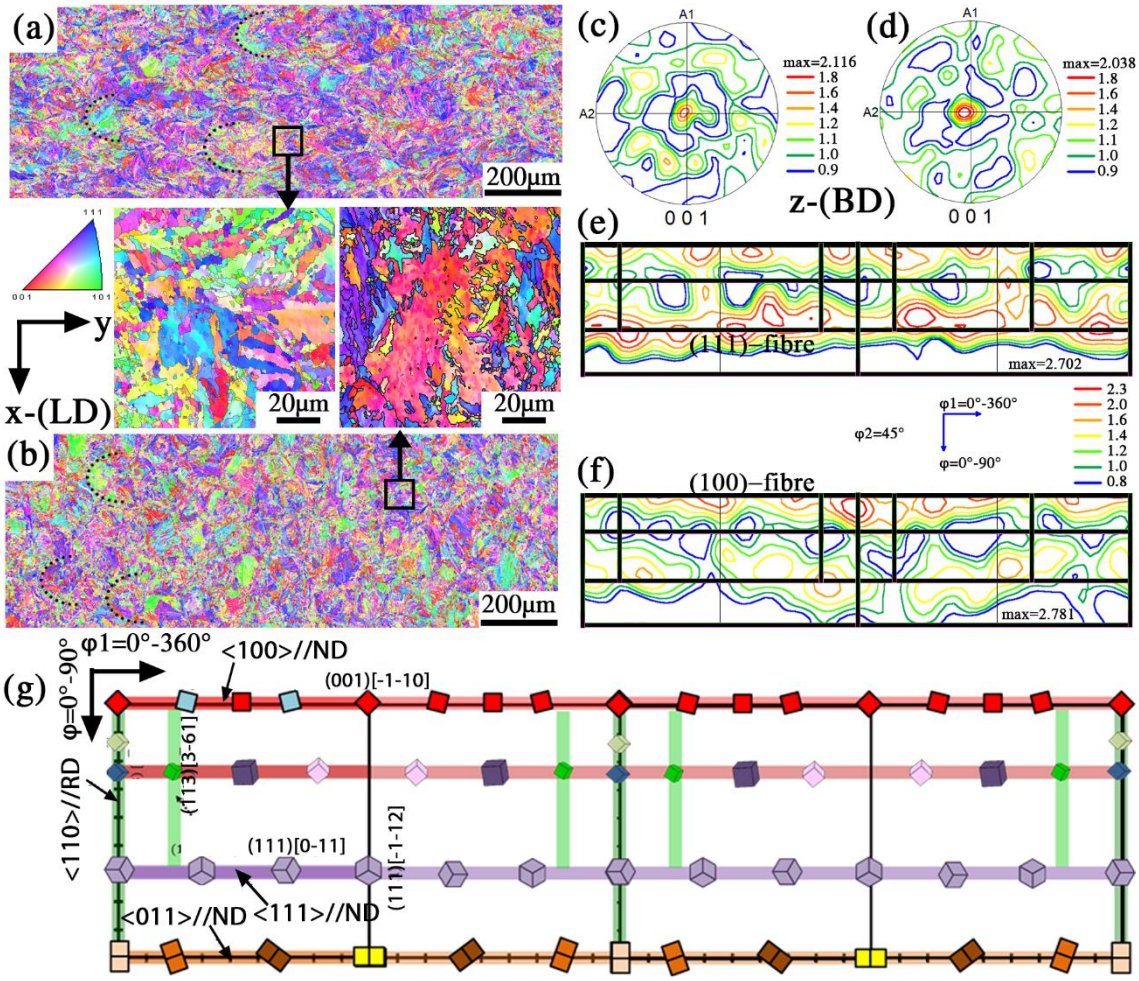

Fig. 3-5 (a, b): IPF for LPBF-40-A, LPBF-50-A, (c, d): Pole figures for LPBF-40-A and LPBD-50-A, (e, f): ODF for LPBF-40-A, LPBF-50-A, (g): ODF key components (Sanjari, et al., 2017).

Fig. 3-6 shows the XRD patterns for the undeformed and severely deformed samples for both cases of powder layer thickness. The LPBF-40-A sample is reported to have a lower γ volume fraction (4.6 %) than the LPBF-50-A case (5.1 %). The γ peaks shown in Fig. 3-6 have been disappeared in the LPBF-C samples, in agreement with the elimination of the γ phase through the strain-induced γ→ά phase transformation. It is noteworthy that, no traces of hcp-martensite were depicted in the XRD patterns (Martin, et al., 2016). Although the maraging steel used in the current study has a substantially high percentage of alloying elements, it shows γ to the ά phase transformation due to plastic strain, similar

to the low alloy ferritic bainitic steels (L-TRIP) (Fischer, et al., 2000). It turns out that a strain-induced transformation can also prevent premature failure, while a complete transformation of γ to ά may occur in lower strains (Yuan, et al., 2012) and (Wang, et al., 2014). Similarly, in the current study, the material has gone through a complete phase transformation before the fracture.

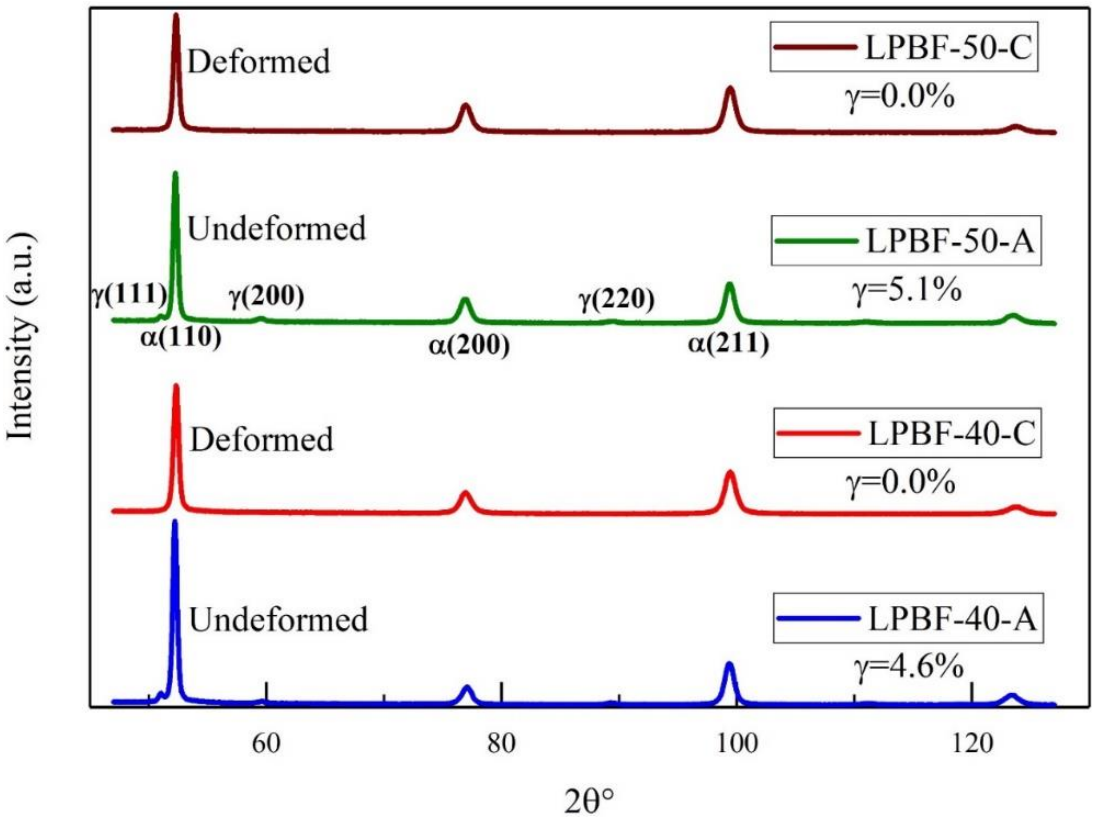

Fig. 3-6 XRD pattern for the 18Ni-300 deformed and undeformed samples in zones A and C.

Fig. 3-7 shows the collected EBSD data of zone B near the gauge shoulder, which is partially exposed to plastic deformation. Melt-pools are identified and marked in Fig. 3-7 (a, b) by curved dash lines. The size of the melt-pools is the same as those observed in zone A (Fig. 3-5). Like the undeformed cases in Fig. 3-5, components of the θ-fibre{100} and γ-fibre{111} are observed in the zone-B for both LPBF-40 and LPBF-50 samples. Although the pole figures that are shown in Fig. 3-7 (c) and (d) look similar, the intensities

are weaker in the zone-B compared to zone-A (see Fig. 3-5). The {111} components observed in the ODF plot in Fig. 3-7 (e, f) are similar for both LPBF-40 and LPBF-50 cases and agree with the pole figure plots showing similar grain orientation for LPBF-40-B and LPBF-50-B samples.

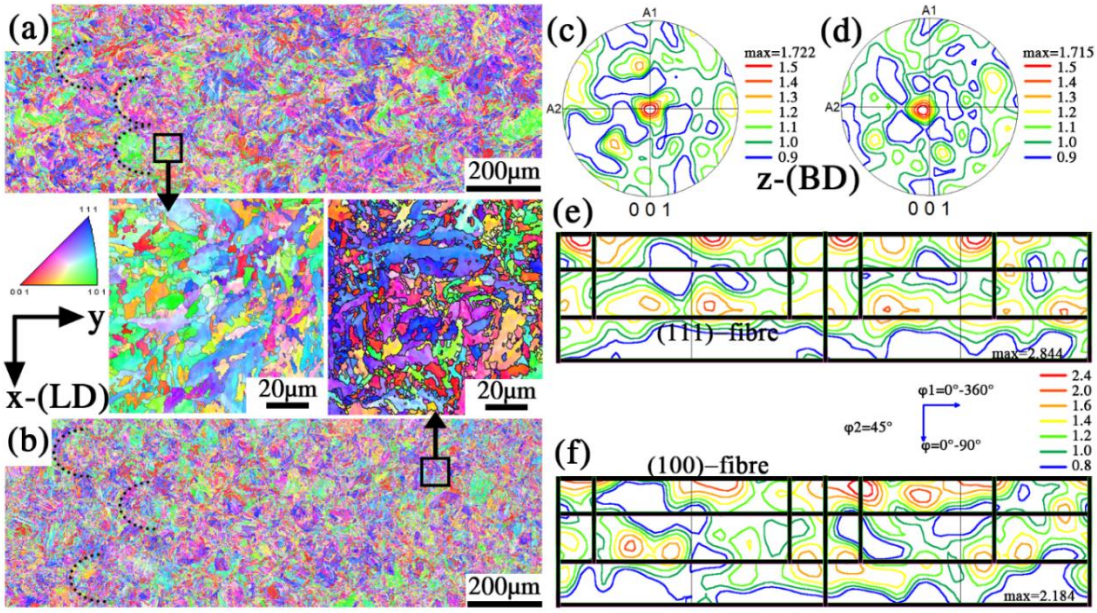

Fig. 3-7 (a, b): IPF for LPBF-40-B, LPBF-50-B, (c, d): Pole figures for LPBF-40-B and LPBD-50-B, (e, f): ODF for LPBF-40-B, LPBF-50-B.

Fig. 3-8 represents collective EBSD data of zone C, which is neighbouring to the fracture area. As shown in Fig. 3-8 (a, b), the grains are drawn along the load direction resulting in the semi-oval shape of the melt-pools. Fibrous textures are observed in the EBSD pole figures and shown in Fig. 3-8 (c, d). Fig. 3-8 (e, f) show the φ2=45° section of the ODF designated by θ-fiber {100} and γ-fibre {111} planes. The (111)[1$\bar{2}$1] and (111)[$\bar{1}\bar{1}$2] peaks show the θ-fibre components, while (001)[1$\bar{1}$0] and (001)[$\bar{1}\bar{1}$0] represent γ-fibre. The peaks in the {001} family planes are not a considerable concern due to the high vulnerability of these planes to crack propagation and transgranular cleavage fracture in the BCC structure (Pineau, et al., 2016). It is also possible that the intergranular fracture

initiates from the porosities at the vicinity of the cell boundaries and deflects through the {001} planes (Béreš, et al., 2017).

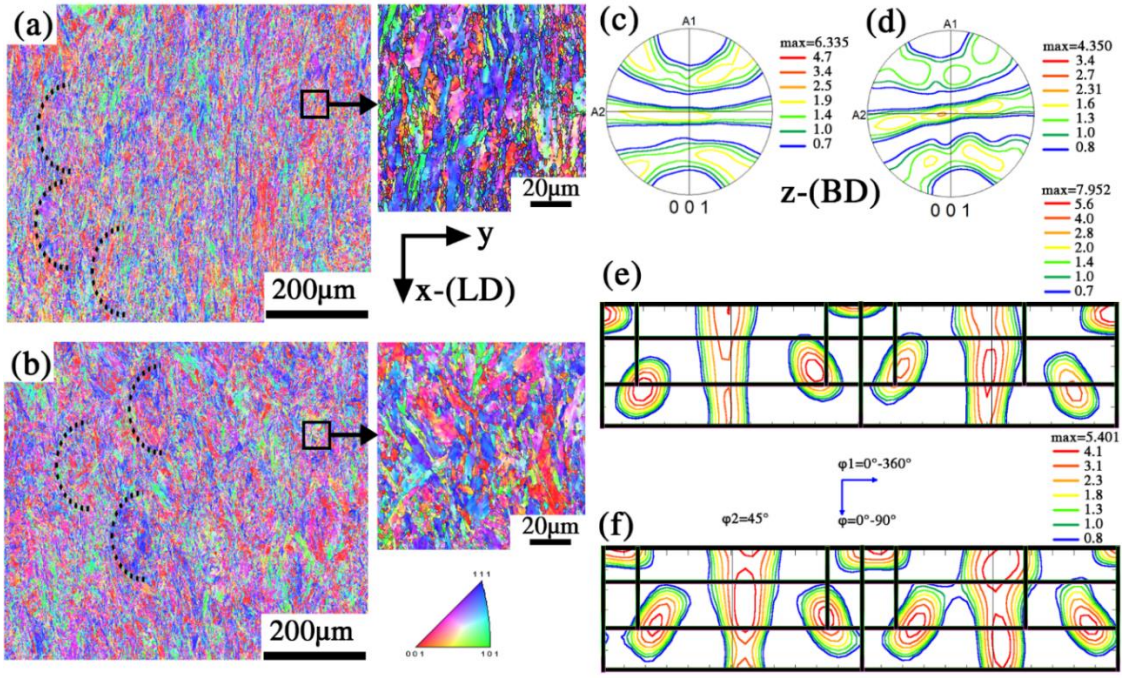

Fig. 3-8 (a, b): IPF for LPBF-40-C, LPBF-50-C, (c, d): Pole figures for LPBF-40-C and LPBD-50-C, (e, f): ODF for LPBF-40-C, LPBF-50-C.

Fig. 3-9 displays the grain boundaries types and the area fraction over different sectioned zones in the LPBF-40 and LPBF-50 samples. High angle grain boundaries (HAGBs) categorized as the 2D structural defect with 15-64.7° misorientation angles are pointed out in black colour, while low angle grain boundaries (LAGBs) with misorientation angles ranged within 3-15° are shown in light green colour. In both cases of the powder layer thickness, the plastic deformation results in more number and higher length of the LAGBs. As Sangid et al. showed (Sangid, et al., 2011), the GBs with lower interfacial energy, such as the values expected in LAGBs, offer a more substantial barrier against slip transmission. Regarding this fact, the as-built structure of the LPBF-40-A sample with a lower fraction of LAGBs compared to the LPBF-50-A zone is supposed to be more

resistant against the dislocations slip during the uniaxial tensile testing. This trend is also observed in the deformed LPBF-B zones. Therefore, the LPBF-40 sample reveals more strain hardenability, which brings it a higher UTS value than the LPBF-50 one. The above observation is in good agreement with the results in Fig. 3-3. The LAGBs are suitable sites to accumulate and tangle the dislocations. Subsequently, an increase in the LAGBs in zone C is a shred of evidence showing the high density of dislocations in Fig. 3-9 (e, f) (Masoumi, et al., 2019).

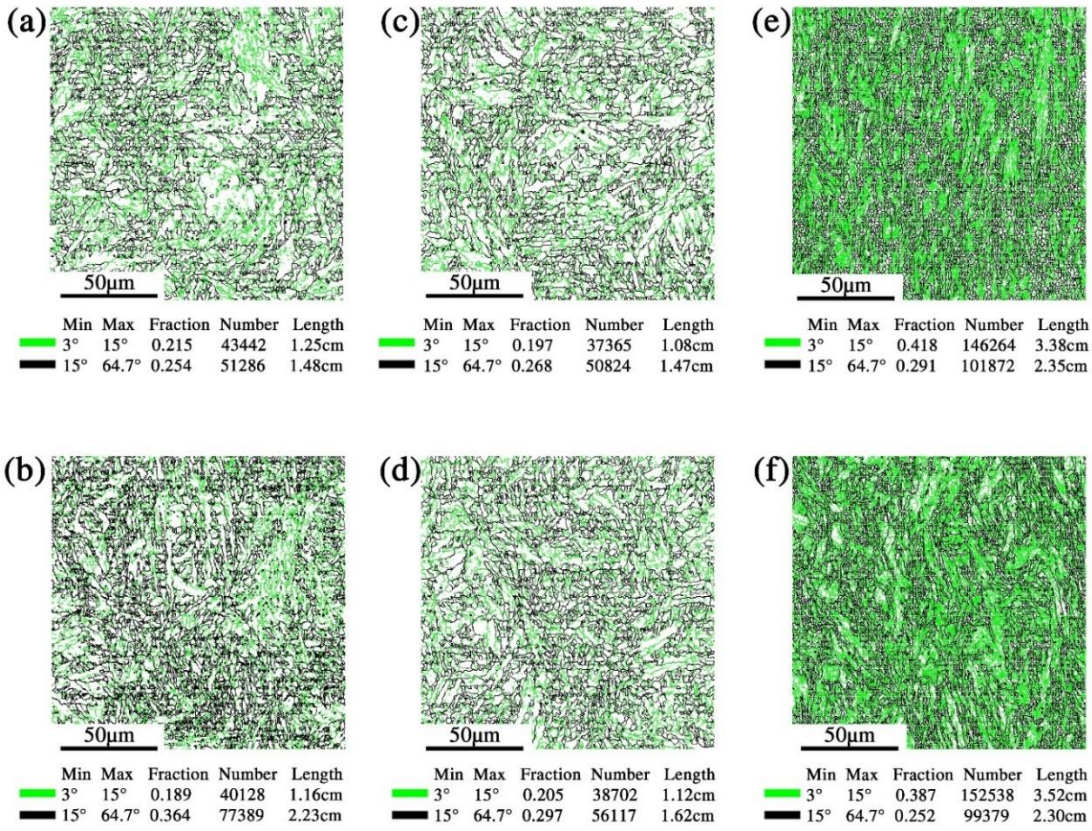

Fig. 3-9 EBSD grain boundary maps in three different zones shown for (a, b): LPBF-40-A, LPBF-50-A, (c, d): LPBF-40-B, LPBF-50-B, and (e, f): LPBF-40-C, LPBF-50-C.

Fig. 3-10 shows Kernel Average Misorientation (KAM) technique in zones A-C. The KAM results are used to measure the local grain misorientation, where the more dislocation density leads to higher KAM values. It can also be employed to investigate the local lattice

distortion, localized deformation, and stored strain energy in grains (Saraf, 2011) (Schwartz, et al., 2009). The LPBF-40 and LPBF-50 samples in zones A and B present a semi-homogenous distribution of KAM majorly ranged at intermediate intensities (Min:1-Max:2). The LPBF-50-(A to C) samples show a localized distribution of KAM at higher intensities compared to the LPBF-40-(A to C). In the undeformed cases (zone A), the difference in KAM intensity can be hypothesized due to a difference in residual stresses stored during 40 µm- and 50 µm-thick powder layers depositions. Higher KAM values (Min:4-Max:5) in the LPBF-50-A imply that the stored energy during 50 µm-thick layers deposition is higher than the 40 µm case numerous LAGBs compromise it. Since the more residual stresses lead to more dislocations nucleation, and consequently, more stored internal energy, it can be hypothesized that the LPBF-50 undeformed structure contains a higher volume of residual stresses compared to the LPBF-40 one. It might be another reason behind the lower strength and ductility of the LPBF-50 samples. In zone C, the KAM intensity is higher, ranged within Min:3-Max:4. A higher fraction of intensified KAM values is again observable in the LPBF-50 sample compared to the LPBF-40 case.

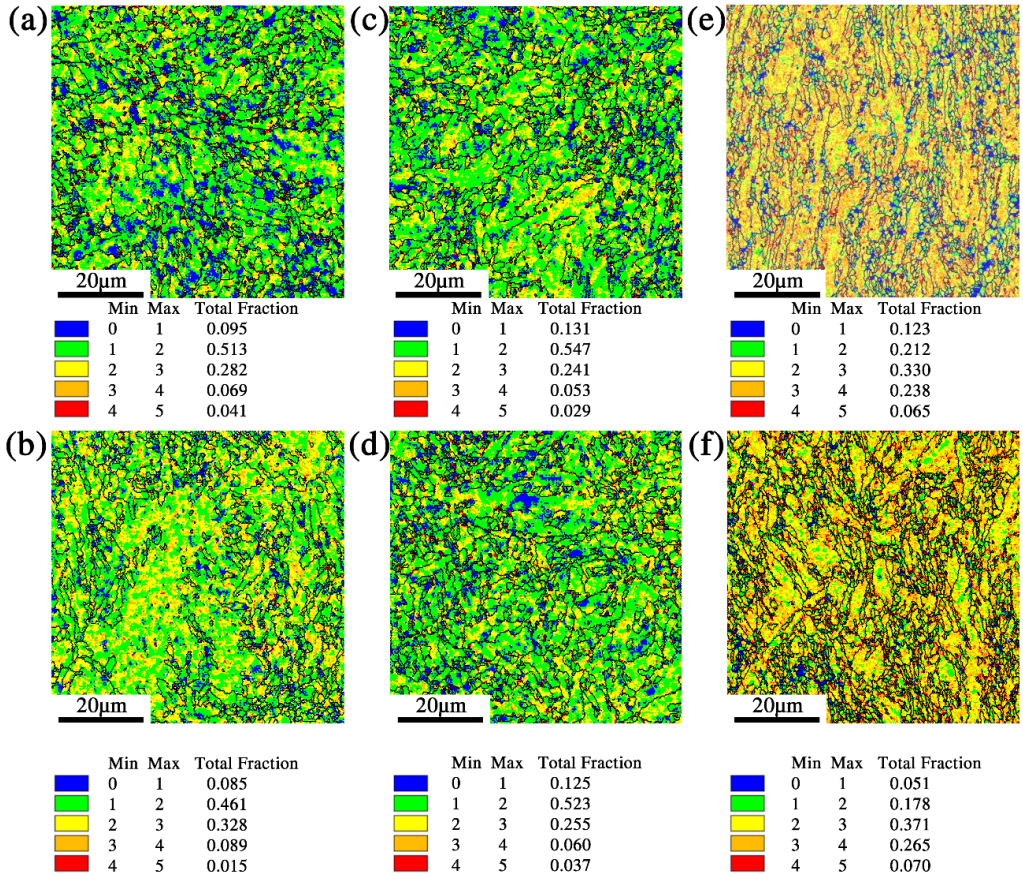

Fig. 3-10 EBSD KAM in three different zones shown for (a, b): LPBF-40-A, LPBF-50-A, (c, d): LPBF-40-B, LPBF-50-B, and (e, f): LPBF-40-C, LPBF-50-C.

In Fig. 3-11, the grain size distribution in each zone is presented for both LPBF-40 and LPBF-50 samples. As seen, the difference in powder layer thickness does not affect the grain size of the AM product. Zones A and B present similar trends in grain size variation, where the size of almost 90 % of grains is below 10 μm. However, in the sample collected from the vicinity of the fracture area (zone c), the majority of grains (90 %) is ranged below 6 μm in size. More specifically, around 50 % of grains in the severely deformed zone C are smaller than 2 μm, while only 25-30 % of the grains in zone A and B are below 3 μm. The average grain size is also measured and presented in Table 3.2.

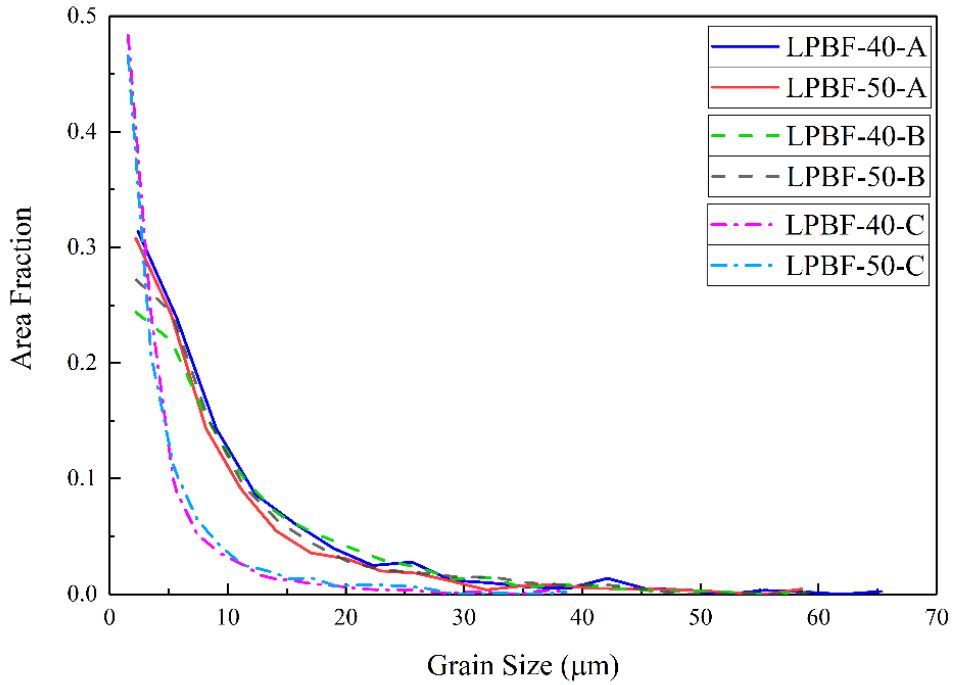

Fig. 3-11 Grain size distribution in different zones of the LPBF-40 and LPBF-50 samples.

Table 3.2 The average grain size for each variation of specimens

Sample	LPBF-40A	LPBF-50A	LPBF-40B	LPBF-50B	LPBF-40C	LPBF-50C
Average Grain size	10.0	9.0	10.5	10.0	4.5	5.0

Dimensions are in (μm), and the associated error was measured to be ± 0.5 μm.

The distribution of the misorientation angle in different zones is shown in Fig. 3-12. Fluctuation in data within 30°-60° range is higher in the undeformed samples (collected from zone A). In all samples except the LPBF-40-C, an increase in the fraction of misoriented grain is marked close to 60°.

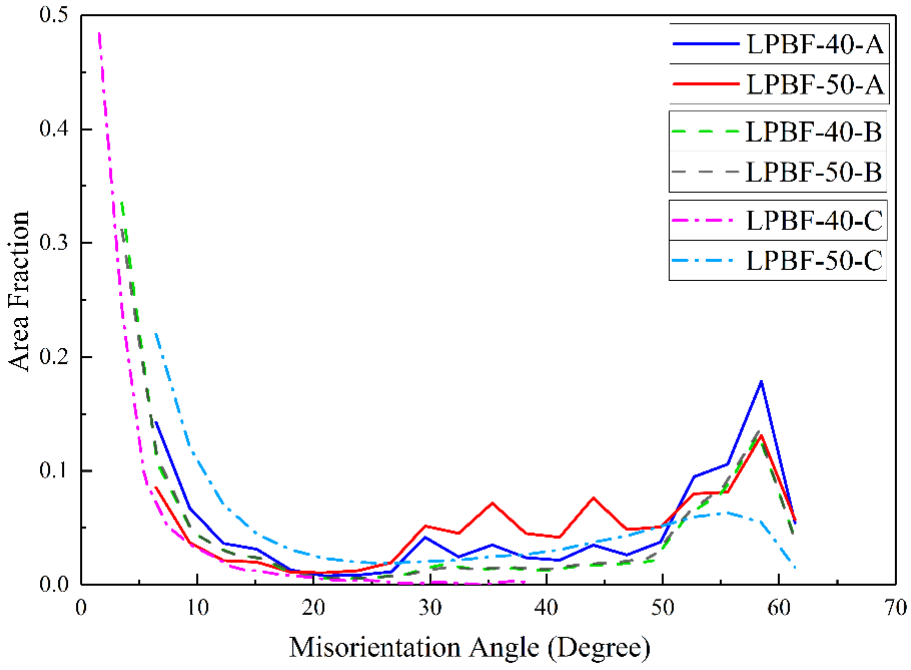

Fig. 3-12 Misorientation angle distribution in different zones of the LPBF-40 and LPBF-50 samples.

The STEM-BF image and corresponding elemental distribution maps of the LPBF-40-C and LPBF-50-C samples are shown in Fig. 3-13 and Fig. 3-14, respectively. According to distribution maps of Ti, N, Al, and O, the TiN and Al_2O_3 are determined to be nanoparticles filling the pores that were made during the manufacturing process (Shamsdini, et al., 2020). During the tensile deformation, those round Al_2O_3/TiN core/shell inclusions become elongated (Shamsdini, et al., 2020), and subsequently, debonding occurs at their interfaces. Since both inclusions have non-metallic (covalent) bonding through their structure and their surface wettability during the solidification (before any further deformation processes) is low, the interface is very prone to be debonded during stress and strain localization. Consequently, a narrow flaw between these inclusions can be enlarged and propagated during the tensile testing. As seen in Fig. 3-14 (Ti and O subfigures), it can be seen that the O element is accumulated in peripheral regions of the

crack, while the Ti element keeps its form as an elongated phase at the centre of the crack. By considering the other elemental maps (like Ni, Co, Fe), it can be concluded that the initial site for this debonding is the Al_2O_3/TiN interface; however, tensile strain leads to flaw expansion and propagation as a form of internal crack. Dislocations' pile up behind the crack and adjacent to its tip in the STEM-BF subfigure also confirms stress accumulation causing further propagation of this defect. In terms of cracking susceptibility, the grains with growth direction normal to the {100} plane are more vulnerable to crack nucleation and propagation, which is in agreement with the ODF maps in Fig. 3-8, (Figueiredo, et al., 2019) (Masoumi, et al., 2019). As a result, the TiN inclusions are nucleation sites of cracks, and subsequently, the fracture is accelerated (Viswanathan, et al., 2005).

Another feature depicted in Fig. 3-13 is the cellular structure. A trace of microsegregation in the Ti and Mo distribution maps is observable in a hexagonal shape. These elements, due to low distribution coefficient (k_0) and high diffusion coefficient (D_L) in liquid Fe, are more prone to be rejected to solid/liquid interface during solidification than those with high k_0 and low D_L, e.g. Ni and Mn (Zhang, et al., 2006) (Hunziker, 2001). Despite Ti alloying element that tends to segregate into cell boundaries (Shamsdini, et al., 2020), Ni, Co, and Mo atoms are more prone to be interstitially trapped into the lattice, also known as solute trapping or banding effect (Dmitrieva, et al., 2011). Fast solid/liquid interface velocity and high cooling rate during the LPBF technique intensify the reluctance of solute segregation during solidification in which most of the solute atoms tend to be trapped into the matrix (Ghoncheh, et al., 2020). The Ni, Co, and Mo atoms can be thermodynamically solid solutionized into the matrix at low cooling rates. However, due

to the fast solidification during the AM process, they will be dispersed over the entire microstructure showing trapping phenomenon. Furthermore, Ti shows intercellular segregation due to its low distribution coefficient and high diffusion coefficient (Dehgahi, et al., 2020).

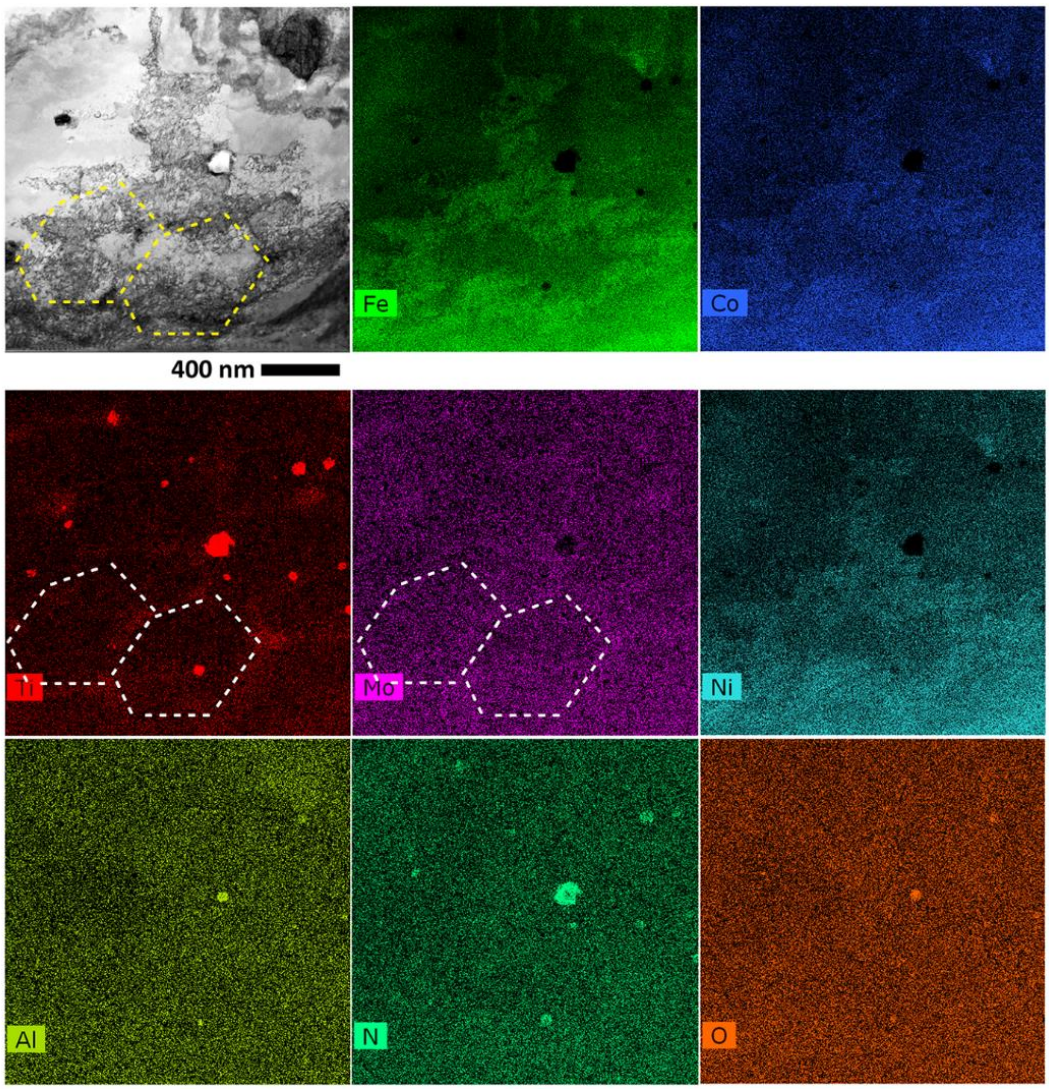

Fig. 3-13 STEM-BF image and corresponding elemental distribution maps in the LPBF-40-C sample.

Each alloying element has a different segregation rate depending on the concentration of the element in solid ($C_{s,i}$) and liquid ($C_{l,i}$) phases known as the distribution coefficient

defined in equation 1. A solid/liquid interface velocity (R) is considered in the non-equilibrium case leading to equation 2. (Dehgahi, et al., 2020)

$$k_{0,i} = {C_{S,i}}/{C_{L,i}} \quad (1)$$

$$k_{R,i} = {\left[k_{0,i} + \left(a_0 R/D_{L,i}\right)\right]}/{\left[1 + \left(a_0 R/D_{L,i}\right)\right]} \quad (2)$$

where a_0 is the interatomic distance constant and $D_{L,i}$ is diffusivity of element i in the interface. The distribution coefficients for Ni, Co, Mo and Ti are reported to be 0.81-0.95, 0.91-0.95, 0.57-0.61 and 0.30-0.32 respectively (MORITA, et al., 1988).

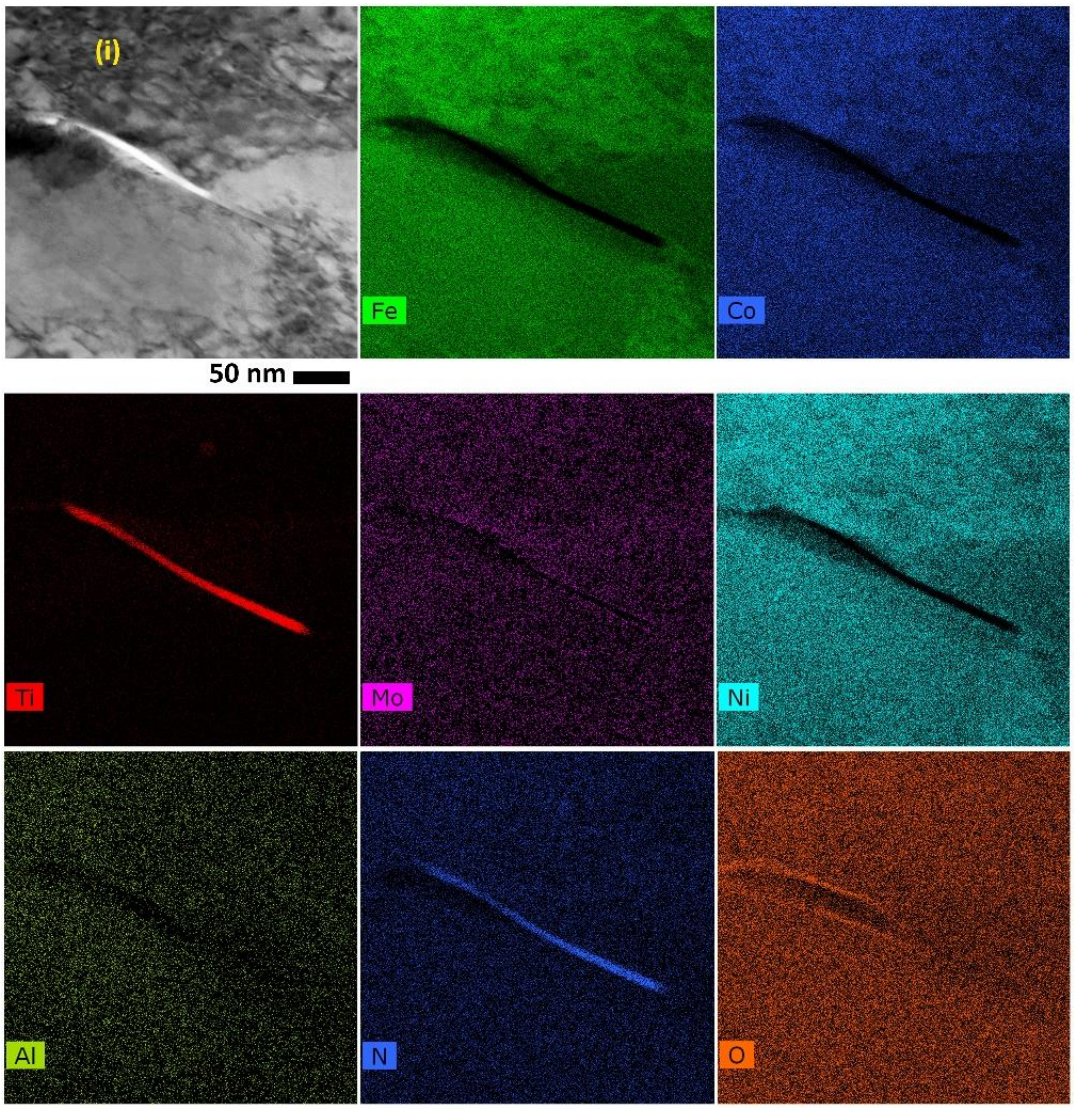

Fig. 3-14 STEM-BF image and corresponding elemental distribution maps in the LPBF-50-C sample (i: dislocations).

3.4 Discussion

3.4.1 Phase transformation

Martensitic transformation of the metastable γ phase needs a driving force to overcome the Gibbs energy barrier, also known as the saddle point in $\Delta G_{\gamma\rightarrow\acute{\alpha}}$ diagram. In 18Ni-300 maraging steel, except the ά phase formed via γ→ά athermal transformation, the rest of martensite is formed from the transformation of the metastable retained γ, where the driving force at room temperature is provided by strain induction (Tomimura, et al., 1991) (Spencer, et al., 2004). Since the X-ray has a high interaction volume in the XRD analysis, the phase fraction results present better statistics. As a result, the phase fraction studies are conducted using the XRD technique and results from Fig. 3-6 shows the elimination of the γ phase after uniaxial tensile deformation. As shown in Fig. 3-13, the cell boundaries are indicated as hexagonal cells in the Ti distribution map, where the corresponding zones in the STEM-BF contain a higher density of dislocations generated and piled due to the plastic deformation.

Retained austenite tends to remain along the cell boundaries due to the high concentration of austenite stabilizer alloying elements in these regions. Jagle et al. (Jägle, et al., 2017) and Liu et al. (Liu, et al., 2001) showed that the ultra-low carbon steels show less hardenability in regions containing high contents of Ti, Mo, and Ni, which means that Ti in these steels can also act as γ stabilizer. A higher density of dislocations in the retained austenite can be due to the higher ability of strain hardening in γ rather than ά, which brings further nucleation of dislocations. A higher density of LAGBs in Fig. 3-9 (zone C) has

resulted from the dislocation movements, also observed by Liu et al. (Liu, et al., 2019). Fig. 3-10 shows a higher mean value of KAM angles in the deformed samples, as another indication of the dislocations pile-up. In this case, increasing the dislocations density can occur in either the cell boundaries or during strain-induced martensitic transformation (Zhang, et al., 2020). The graph of the misorientation angle in Fig. 3-12 shows peaks close to 60°. These peaks indicate twin misorientation in the γ phase (Zhang, et al., 2020), and the drop after deformation is attributed to phase transformation during plastic deformation. Since twinning occurs in the γ phase at the beginning of deformation, the possibility of mechanical twinning is reduced, as γ→ά further takes place (Avner, 1974).

3.4.2 Plastic deformation

The ά phase has higher flow stress than the γ phase. Under tensile loading, the γ ductile phase embedded into the martensitic matrix is the first one experiencing the plastic deformation (Spencer, et al., 2004). Moreover, we know that in the austenite phase, the dislocation density increases with strain (Kundu, et al., 2020). In the BCC ά phase with high Peierls stress, the slip planes are less activated compared to the FCC phase containing lower Peierls stress. In maraging steels with intrinsically low stacking fault energy (SFE) due to the presence of various solute atoms of alloying elements within the lattice (Suzuki effect (Suzuki, 1962)), high Peierls stress of ά phase remarkably reduces the strain hardening rate of ά compared to the γ phase. During plastic deformation, the active slip systems of the FCC γ phase (<110>{111}) and BCC ά phase (<111>{110}{112}{123}) can be observed as shear deformation component in texture analyses. A weak γ-fibre as a shear deformation component in the FCC structure is observed in zones A and B (Fig. 3-5 and Fig. 3-7). In the severely deformed area in zone C, θ-fibre and γ-fibre components

show higher intensities, which is showing the transformation of the austenite phase into martensite through the deformation.

In Fig. 3-10, higher KAM intensity in zone C represents higher localized strain, which occurs along the grain boundaries. The γ→ά transformation and the grain refining happen concurrently in zone C, which is confirmed in Fig. 3-11. Zone B, on the other hand, shows no significant change in the grain size compared to initial grains in the as-built structure (zone A). It is concluded that zone B is not subjected to large deformation, and consequently, the strain-induced phase transformation. It is noteworthy that the deformation occurs under the quasi-static state with no external heat source. As a result, the martensitic transformation is not followed by an irreversible ά→$\gamma_{Reverted}$ transformation. Therefore, the XRD pattern of the severely deformed sample does not show the γ phase.

The LAGBs distribution and misorientation correlation through plastic deformation are observed in Fig. 3-9 and Fig. 3-12 (Li, et al., 2019). The misorientation angle shows multiple peaks that start from 30° and reach a maximum value close to 60°. During the deformation, the graphs become gentler, but the gradual increase within 30°-60° is still apparent. These graphs show the softening trend similar to rolled steels (Liu, et al., 2019).

3.4.3 Strain hardening

Fig. 3-3 shows two stages of strain hardening through the total deformation. In stage I, between the yield strength (YS) and UTS, where the samples are exposed to homogeneous plastic deformation, the strain hardening values are positive; however, the trend of $d\sigma/d\varepsilon$ vs. ε is descending. The positive values resulted from an increase in the number of dislocations, the more resistance against the dislocations mobility and further deformation, while the descending behavior can be attributed to progress in strain-induced martensitic

transformation (Zhu, et al., 2019). The austenite phase in stage I is a source of mechanical twin generation (Chowdhury, et al., 2017). Twins act as obstacles against dislocations movement on the slip planes. As a result, the structure still keeps strain hardening. On the other side, since the ά phase contains a considerable number of dislocations, its under-load lattice is saturated by stored energy. An increase in the density of dislocations lowers the rate of strain hardening. Therefore, progress in γ→ά transformation brings less strain hardening due to an increase in ά volume fraction. Shear bands result in the generation of mechanical twins and stacking faults in the $\gamma_{\{111\}}$ planes, which are followed by the ά phase nucleation (Lo, et al., 2009) (Das, et al., 2008). After the peak stress in which $d\sigma/d\varepsilon = 0$, the fully martensitic structure is subjected to geometric softening caused by the necking effect. Hence, strain softening will be dominant and leads $d\sigma/d\varepsilon$ becoming negative.

In Fig. 3-10, the high-intensity KAM distribution in zone C shows that high dislocation density spreads along with the material. Besides, the austenite is first to deform, and the dislocations are formed and piled-up at the austenite phase along the cell boundaries. Since the austenite is distributed evenly all over the microstructure, local dislocation movements lead to localized strain rate increase followed by localized temperature increase (Antolovich, et al., 2014) (Nes, 1997). This process is followed by void formation and coalescence of microcracks and a reduction in the active cross-section, the so-called necking effect. It is noteworthy that the deformation occurs in a quasi-static state without an external heat source involved in the current study. Nevertheless, the dislocation motion provides the energy source to local heating, resulting in adiabatic shear band failure. The strain hardening is observed at a negative rate in this stage in Fig. 3-3.

3.5 Conclusions

A comprehensive study on deformation, strain hardening mechanisms, and strain-induced phase transformation of the AM 18Ni-300 maraging steel are conducted. The most important findings of this study can be mentioned as:

After the athermal γ→ά transformation during the LPBF process, the retained γ mostly remains along the cell boundaries, the areas enriched by the solute atoms rejected during melting/solidifying repetitive cycles. In terms of segregated atoms, Ti and Mo atoms reveal a higher tendency of rejection during solidification and accumulation in cell boundaries. It is related to the low distribution coefficient and high diffusion rate of these atoms into the liquid Fe.

Strain-induced γ→ά transformation is responsible for the variation of strain hardening rate under uniaxial tensile testing, where more strain hardening tendency of the retained γ compared to ά brings positive values of $d\sigma/d\varepsilon$ over stage I; however, progress in the martensitic transformation lowers the values down to zero at peak stress. After this point, in stage II, negative values of $d\sigma/d\varepsilon$ are assigned to geometric softening effect.

The material adjacent to the fracture area (zone C) shows a fully martensitic structure, fine grains, a high fraction of LAGBs, a severe intensity of KAM angles, and a high density of dislocations at the vicinity of cell boundaries. In this regard, the AM sample manufactured by deposition of 40 μm-thick powder layers shows a lower fraction of LAGBs, and consequently, higher resistance against the dislocations slip during plastic deformation. Higher strain hardenability and UTS value in the LPBF-40 sample are due to this difference.

3.6 References

Ahmed M. [et al.] Magnetic properties of maraging steel in relation to deformation and structural phase transformations [Journal] // Acta metallurgica et materialia. - 1994. - Vol. 42(3). - pp. 631-638.

Antolovich S. D. and Armstrong R. W. Plastic strain localization in metals: origins and consequences [Journal] // Progress in Materials Science. - 2014. - Vol. 59. - pp. 1-160.

Asgari H. [et al.] On microstructure and mechanical properties of additively manufactured AlSi10Mg_200C using recycled powder [Journal] // Materials Science and Engineering: A. - 2017. - Vol. 707. - pp. 148-158.

ASM International Handbook Committee Properties and selection: irons steels and high performance alloys [Book]. - America : ASM Handbook, Materials Information Company, 1991.

Avner S. H. Introduction to physical metallurgy [Book]. - New York : McGraw-hill, 1974.

Béreš M. [et al.] Role of lattice strain and texture in hydrogen embrittlement of 18Ni (300) maraging steel [Journal] // International Journal of Hydrogen Energy. - 2017. - Vol. 42(21). - pp. 14786-14793.

Bhardwaj T. and Shukla M. Effect of laser scanning strategies on texture, physical and mechanical properties of laser sintered maraging steel [Journal] // Materials Science and Engineering: A. - 2018. - Vol. 734. - pp. 102-109.

Chowdhury P., Canadinc D. and Sehitoglu H. On deformation behavior of Fe-Mn based structural alloys [Journal] // Materials Science and Engineering: R: Reports. - 2017. - Vol. 122. - pp. 1-28.

Cyr E. [et al.] Fracture behaviour of additively manufactured MS1-H13 hybrid hard steels [Journal] // Materials Letters. - 2018. - Vol. 212. - pp. 174-177.

Das A. [et al.] Morphologies and characteristics of deformation induced martensite during tensile deformation of 304 LN stainless steel [Journal] // Materials Science and Engineering: A. - 2008. - Vols. 486(1-2). - pp. 283-286.

Dehgahi S. [et al.] The role of titanium on the microstructure and mechanical properties of additively manufactured C300 maraging steels [Journal] // Materials & Design. - 2020. - Vol. 194. - p. 108965.

Dmitrieva O. [et al.] Chemical gradients across phase boundaries between martensite and austenite in steel studied by atom probe tomography and simulation [Journal] // Acta Materialia. - 2011. - Vol. 59(1). - pp. 364-374.

Dos Reis A. G. [et al.] High-temperature creep resistance and effects on the austenite reversion and precipitation of 18 Ni (300) maraging steel [Journal] // Materials Characterization. - 2015. - Vol. 107. - pp. 350-357.

Emadoddin E. [et al.] Influence of cold-rolling reduction on retained austenite texture in cold-rolled and intercritically annealed TRIP-assisted steel [Journal] // Journal of Applied Crystallography. - 2011. - Vol. 44(6). - pp. 1190-1197.

Figueiredo N. C. [et al.] Microstructural variations at different distance from the surface in forged 18 Ni C300 maraging steel [Journal] // Journal of Materials Research and Technology. - 2019. - Vol. 8(1). - pp. 284-291.

Fischer F. D. [et al.] A new view on transformation induced plasticity (TRIP) [Journal] // International Journal of Plasticity. - 2000. - Vols. 16(7-8). - pp. 723-748.

Galindo-Nava E. I. and Rivera-Díaz-del-Castillo P. E. J. A model for the microstructure behaviour and strength evolution in lath martensite [Journal] // Acta Materialia. - 2015. - Vol. 98. - pp. 81-93.

Ghoncheh M. H. [et al.] On the solidification characteristics, deformation, and functionally graded interfaces in additively manufactured hybrid aluminum alloys [Journal] // International Journal of Plasticity. - 2020. - Vol. 133. - p. 102840.

Hadadzadeh A. [et al.] Strengthening mechanisms in direct metal laser sintered AlSi10Mg: Comparison between virgin and recycled powders [Journal] // Additive Manufacturing. - 2018. - Vol. 23. - pp. 108-120.

Hunziker O. Theory of plane front and dendritic growth in multicomponent alloys [Journal] // Acta materialia. - 2001. - Vol. 49(20). - pp. 4191-4203.

Jägle E. A. [et al.] Comparison of maraging steel micro-and nanostructure produced conventionally and by laser additive manufacturing [Journal] // Materials. - 2017. - Vol. 10(1). - p. 8.

Jägle E. A. [et al.] Precipitation and austenite reversion behavior of a maraging steel produced by selective laser melting [Journal] // Journal of Materials Research. - 2014. - Vol. 29(17). - p. 2072.

Kučerová L., Zetková, I., Jandová A. and Bystrianský M. Microstructural characterisation and in-situ straining of additive-manufactured X3NiCoMoTi 18-9-5 maraging steel [Journal] // Materials Science and Engineering: A. - 2019. - Vol. 750. - pp. 70-80.

Kundu A., Field D. P. and Chakraborti P. C. Effect of strain and strain rate on the development of deformation heterogeneity during tensile deformation of a solution annealed 304 LN austenitic stainless steel: An EBSD study [Journal] // Materials Science and Engineering: A. - 2020. - Vol. 773. - p. 138854.

Li S. [et al.] In-situ EBSD study of deformation behaviour of 600 MPa grade dual phase steel during uniaxial tensile tests [Journal] // Materials Science and Engineering: A. - 2019. - Vol. 759. - pp. 624-632.

Liu C. [et al.] A new empirical formula for the calculation of MS temperatures in pure iron and super-low carbon alloy steels [Journal] // Journal of Materials Processing Technology. - 2001. - Vols. 113(1-3). - pp. 556-562.

Liu Z. [et al.] EBSD analysis and mechanical properties of alumina-forming austenitic steel during hot deformation and annealing [Journal] // Materials Science and Engineering:

A. - 2019. - Vol. 755. - pp. 106-115.

Lo K. H., Shek C. H. and Lai J. K. L. Recent developments in stainless steels [Journal] // Materials Science and Engineering: R: Reports. - 2009. - Vols. 65(4-6). - pp. 39-104.

Martin S. [et al.] Deformation mechanisms in austenitic TRIP/TWIP steel as a function of temperature [Journal] // Metallurgical and Materials Transactions A. - 2016. - Vol. 47(1). - pp. 49-58.

Masoumi M. [et al.] EBSD study of early fractured phenomena in a 350 grade Maraging steel elbows exposed to hydrofluoric acid [Journal] // Engineering Failure Analysis. - 2019. - Vol. 104. - pp. 379-387.

Material Data sheet EOS Maraging Steel MS1 [Journal] // EOS GmbH-Electro Optical Systems. - Munchen : [s.n.], 2017.

Mohammadi M. and Asgari H. Achieving low surface roughness AlSi10Mg_200C parts using direct metal laser sintering [Journal] // Additive Manufacturing. - 2018. - Vol. 20. - pp. 23-32.

MORITA Z. I. and TANAKA T. Thermodynamics on the equilibrium distribution coefficients of solute elements between solid and liquid phases in iron alloys [Journal] // Tetsu-to-Hagane,. - 1988. - Vol. 74(7). - pp. 1210-1218.

Morsdorf L. [et al.] 3D structural and atomic-scale analysis of lath martensite: effect of the transformation sequence [Journal] // Acta Materialia. - 2015. - Vol. 95. - pp. 366-377.

Nes E. Modelling of work hardening and stress saturation in FCC metals [Journal] // Progress in materials science. - 1997. - Vol. 41(3). - pp. 129-193.

Pineau A., Benzerga A. A. and Pardoen T. Failure of metals I: Brittle and ductile fracture [Journal] // Acta Materialia. - 2016. - Vol. 107. - pp. 424-483.

Rajkumar V. and Arivazhagan N. Role of pulsed current on metallurgical and mechanical

properties of dissimilar metal gas tungsten arc welding of maraging steel to low alloy steel [Journal] // Materials & Design. - 2014. - Vol. 63. - pp. 69-82.

Rusinek A. and Rodríguez-Martínez J. A. Thermo-viscoplastic constitutive relation for aluminium alloys, modeling of negative strain rate sensitivity and viscous drag effects [Journal] // Materials & Design. - 2009. - Vol. 30(10). - pp. 4377-4390.

Sangid M. D. [et al.] Energy of slip transmission and nucleation at grain boundaries [Journal] // Acta materialia. - 2011. - Vol. 59(1). - pp. 283-296.

Sanjari M. [et al.] Texture evolution during skew cold rolling and annealing of a non-oriented electrical steel containing 0.9 wt% silicon [Journal] // Journal of Materials Science. - 2017. - Vol. 52(6). - pp. 3281-3300.

Saraf L. Kernel average misorientation confidence index correlation from FIB sliced Ni-Fe-Cr alloy surface [Journal] // Microscopy and Microanalysis. - 2011. - Vol. 17(S2). - pp. 424-425.

Schwartz A. J. [et al.] Electron backscatter diffraction in materials science [Book]. - New York : Springer, 2009.

Sha Wei and Guo Zhanli Maraging Steels, Modeling of Microstructure, Properties and Applications [Book]. - [s.l.] : Woodhead Publishing, 2009.

Shakerin S. [et al.] Additive manufacturing of maraging steel-H13 bimetals using laser powder bed fusion technique [Journal] // Additive Manufacturing. - 2019. - Vol. 100797.

Shamsaei N. [et al.] An overview of Direct Laser Deposition for additive manufacturing; Part II: Mechanical behavior, process parameter optimization and control [Journal] // Additive Manufacturing. - 2015. - Vol. 8. - pp. 12-35.

Shamsdini S. [et al.] A trade-off between powder layer thickness and mechanical properties in additively manufactured maraging steels [Journal] // Materials Science and

Engineering: A. - 2020. - Vol. 776. - p. 139041.

Spencer K. [et al.] Strengthening via the formation of strain-induced martensite in stainless steels [Journal] // Materials Science and Engineering: A, . - 2004. - Vol. 387. - pp. 873-881.

Standard A. S. T. M. ASTM E8/E8M-15a [Journal] // ASTM Standards. - [s.l.] : Standard Test Methods for Tension Testing of Metallic Materials, 2015.

Suryawanshi J., Prashanth K. G. and Ramamurty U. Tensile, fracture, and fatigue crack growth properties of a 3D printed maraging steel through selective laser melting [Journal] // Journal of Alloys and Compounds. - 2017. - Vol. 725. - pp. 355-364.

Suzuki H. Segregation of solute atoms to stacking faults [Journal] // Journal of the Physical Society of Japan. - 1962. - Vol. 17(2). - pp. 322-325.

Tan C. [et al.] Microstructural evolution, nanoprecipitation behavior and mechanical properties of selective laser melted high-performance grade 300 maraging steel [Journal] // Materials & Design,. - 2017. - Vol. 134. - pp. 23-34.

Tomimura K., Takaki S. and Tokunaga Y. Reversion Mechanism from Deformation Induced Martensite to Austenite in Metastable Austenitic Stainless Steels [Journal] // isij international. - 1991. - Vol. 31(12). - pp. 1431-1437.

Viswanathan U. K., Dey G. K. and Sethumadhavan V. Effects of austenite reversion during overageing on the mechanical properties of 18 Ni (350) maraging steel [Journal] // Materials Science and Engineering: A. - 2005. - Vols. 398(1-2). - pp. 367-372.

Wang M. M. [et al.] Smaller is less stable: size effects on twinning vs. transformation of reverted austenite in TRIP-maraging steels [Journal] // Acta Materialia. - 2014. - Vol. 79. - pp. 268-281.

Xu X. [et al.] Microstructural evolution and mechanical properties of maraging steel produced by wire+ arc additive manufacture process [Journal] // Materials

Characterization. - 2018. - Vol. 143. - pp. 152-162.

Yuan L. [et al.] Nanoscale austenite reversion through partitioning, segregation and kinetic freezing: Example of a ductile 2 GPa Fe–Cr–C steel [Journal] // Acta Materialia. - 2012. - Vols. 60(6-7). - pp. 2790-2804.

Zhang M. [et al.] Ex-situ EBSD analysis of hot deformation behavior and microstructural evolution of Mg–1Al–6Y alloy via uniaxial compression [Journal] // Materials Science and Engineering: A. - 2020. - Vol. 775. - p. 138978.

Zhang R. [et al.] Phase-field simulation of solidification in multicomponent alloys coupled with thermodynamic and diffusion mobility databases [Journal] // Acta materialia. - 2006. - Vol. 54(8). - pp. 2235-2239.

Zhu Q. [et al.] Effect of the grain size on the microtensile deformation and fracture behaviors of a nickel-based superalloy via EBSD and in-situ synchrotron radiation X-ray tomography [Journal] // Materials Characterization. - 2019. - Vol. 156. - p. 109875.

Chapter 4

A relationship between the build and texture orientation in tensile loading of the additively manufactured maraging steels

Abstract

This research reveals the effect of building direction on the microstructure, mechanical properties and the deformation behaviour of additively manufactured maraging steels. 18Ni-300 maraging steel samples were manufactured throughout the laser powder bed fusion (LPBF) process in horizontal and vertical directions. Uniaxial tensile tests were then conducted for as-built and heat-treated specimens to study the mechanical properties before and after the heat treatment process. The horizontal samples showed higher strength and ductility than the vertical ones, while the heat-treatment procedure reduced the building direction effect on the mechanical strength. Ductility was slightly different amongst the four sets of specimens. The heat-treatment increased the mechanical strength significantly at the expense of decreasing the ductility. Fractography through scanning electron microscopy showed that the aged fracture surfaces contain cleavage along with dimples. Transmission electron microscopy revealed the austenite phase enclosed by the martensite laths and segregated alloying elements and precipitations, resulting in a hierarchical microstructure. Further studies on the deformation behaviour in the four cases of as-built/aged, horizontal/vertical combinations were conducted. X-ray diffraction technique was adopted to study the phase changes through the deformation process. The as-built specimens showed a fully transformed austenite phase, while the aged samples reduced the austenite fraction to half at the fracture. Finally, the EBSD technique was conducted to show the microstructure evolution through the manufacturing process. The material

showed an elongated grain structure towards the building direction. Heat-treatment did not eliminate the texture along the building direction, while the deformation process led to a texture evolution from <100> and <111> into <110> directions.

Keywords: Maraging steel; microstructure; laser-powder bed fusion; recoater blade; deformation.

4.1 Introduction

Maraging steels have been extensively used in different industries due to their mechanical properties (Sha, et al., 2009). However, the knowledge around the additively manufactured maraging steels is not sufficient for the industrial world yet. Along with the development of the additive manufacturing process, research on the mechanical properties and microstructure of such material is shedding light on its ability to produce parts with similar properties compared to the older manufacturing methods (Tan, et al., 2018) (Mooney, et al., 2019) (Meneghetti, et al., 2017) (Fortunato, et al., 2018) (Mutua, et al., 2018). Tan et al. (Tan, et al., 2018) studied the as-built and aged maraging steel samples concluding that the heat treatment reduced the residual stresses. A variation of heat treatment and build orientation was investigated by Mooney et al. (Mooney, et al., 2019), resulting in a mechanical properties window for the studied parameters. The fatigue properties of maraging steel were studied by Meneghetti et al. (Meneghetti, et al., 2017), and the vertical samples showed higher fatigue strength. However, in a recent study conducted by Croccolo et al. (Croccolo, et al., 2019), the building orientation showed no effect on the fatigue response. Fortunato et al. (Fortunato, et al., 2018) studied the optimal process parameters by applying the milling operation on maraging steel. Besides, a processing window showing the mechanical properties based on the process parameters

was presented by Mutua et al. (Mutua, et al., 2018). Although the material might be showing some similar properties at the end, it is following a different path during its manufacturing process. The multi-layer powder deposition, in conjunction with the cyclic heating loads applied to the previously solidified layers, results in a whole different microstructure (Becker, et al., 2016) (Jägle, et al., 2014) (Cyr, et al., 2018).

The additively manufactured microstructure is typically anisotropic, with a directional grain texture (Sun, et al., 2018) (Kuo, et al., 2017). Thus, the mechanical properties are different in horizontal and vertical directions. Due to the rapid cooling rate during solidification, grains tend to elongate perpendicular to the melt-pool boundaries (Dovgyy, et al., 2018). A hierarchical microstructure is predictable considering melt-pool structure and grain orientation to apply high vs. low scale anisotropy, respectively. The hierarchical structure in stainless steel manufactured through the additive process was shown by Wang et al. (Wang, et al., 2018) to increase the strength and ductility without sacrificing one in favour of the other. In another study, additively manufactured AlSi10Mg was studied, and the role of the hierarchical microstructure on the dynamic behaviour was investigated (Hadadzadeh, et al., 2019).

Recent studies on maraging steel showed the anisotropic behaviour by studying various building directions (Mooney, et al., 2019) and (Vishwakarma, et al., 2020). A significant range of anisotropy was reported amongst various suppliers, and the heat-treatment showed to be able to reduce the anisotropic behaviour (Mooney, et al., 2019). In a study by Vishwakarma et al. (Vishwakarma, et al., 2020), the tensile behaviour with higher strength and ductility in 45° build direction was reported. Various aging temperatures were studied recently on additively manufactured maraging steel resulting in an optimum heat-treatment

of 420 °C for four hours for the highest strength and ductility combination (Zhou, et al., 2020). A comprehensive review on maraging steel showed the effect of powder feedstock, processing parameters, scan strategy, and the building direction on mechanical properties of additive manufactured builds (Mooney, et al., 2020). The chemical composition was studied recently, showing an extensive effect in ductility and strength of aged maraging steel C300 (Dehgahi, et al., 2021). A wider range of steels was reviewed, and a <001> fibre texture was recognized along the building direction. The higher mechanical strength and hardness were attributed to the hierarchical structure induced through the additive process (Bajaj, et al., 2020).

On the other hand, the material passes through a microstructural evolution in terms of the available phases from powder particles to 3D-manufactured parts (Shamsdini, et al., 2020). The microstructural phases evolve due to the heat-treatment process (Guo, et al., 2004) and the strain deformation (Xu, et al., 2019). The deformation behaviour of maraging steels has been investigated in the literature, showing transformation induced plasticity (TRIP) (Wang, et al., 2015). Besides, 18Ni-300 maraging steel contains a higher fraction of martensite phase with body centred cube (BCC) crystal structure and a lower fraction of austenite with face centred cube (FCC) crystal structure, retained from the solidification process or reverted from the heat-treatment (Suryawanshi, et al., 2017). The effect of building direction is overlooked on the deformation mechanisms and the phase transformation. Likewise, studies on the deformation and phase transformation of the heat-treated samples are missing in the literature.

Although a detailed study on the microstructural components of the martensitic steel is available in the literature (Galindo-Nava, et al., 2016), the microstructure of additively

manufactured maraging steel is needed to be looked at on various scales. In the current study, 18Ni-300 maraging steel is investigated in the additive manufacturing process. Manufactured samples are studied in both horizontal and vertical directions and for as-built and heat-treated conditions. At first, the hierarchical microstructure is characterized, and then the evolution of the microstructure due to the manufacturing process, ageing and strain deformation is investigated.

4.2 Experimental procedures

4.2.1 Manufacturing process

Gas atomized 18Ni-300 maraging steel powder was used to produce cubes and rods through the laser powder bed fusion (LPBF) technique. The chemical composition of the maraging powder used in this study is shown in Table 4.1 (Matreial Data sheet, 2017). The additive manufacturing process was implemented using an EOS M290 machine with a 400 W Yb-fiber laser and a laser spot size of 100µm. The build plate was preheated to 40 °C, and nitrogen gas was used to reduce the building chamber's oxygen content and facilitate the powder deposition. Cubic samples were produced to study the porosity and hardness of the material. Cylindrical bars were then manufactured and machined into uniaxial tensile test samples. All samples in the current study were manufactured using a stripe scanning strategy. The stripes had a 10 mm length with 67° layer rotation. The manufacturing process parameters were used to reach the minimum porosity and are presented in Table 4.2, while p shows the power, v represents the scanning speed, t and h refer to the layer thickness and hatch spacing, and E is associated with the energy density.

Table 4.1 Chemical composition of the 18Ni-300 maraging steel powder (Material Data sheet, 2017)

Element	Fe	Ni	Co	Mo	Ti	Al	Cr, Cu	C	Mn, Si	P, S
Range %	Bal.	17-19	8.5-9.5	4.5-5.20	0.6-0.80	0.05-0.15	0-0.50	0-0.03	0-0.10	0-0.01

Table 4.2 LPBF process parameters applied in the current study

Process parameter	p (W)	v (mm/s)	t (µm)	h (µm)	E (j/mm^3)
Value	285	960	40	110	67.47

4.2.2 Through the depth properties

Cubic samples were additively manufactured with one cubic centimetre dimension to study the porosity through the depth. As-built and heat-treated samples were polished from the top surface into a fine grade up to 1 µm polishing cloth. Using a Zeta-20 optical microscope (OM), over 30 images were collected for each sample and analyzed through the return mapping technique. The ImageJ software was used to implement the image processing, and the porosity level for the polished surface was measured (Schneider, et al., 2012). Another millimetre of the material was removed using a Nano 1000T Grinder, and the porosity measurement was repeated for the new surface. It was done for up to 5 mm through the depth and would represent the whole sample considering the symmetry.

Along with porosity measurement, hardness was also measured using a CRM Clark Rockwell machine with a 150 kg load applied on the diamond indenter head. The average values for a minimum of three measurements were reported along with the measured error. The as-built cube samples were designated as LPBF-AB, while the heat-treated ones as LPBF-HT. It is noteworthy that the heat-treatment process applied to all samples in the current study was heating to 490°C for 6 hours and air-cool in the oven (Material data sheet, 2017).

4.2.3 Mechanical properties

Uniaxial tensile test samples were machined out of additively manufactured round bars based on the E8/E8M ASTM standard (Standard, 2015). A minimum of three tests was applied for each set of uniaxial test specimens. Fig. 4-1 shows a tensile test coupon schematically, and the dimensions are shown in Table 4.3. A quasi-static strain rate of 9×10^{-3} s^{-1} was implemented on an Instron 1332 universal hydraulic machine equipped with a 25 mm extensometer. The samples were designated based on the building direction (BD) and heat-treatment. The LPBF-AB-H represents the 18Ni-300 maraging steel sample in the as-built condition manufactured in the horizontal direction, while the LPBF-AB-V represents the same sample printed in the vertical direction. Likewise, the LPBF-HT-H and LPBF-HT-V were the same material in the heat-treated condition and manufactured in horizontal and vertical directions. The same heat-treatment process was applied to the tensile specimens as well.

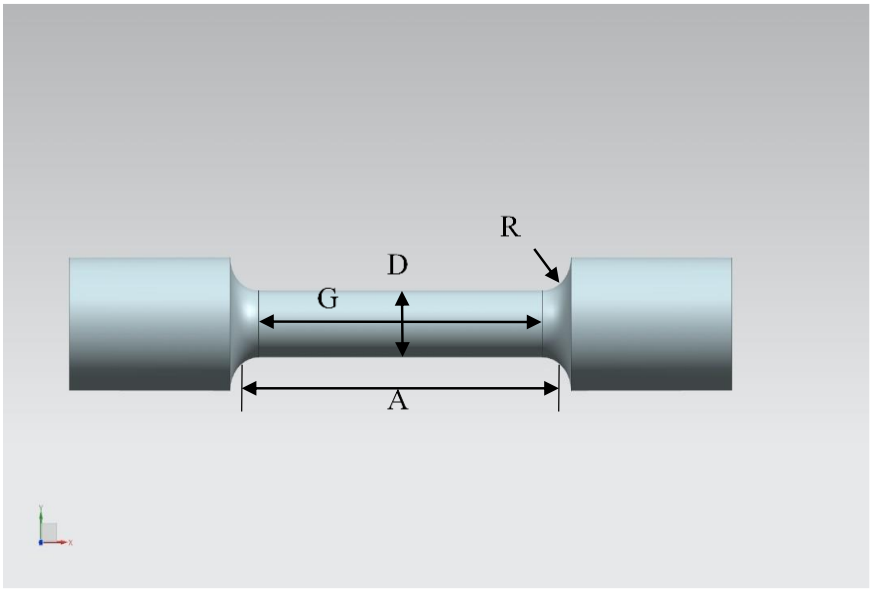

Fig. 4-1 Schematic of the uniaxial tensile test samples.

Table 4.3 Uniaxial tensile test specimens' dimensions (Standard, 2015).

	D	G	A	R
Dimensions (mm)	6.0 ± 0.1	30 ± 0.1	36	6

4.2.4 Electron microscopy and texture analyses

The sample surfaces were etched in Nital 3% for 120 seconds, and a Jeol 6400 scanning electron microscope (SEM) was used to characterize the microstructure in low and high magnifications. Fracture surfaces were then depicted with the SEM technique for low and high magnifications.

Using an FEI Tecnai Osiris device, the transmission electron microscopy (TEM) was implemented to depict high magnification images with a 200 KeV XFEG gun. A sub-nanometer electron probe was used in a super EDS detector set to provide elemental maps of TEM micrographs. TEM samples with thicknesses up to 50 nm were prepared by a lift-out technique using an FEI Helios Nanolab 650 dual-beam instrument.

The EBSD measurements were conducted using an FEI QuantaTM 450 FEG-SEM microscope over a zone with an area of 700 by 700 μm^2 placed at the x-y plane (defined in Fig. 4-11, Fig. 4-12, and Fig. 4-13). The diffraction patterns were then collected using the TSL® OIM data collection software and were post-processed using the OIM data analysis software. The crystallographic textures were calculated by harmonic series expansion with truncation at L=16. Texture fibres with <100>||BD and <111>||BD are designated as <100>-fibre and <111>-fibre, respectively.

4.2.5 X-ray diffraction technique

X-ray diffraction technique (XRD) was employed to study the deformation behaviour of the material. For this purpose, samples before and after deformation were studied using a Brucker D8 instrument equipped with a Co-Kα radiation source at 45 mA and 35 kV.

The intensity was measured over a 2θ range from 45-105°. The Rietveld technique was used to measure the weight fraction of BCC and FCC crystal structures representing martensite and austenite phases available in the material.

4.3 Results

In Fig. 4-2, the variation of hardness and porosity is shown for the as-built and aged conditions. The hardness is shown in the left y-axis and the porosity in the right y-axis. The x-axis denotes the depth from the top surface. The as-built sample results are shown in Fig. 4-2(a), with hardness varying between 35 and 36 HRC through half the sample (5 mm). The porosity changes within the range of 0.1-0.5%. There is an increase in the porosity level 2-3 mm beneath the surface, which is probably a result of the scanning strategy contour (Mohammadi, et al., 2018). Fig. 4-2(b) shows the hardness varying in the range of 53.5-54.5 HRC. Hardness at the top layers is slightly higher, which agrees with the literature (Jägle, et al., 2017). The porosity has decreased compared to the as-built case and has dropped below 0.05%, which can be considered a fully dense material. Marangoni effect results in void formation due to gas entrapment during the manufacturing process (Shakerin, et al., 2019). Throughout the heat-treatment process, those voids are prone to segregation of alloying elements, and they act as the γ-stabilizing elements as a source for reverted austenite formation (Galindo-Nava, et al., 2016), which is in agreement with the reduction of the porosity through the ageing process.

(a)

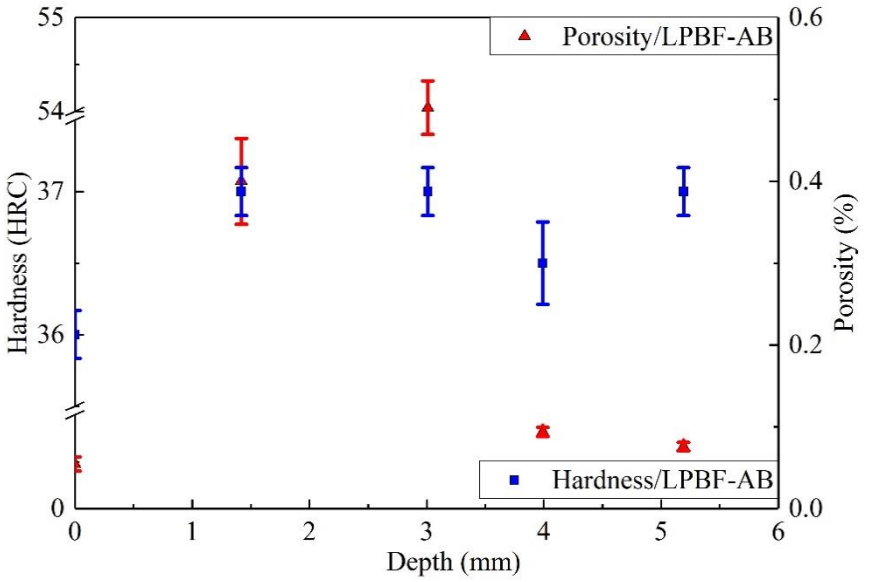

(b)

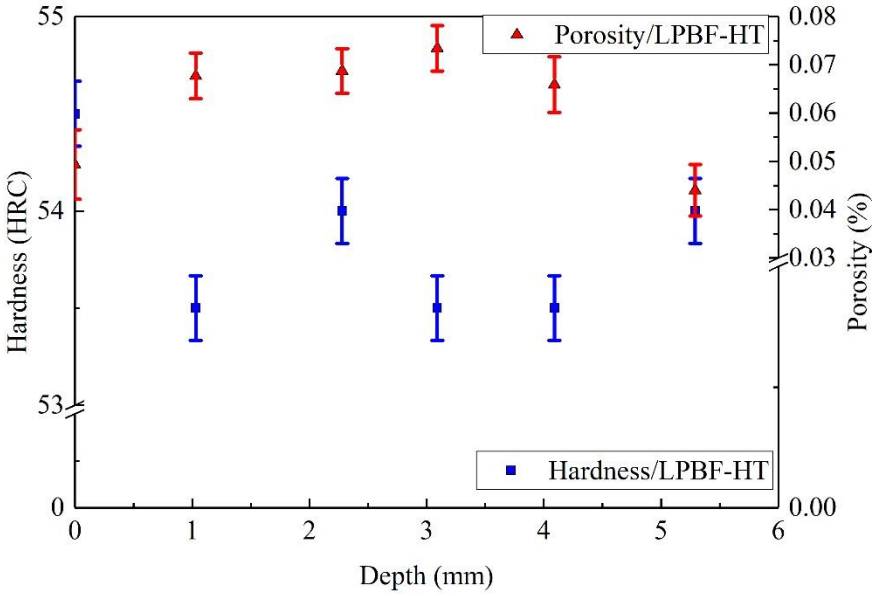

Fig. 4-2 Through the depth porosity and hardness for samples (a): As-built, (b): heat-treated.

Fig. 4-3 shows the SEM micrographs for horizontal and vertical building directions in the as-built and aged conditions. The melt-pools are observed in the Low magnification images and are showing coherent solidified structure. It is worth mentioning that the SEM results are conducted over a wide range of the surface and in multiple layers of the volume.

Thus, the images shown here are typical and represent the overall microstructure. The melt-pool dimensions showed to be similar in both horizontal and vertical builds with an average of 105 and 125 μm of depth and width, respectively. In the High magnification images, cellular structure is clearly shown in the as-built micrographs in Fig. 4-3(a, b). In both cases, the fine cellular structure reveals the effect of impulsive remelting cycles and agrees with the literature (Tan, et al., 2017). The melt-pool boundary is shown to divide the cellular structure in Fig. 4-3(b). Although the cellular structure is not as evident in the aged samples in Fig. 4-3(c, d), the austenite phase in darker shapes among the martensitic structure grains is tracked (Xu, et al., 2018).

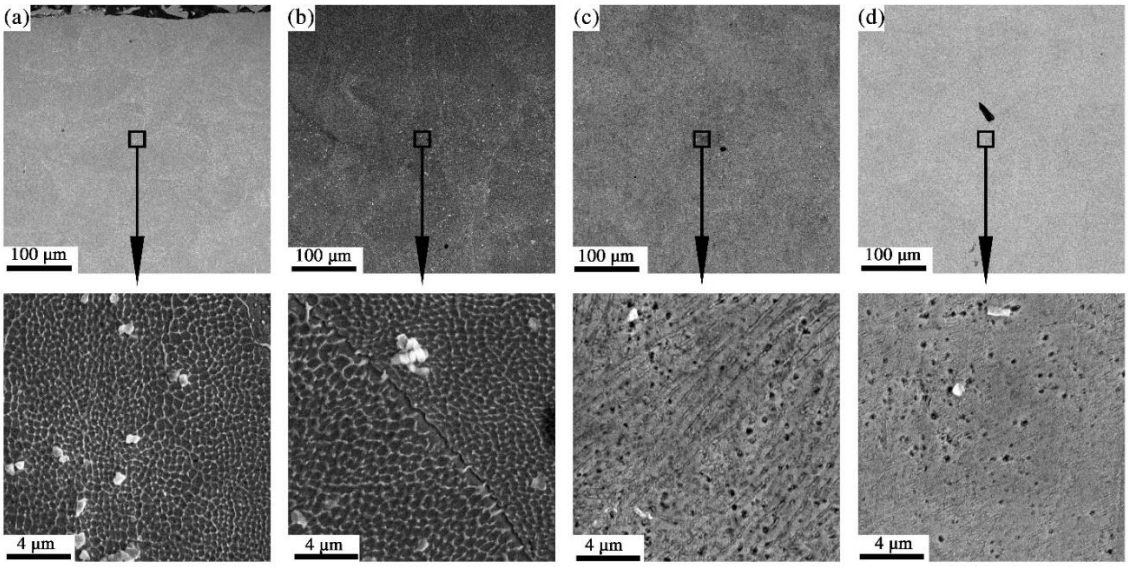

Fig. 4-3 SEM micrographs for samples (a): As-built, horizontally printed (b): As-built, Vertically printed, (c): heat-treated, horizontally printed, and (d): heat-treated, vertically printed.

Fig. 4-4 shows the stress-strain graphs for the as-built and aged conditions for both vertical and horizontal prints. The horizontal samples show an average strength and ductility of 1222 MPa and 14.6%, while the vertical ones reveal 1135 MPa strength and 11.8% ductility. The as-built samples printed in the horizontal direction show higher

strength and ductility than the vertical ones, aligned with the literature (Mooney, et al., 2019). The strength increases to 2062 and 2049 MPa, while the ductility decreases into 5.4% and 4.6% for horizontal and vertical aged samples. The aged condition's strengths are governed by the intermetallic precipitates, regardless of the build orientation (Vasudevan, et al., 1990). As a result, the aged samples show identical strength for horizontal and vertical samples. In the aged condition, the ductility is observed to be affected by the building direction, however. It is an indication of an orientational crystal structure, which is not influenced by the ageing process. In other words, the heat treatment will not result in an isotropic material that needs to be considered in the design (Sun, et al., 2018).

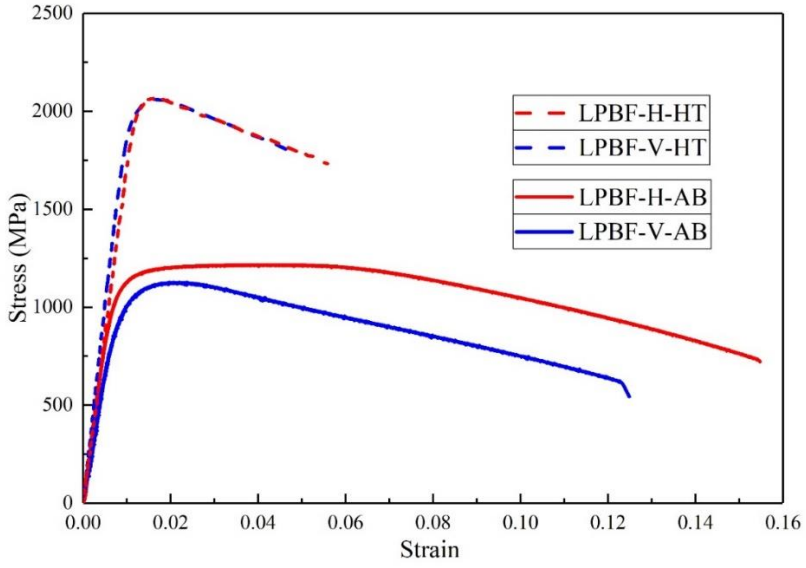

Fig. 4-4 stress-strain curves for as-built and heat-treated samples on both horizontally and vertically printed samples.

Young's modulus of elasticity, 0.2% yield strength, ultimate strength, and fracture strain are shown in Table 4.4. The first four rows present the current study's mechanical properties based on the average engineering stress-strain data and the associated errors. As observed in the data, the horizontal tests in the as-built and aged conditions show lower deviation than the vertical ones. Mechanical properties of the maraging steel are normally improved compared to the wrought material (Xu, et al., 2018). More specifically, in the as-built condition, all the parameters are higher such as mechanical strength and elasticity, or at the high range, such as ductility. In the aged condition, the mechanical strength fits the high range of the wrought material at lower ductility cost. A similar trend was observed with the additively manufactured tests in the literature (Vishwakarma, et al., 2020). As-builts samples in the current study show higher mechanical properties both in the vertical and horizontal cases. However, the solution treatment before heat-treatment results in lower ultimate strength and higher ductility compared to the results of the current study.

Table 4.4 Mechanical properties of 18Ni-300 maraging steel, (AB: As-built, HT: Heat-treated, H: horizontal, V: Vertical, ST: Solution-treated), (Becker, et al., 2016), (Vishwakarma, et al., 2020), (Kempen, et al., 2011), and (Handbook, 1990).

Maraging steel	**E (GPa)**	**S_y (MPa)**	**S_{ut} (MPa)**	**ε_f (%)**
LPBF-H-AB	181 ± 6	1084 ± 10	1222 ± 4	14.6 ± 0.7
LPBF-V-AB	176 ± 24	936 ± 22	1143 ± 15	11.8 ± 0.8
LPBF-H-HT	178 ± 4	2045 ± 15	2062 ± 13	5.4 ± 0.3
LPBF-V-HT	180 ± 21	1989 ± 40	2049 ± 24	4.6 ± 0.2
18Ni300-AB (Becker, et al., 2016)	181	815 - 1080	1100-1205	8.3 - 12
18Ni300-HT (Becker, et al., 2016)	220	1750	1850	5.1
M300-H-AB (Vishwakarma, et al., 2020)	N/A	713	1058	11.24
M300-V-AB (Vishwakarma, et al., 2020)	N/A	851	1023	9.63
M300-H-ST-HT (Vishwakarma, et al., 2020)	N/A	920	1529	10.56
M300-V-ST-HT (Vishwakarma, et al., 2020)	N/A	886	1552	10.73
Wrought-AB (Kempen, et al., 2011) (Handbook, 1990)	180	760-895	1000-1170	6-15
Wrought HT (Kempen, et al., 2011) (Handbook, 1990)	183-193	1790-2070	1830-2100	5-11

Fig. 4-5 shows the SEM fractography of the tensile test samples. Transgranular fracture is observed in both horizontal and vertical samples in the as-built condition. In Fig. 4-5(a, b), the cup and cones are displayed in low magnifications, and the dimples reveal tensile shear in higher magnifications (Dos Reis, et al., 2015). Intergranular fracture is then presented in the aged samples in Fig. 4-5(c, d) for horizontal and vertical samples. The cleavage and the micro-cracks are demonstrated, showing the aged samples' dominant fracture mechanism (Xu, et al., 2018). The heat treatment changes the fracture mechanism, while the building direction has less effect on the fracture in both as-built and aged conditions.

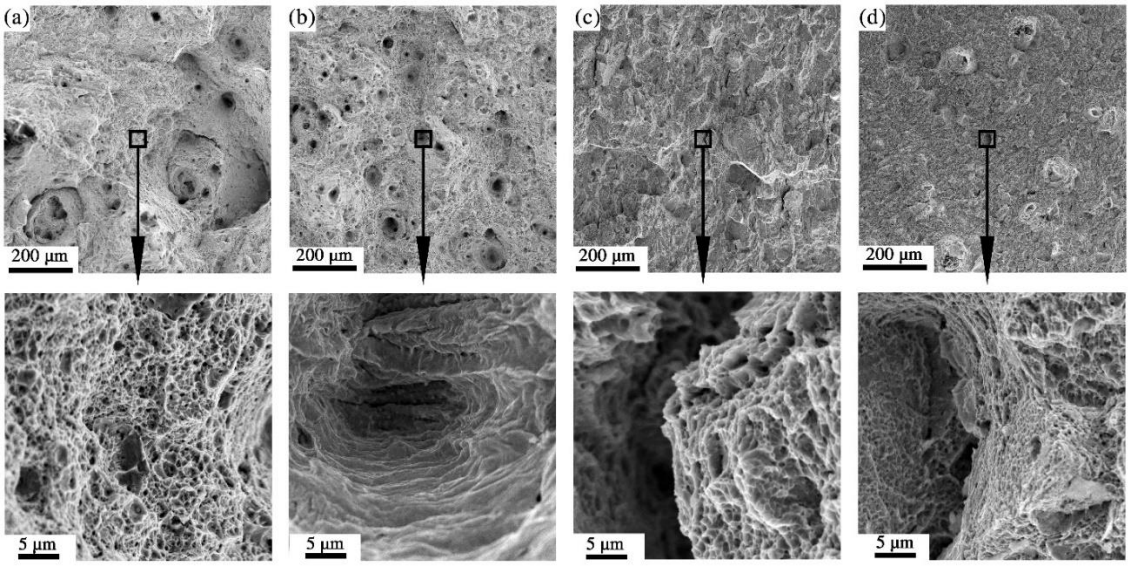

Fig. 4-5 Fracture surface for samples (a): as-built, horizontal, (b): as-built, vertical, (c): heat-treated, horizontal, (d): heat-treated, vertical.

In Fig. 4-6, STEM Bright Field micrographs are shown to identify different phases in horizontal and vertical builds for as-built and aged conditions. In Fig. 4-6(a), the austenite phase is tracked with a 150×500 nm size in the LPBF-H-AB sample. Martensite laths are depicted in parallel in Fig. 4-6(b), with a 50-150 nm width size in the LPBF-V-AB sample as the microstructure's basic units (Dos Reis, et al., 2015). A high density of dislocations dispersed among the martensitic structure is also depicted. Despite the SEM micrographs with an unclear structure in Fig. 4-3(c, d), the cellular structure is evident in the TEM micrographs of aged samples in Fig. 4-6(c, d). The hexagonal cells' size is similar to the as-built case in Fig. 4-3(a, b). In all four cases, the Ti particles are observed in a range of 50-100 nm size. The Titanium particles are spread randomly between the cellular structure and form in the martensite lath borders.

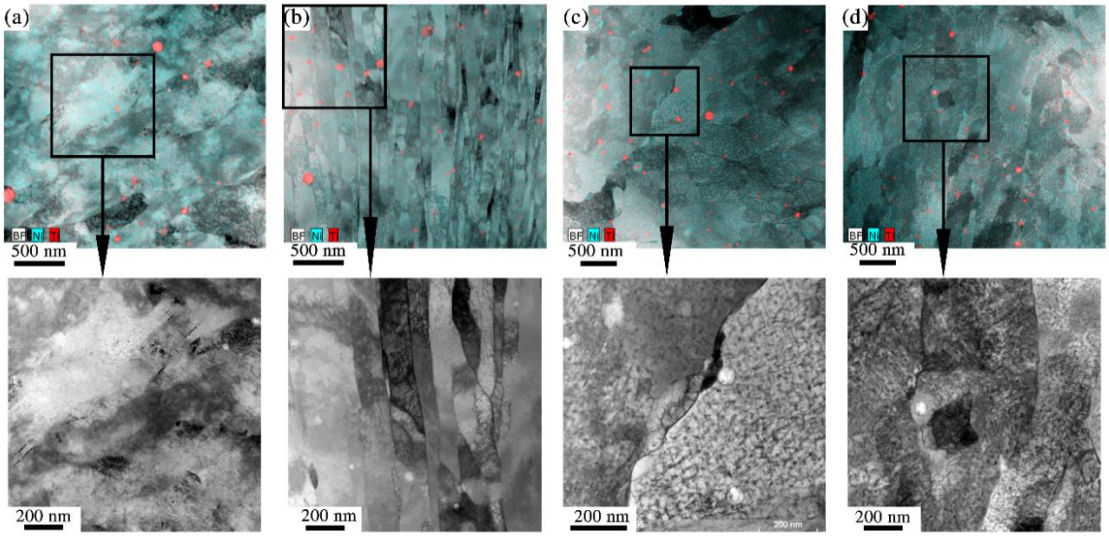

Fig. 4-6 BF-STEM micrographs for samples (a): as-built, horizontal, (b): as-built, vertical, (c): heat-treated, horizontal, (d): heat-treated, vertical.

Fig. 4-7 represents the BF-STEM micrograph and the element distribution map for the aged sample built horizontally. Particles with Aluminum core and Titanium shell are observed in the element maps with a 60 nm size. Although the nano-scale Al and Ti elements are reported previously in the as-built condition (Shamsdini, et al., 2020), the heat-treatment process seems not to affect its morphology. Precipitates of Nickel, Titanium, and Molybdenum are also depicted in this figure. The needle-shaped precipitates of Ni_3(Ti, Mo) are observed having a width of 5-10 nm and a length of 50-100 nm, while the Fe_2Mo precipitates are shown smaller in globular shapes (Dos Reis, et al., 2015).

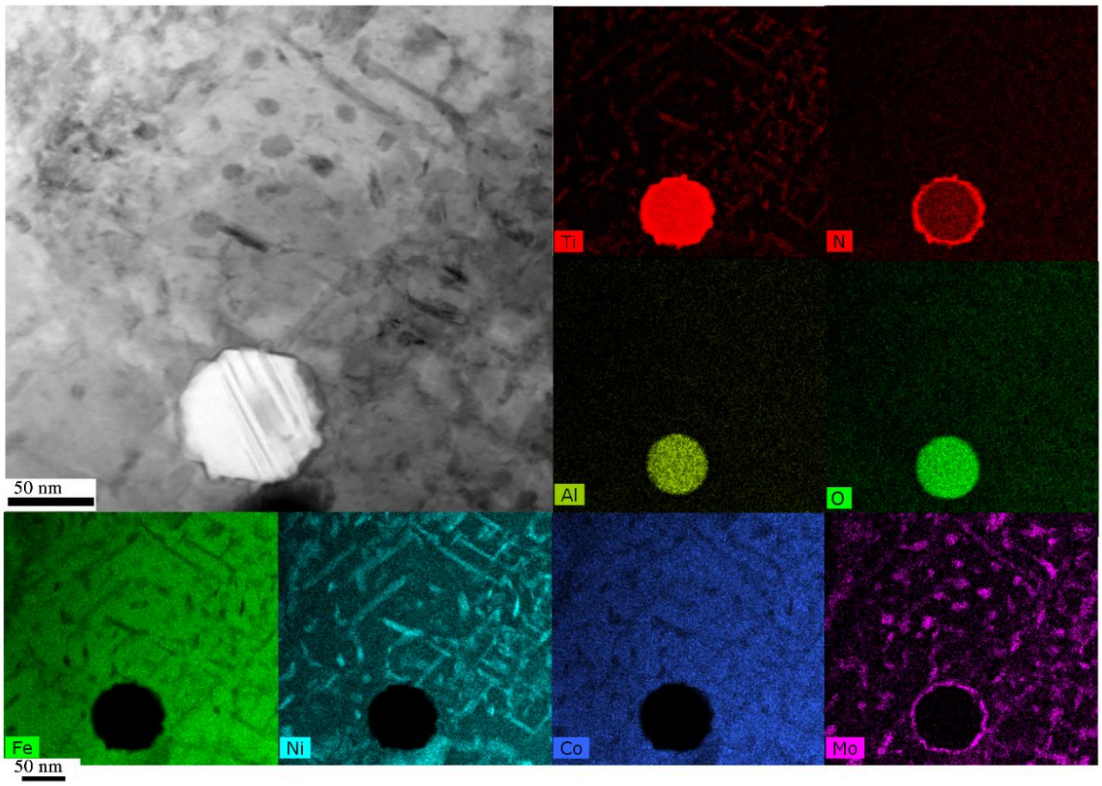

Fig. 4-7 BF-STEM micrograph, along with the element distribution map for heat-treated samples printed in the horizontal direction.

The BF-STEM, along with its element distribution map of the vertically printed sample after heat-treatment, is shown in Fig. 4-8. High dislocation density is observed on the left side of the STEM micrograph. The high dislocation area is highly rich with precipitates of Ni, Ti, and Mo elements. In the center of the graph, a noticeable nano-scale reverted austenite grain γ_{RN} is depicted. The γ_{RN} forms through the aging process at the martensite grain boundaries. It has also been reported for Fe-9%Mn maraging steel (Raabe, et al., 2013). The austenite grain is observed to have a 40-80 nm width and over 250 nm length and riched with Fe, Ni, Co, and Mo alloying elements. Finally, the Al/Ti elements discussed in Fig. 4-7 are also observed in Fig. 4-8, indicating that its distribution along the structure is regardless of the build orientation.

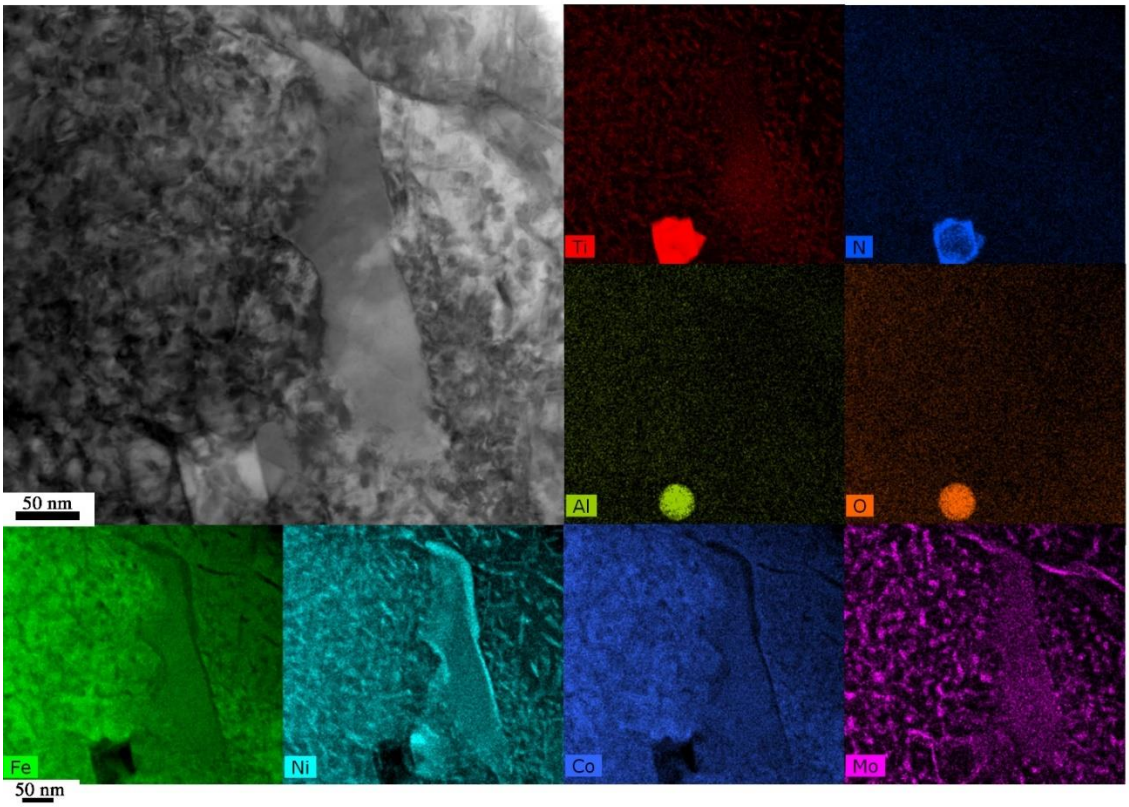

Fig. 4-8 BF-STEM micrograph, along with the element distribution map for heat-treated samples printed in the vertical direction.

Fig. 4-9 Shows the XRD intensity over 2θ range in the undeformed condition for horizontal and vertical directions in the as-built and aged condition. The austenite phase fraction is compared in Table 4.5. The first observation is that the austenite fraction is 1.5 times higher in the horizontal builds than the vertical direction. On the other hand, the heat-treatment process shows to increase the austenite phase fraction extensively. The initial percentage of the austenite grains before the ageing process seems to affect the reverted austenite fraction similar to the as-built cases (1.5 times higher in horizontal compared to vertical). Although various studies in maraging steel show different values for phase fractions, they are consistent in reposting an increase of austenite phase fraction after the heat treatment (Tan, et al., 2017) (Suryawanshi, et al., 2017) (Xu, et al., 2018).

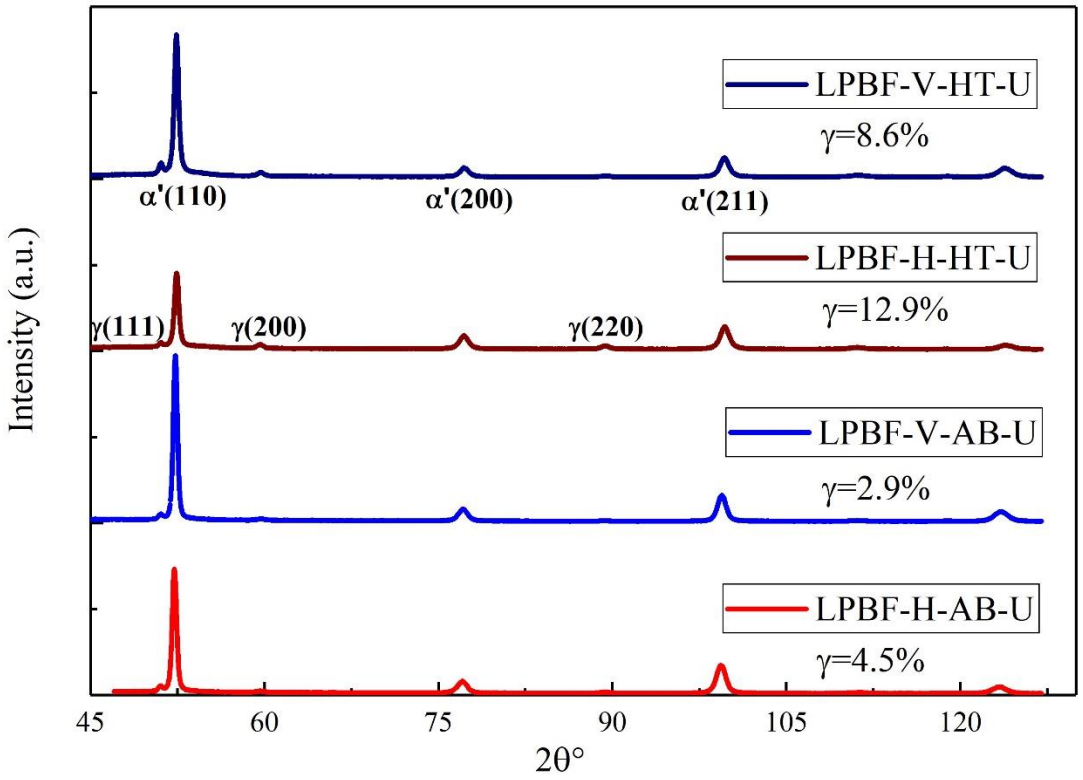

Fig. 4-9 XRD intensity over 2θ range in the undeformed condition for as-built and heat-treated samples in horizontal and vertical directions.

Fig. 4-10 shows the XRD results in the deformed case. The horizontal and vertical samples in the as-built condition show a complete transformation of austenite into martensite during the deformation. A complete austenite phase transformation has been reported for Fe-Cr-C steel near the fracture surface previously (Yuan, et al., 2012). The aged samples show an incomplete strain-induced transformation in both horizontal and vertical conditions. The aging process increases the austenite fraction and embrittlement of the microstructure, resulting in a fracture before a complete phase transformation. Still, reducing the austenite phase fraction in different directions is proportional to the initial values before the deformation.

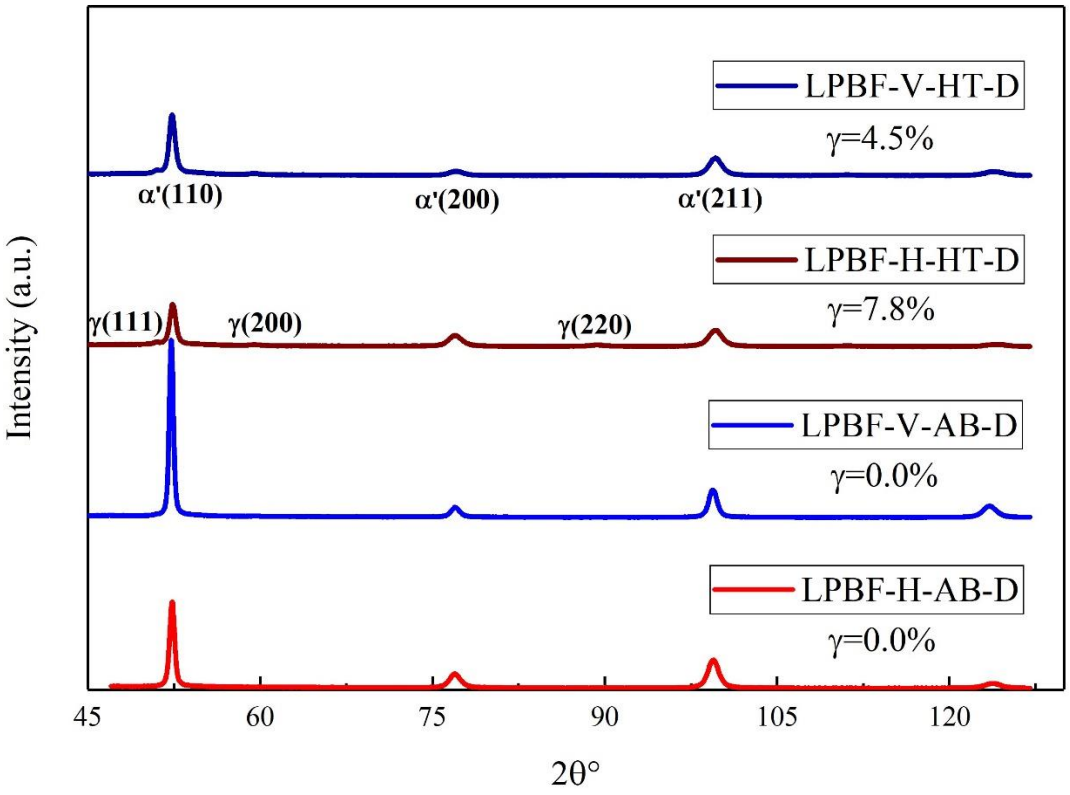

Fig. 4-10 XRD intensity over 2θ range in the deformed condition for as-built and heat-treated samples in horizontal and vertical directions.

Table 4.5 Austenite phase fraction for various samples (All data in % with ±0.2% error).

Undeformed				**Deformed**			
As-Built		Heat-Treated		As-Built		Heat-Treated	
Horizontal	Vertical	Horizontal	Vertical	Horizontal	Vertical	Horizontal	Vertical
4.5	2.9	12.9	8.6	0	0	7.8	4.5

Fig. 4-11 shows the inverse pole figure (IPF) and pole figures (PFs) for the as-built sample in the vertical prints in undeformed and deformed conditions. In this case, the build and tensile directions are aligned. It is noteworthy that the pole figures have been plotted based on the texture of the bcc phase. Since the melt-pools are directed upward towards the build-direction, it is expected that the melt-pools elongate during tensile deformation by increasing the depth and decreasing the width. Fig. 4-11(b) reveals a texture of

elongated melt-pools towards the load direction. As it can be seen from the pole figures depicted in Fig. 4-11(c), the as-built sample presents a weak texture with the maximum intensity at <100> pole and the second maximum at <111> pole. The peak observed in the (111) PF indicates a <111>-fibre texture, while the (001) PF peak reveals the <100>-fibre texture. After deformation, however, the sample represents a relatively strong texture with dominant <011>-fibre texture in which the <011> direction is preferentially aligned with the building direction (cf. Fig. 4-11(d)) and both peaks of <111>-, and <100>-fibre have disappeared.

XRD results from Fig. 4-9 and Fig. 4-10 suggest that the AM samples' major volume fraction in various builds consist of a bcc crystal structure. In such structure, the deformation occurs in <111> direction and {110} or {112} planes (according to the closed packed direction and large interplanar spacing) (Weinberger, et al., 2013). Based on Schmid's law, a uniaxial tensile test in bcc crystal structures leads to a rotation of the tensile axis towards a <111> (e.g. [111]) direction. When the tensile axis reaches the <001>-<011> symmetry line, duplex slip system will cause a rotation towards another <111> (e.g. $[11\bar{1}]$>, which will consequently result in a net rotation towards the <110> direction (Hosford, 2010). The high intensity of the <011> texture in the pole figures in Fig. 4-11(d) agrees with the rotation towards <011> direction. The EBSD results also agree with the simulation through Taylor model shown in Fig. 4-11(e). Bcc slip systems, {110}<111> and {112}<111> are examined in uniaxial tensile stress with an initial random texture and no strain hardening. A good agreement with experimental pole figures (i.e. Fig. 4-11(d)) validates a uniaxial extension strain mode of deformation.

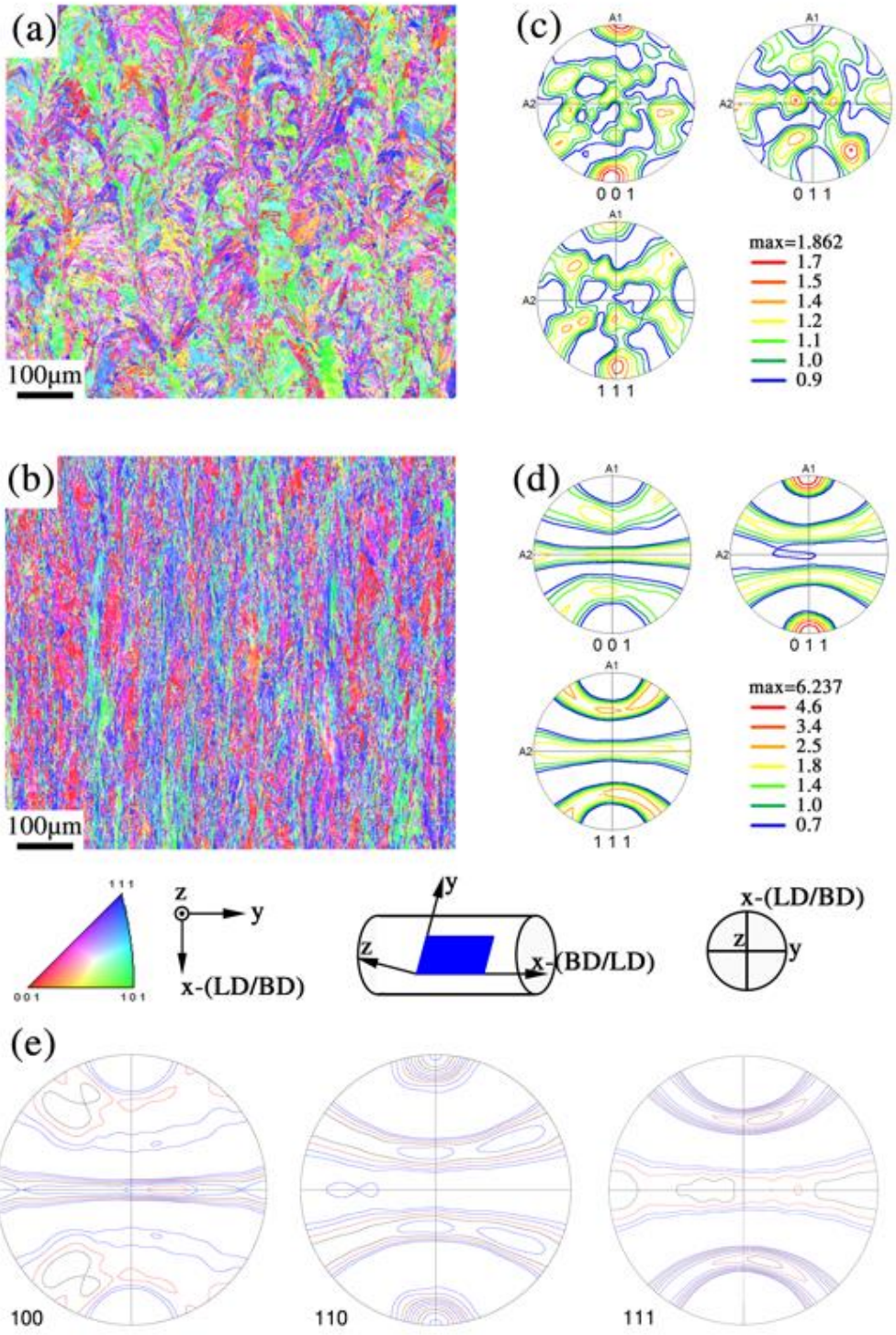

Fig. 4-11 EBSD plots for as-built vertical samples (a): IPF, undeformed, (b): IPF, deformed, (c): PF, undeformed, (d): PF, deformed. (e): texture simulation based on the FC-Taylor model and uniaxial tensile deformation.

Fig. 4-12 shows the EBSD results for the horizontally build, aged samples before and after the tensile test. The ductility is lower than the as-built, and the fracture is occurring in a relatively brittle condition. As a result, melt-pools' elongation is not observed in the IPF plots here despite the as-built case. The load and tensile directions are perpendicular in this case. Similar to the vertically printed sample, the horizontally printed one shows a weak texture with dominant <100> and <111> texture fibres in the undeformed case. The pole figures of the plastically deformed sample depicted in Fig. 4-12(d) show an intensified texture, in which the strong <011> pole is in agreement with the undeformed case in Fig. 4-11(d). As a result of the aged samples' lower ductility, the texture intensity of deformed aged samples is lower than that of the deformed as-built samples.

In Fig. 4-13, the EBSD results conducted on the vertical aged sample are shown. Although the tensile and load directions are aligned in this case, similar to Fig. 4-11, the melt-pools are not deformed significantly, as observed in the as-built case. It is noteworthy that the ductility of the vertically printed samples in the aged condition is the lowest. As a result, the grains, as well as melt-pools, are less likely to strain compared to other cases. As shown in Fig. 4-13(c), the undeformed texture is generally similar to the previous two cases, in which there is a weak texture with the maximum intensity at <100> and <111> poles, showing the <100>-fibre and <111>-fibre textures, respectively. The <110> texture is weakly intensified after the deformation, as shown in Fig. 4-13(d).

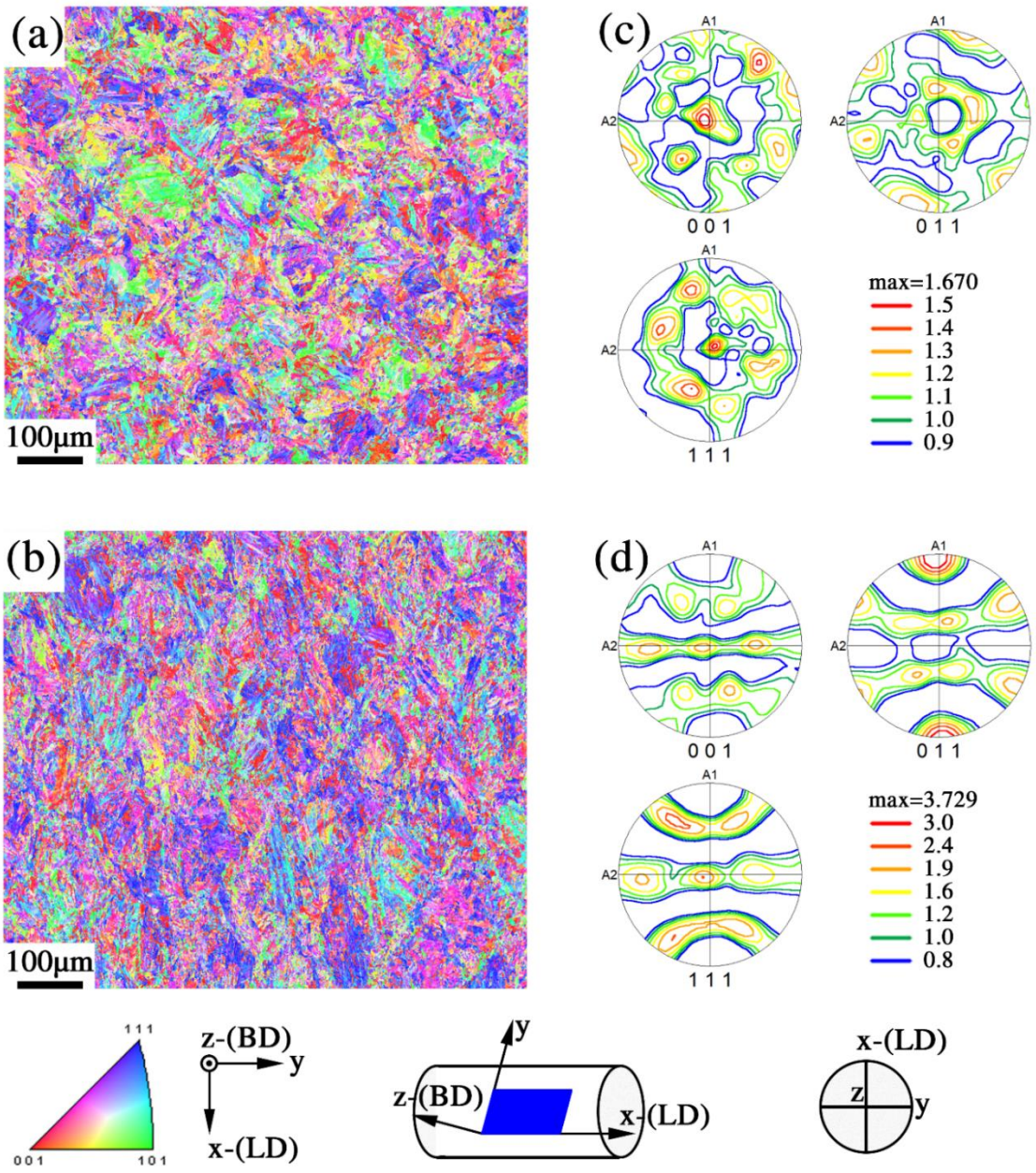

Fig. 4-12 EBSD plots for aged, horizontal samples (a): IPF, undeformed, (b): IPF, deformed, (c): PF, undeformed, (d): PF, deformed.

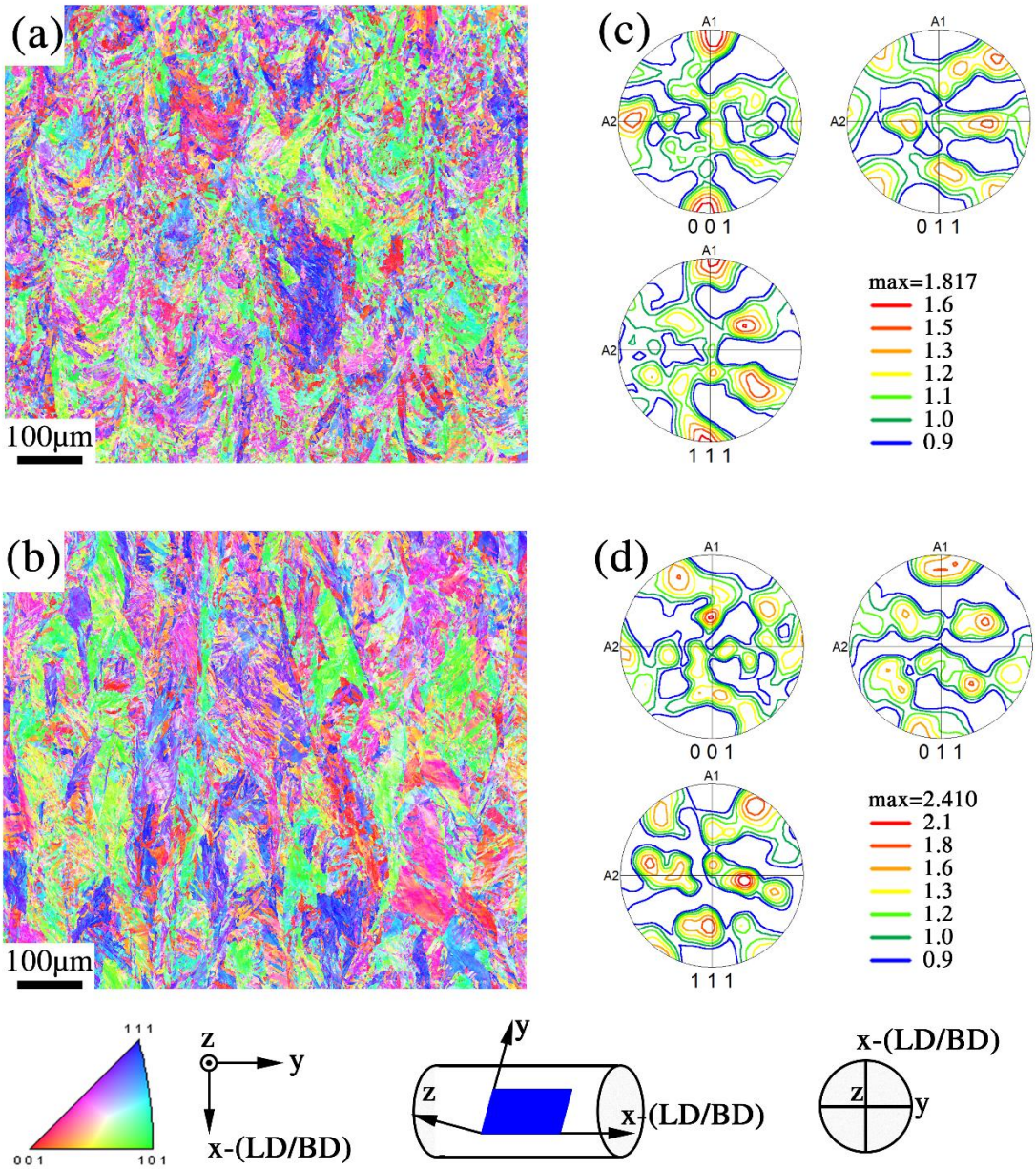

Fig. 4-13 EBSD plots for aged vertical samples (a): IPF, undeformed, (b): IPF, deformed, (c): PF, undeformed, (d): PF, deformed.

4.4 Discussion

4.4.1 Grain structure

By looking through the additive manufactured 18Ni-300 maraging steel in more details, a hierarchical microstructure is discovered. In the as-built condition, the martensite laths are the main structure observed (Galindo-Nava, et al., 2016), along with a lower fraction of the austenite retained from the manufacturing process. The Ti particles tend to form at the lath martensite borders all over the structure (See Fig. 4-6). On the other hand, the cellular structure is formed on a larger scale than the martensitic structure and form in a hexagonal shape and surrounds the martensite laths (Galindo-Nava, et al., 2016). After applying the heat-treatment process, the Ti and Mo alloys segregate into the cell structure in precipitations. The main change from as-built to aged material in terms of strength and hardness has resulted from the nano-scale precipitates observed in the microstructure (Jägle, et al., 2014). The nano-scale reverted austenite phase tends to form and grow at the grain boundaries due to the aging process. On a larger scale, piles of cells with the same orientation form martensite grains with the austenite grains in between (Shamsdini, et al., 2020). The melt-pools are the hierarchy's largest units with over 100 μm size (Mutua, et al., 2018).

4.4.2 Phase transformation

Phase transformation takes place due to the two processes of heating loads and strain deformation (Wang, et al., 2015). The nature of additive manufacturing is to sinter powder particles by applying a heat source and melt the powder, followed by solidification into a solid object. Austenite needs time to form due to its diffusion process (Li, et al., 1995). The laser also applies a concentrated energy source to melt the powder in a small area, and the

energy dissipates rapidly (Xiong, et al., 2018). As a result, there is a lower chance of reverted austenite formation during the manufacturing process. It is also in agreement with Jagle et al. study (Jägle, et al., 2014) showing that the heating cycles do not result in higher austenite formation.

Moreover, martensite formation is a diffusionless process. Our previous study shows that the powder particles consist of 7.4% austenite fraction (Shamsdini, et al., 2020), while through the additive manufacturing process, it has reduced to 4.6-5.1% in the horizontal cases (Shamsdini, et al., 2020). The vertical case has even a lower austenite fraction (2.9%), as observed in Fig. 4-10. It can be concluded that a high number of layers lead to cyclic heat loads. Considering the martensite start and end formation temperatures reported to be 194 and 62 °C (Dos Reis, et al., 2015), it is predictable that each layer deposition ends up with an incremental decrease of austenite through the cooling process. Despite the austenite formation discussed above (having a lower possibility due to the high heating rates), the high cooling rate can not stop the martensite formation due to its diffusionless process. As a result, the impulsive heat load applied to the neighbouring layers can facilitate the phase transformation of the retained austenite into martensite laths (Gilbert, et al., 1962). A higher austenite fraction in the horizontal sample also supports this idea. Generally, the horizontal sample is exposed to fewer layers and fewer heating cycles, respectively. Each cycle can implement a heat load resulting in retained austenite transformed into martensite. Therefore, as observed in Fig. 4-9, the austenite fraction in horizontal builds is higher than the vertical builds.

In the as-built case, the martensitic structure is formed during the solidification process, and a fraction of the austenite is still retained in the microstructure (Shamsdini, et al., 2020).

Reverted austenite, however, is also formed as a result of heat treatment (Sha, et al., 1993). The reverted austenite grains, in addition to the retained austenite present in the as-built state, resulting in a total of austenite phase fraction three times higher than that in the as-built case (See Fig. 4-9). Besides, the deformation results in phase transformation in both cases of as-built and aged (Ali, et al., 1994). The amount of austenite remained is related to the deformation strain. However, in the aged condition, the material expresses a lower ductility. So there is a lower space to transform the austenite phase completely. In the vertical aged sample with the lowest ductility, the situation is even worse, and less fraction of austenite can transform.

4.4.3 Mechanical properties

Mechanical properties of the additive manufactured material are shown to be improved compared to the wrought material. More specifically, in the as-built samples, the mechanical strength is related to the material's micro-ageing through the additive process (Mutua, et al., 2018). Each heating cycle implements a local heat-treatment with very high heating and cooling rates (Gu, et al., 2012)). Since the local ageing contributes to higher strength, the mechanical strength does not vary much with changing the building direction. Besides, the ductility is governed by the austenite content. As explained previously, the horizontal builds have higher austenite content compared to the vertical samples. As a result, higher ductility is expected from the horizontally built samples, which agrees with the current study's measurements.

In the heat-treated case, the strengthening mechanism is the same for both additive and wrought techniques. In both cases, precipitation plays a significant role in increasing mechanical strength (Kempen, et al., 2011). It is also the case for the building direction.

As a result, the yield and ultimate strength are similar amongst the wrought, horizontal, and vertical builds. However, the austenite content again contributes to the ductility resulting in higher ductility of horizontal samples than vertical. The heat-treatment can reduce the anisotropy by affecting the mechanical strength, but it remains in the material's history through ductility.

4.4.4 Deformation mechanism

The austenite to martensite phase transformation through the deformation is known as the TRIP effect (Wang, et al., 2014) (Emadoddin, et al., 2011). Comparing the undeformed and deformed cases (shown in Fig. 4-11, Fig. 4-12, and Fig. 4-13), this phenomenon was observed in the as-built case, while the aged cases showed a TRIP-maraging behaviour as a combination of TRIP-effect in conjunction with the martensite ageing through thermally-induced precipitation of particles (Raabe, et al., 2009). In a bcc/fcc maraging steel such as the current study, the TRIP behaviour can be explained by the Greenwood-Johnson mechanism, in which the plastic strain is induced to austenite phase due to its lower strength and higher relative density compared to the martensite. This phenomenon can also be explained by the Magee mechanism, in which the martensite is formed in a preferred orientation (martensitic variants), resulting in a textured material (Greenwood, et al., 1965) and (Magee, et al., 1966).

Comparing the effect of build orientation and heat treatment simultaneously, the horizontal samples in the as-built condition showed the highest ductility. The aged samples failed in a relatively brittle manner compared to the as-built ones. The additive manufacturing process of the studied alloy implies a texture with the <100> and <111> directions aligned with the part's build direction. Unlike other techniques, the additive

manufacturing layer by layer melting and solidification process implies a high residual stress density (Ding, et al., 2011). In each melting and solidification cycle, a rearrangement of the previous layer's orientation occurs, resulting in fibre textures. As a result, the so-called <100>-fibre and <111>-fibre textures are intensified through the manufacturing process. On the other hand, the deformation strain implies a <110> texture associated with the load direction. Finally, due to relatively low heat treatment temperature compared to the melting point, the grain orientation is not affected by the ageing process.

4.5 Conclusions

In this study, thorough research on the 18Ni-300 maraging steel in horizontal and vertical builds is conducted. A multi-scale characterization is presented in both as-built, and aged conditions and the microstructural evolution is inspected prior and after deformation, and the following results are achieved:

The material shows a hierarchical, mainly martensitic structure with the retained austenite and dispersed alloying elements in the as-built case. In the aged condition, the material develops reverted austenite and precipitates. The cellular structure surrounds the martensite laths and is enclosed with the grains containing piles of martensite or austenite phase with similar orientation. The grain structure is then formed inside the melt-pools.

Additive manufacturing process increases the mechanical strength and ductility in the as-built case, with more increase in the horizontal direction. Besides, the mechanical strength is increased due to heat-treatment into the same range for wrought, horizontal, and vertical additive material. However, the ductility was higher in the horizontal aged samples.

This material shows a long path of phase transformation. In each cycle of heat loads, a portion of retained austenite is transformed into martensite. This cyclic phase transformation implies a texture into the material. The ageing process applies another phase transformation process and results in reverted austenite formation and precipitation simultaneously. However, the texture is not changed through the ageing process.

Deformation is accompanied by phase transformation and evolves the texture towards the <110> direction.

The amount of austenite reversion after the deformation depends on the ductility. For a ductile fracture, the whole austenite phase can transform, while in a brittle fracture, a noticeable amount of austenite remains.

Finally, after ageing, the horizontal build material is considered to have the highest strength and ductility in the tensile test. Since the horizontal builds are faster and less powder is wasted in each build process, it is recommended to consider the relationship between the building direction and the texture orientation in different loading in all the designs for additively manufactured parts in the industry.

4.6 References

Ali A. [et al.] Austenite reversion in cold formed 18 wt-% Ni 350 grade maraging steel [Journal] // Materials science and technology. - 1994. - Vol. 10(2). - pp. 97-101.

Bajaj P. [et al.] Steels in additive manufacturing: A review of their microstructure and properties [Journal] // Materials Science and Engineering: A. - 2020. - Vol. 772. - p. 138633.

Becker T. H. and Dimitrov D. The achievable mechanical properties of SLM produced Maraging Steel 300 components [Journal] // Rapid Prototyping Journal.. - 2016. - pp. 487-494.

Croccolo D. [et al.] Sensitivity of direct metal laser sintering Maraging steel fatigue strength to build orientation and allowance for machining [Journal] // Fatigue & Fracture of Engineering Materials & Structure. - 2019. - Vol. 42(1). - pp. 374-386.

Cyr E. [et al.] Fracture behaviour of additively manufactured MS1-H13 hybrid hard steels [Journal] // Materials Letters. - 2018. - Vol. 212. - pp. 174-177.

Dehgahi S. [et al.] Concurrent improvement of strength and ductility in heat-treated C300 maraging steels produced by laser powder bed fusion technique [Journal] // Additive Manufacturing. - 2021. - p. 101847.

Ding J. [et al.] Thermo-mechanical analysis of Wire and Arc Additive Layer Manufacturing process on large multi-layer parts [Journal] // Computational Materials Science. - 2011. - Vol. 50(12). - pp. 3315-3322.

Dos Reis A. G. [et al.] High-temperature creep resistance and effects on the austenite reversion and precipitation of 18 Ni (300) maraging steel [Journal] // Materials Characterization. - 2015. - Vol. 107. - pp. 350-357.

Dovgyy B. and Pham M. S. Epitaxial growth in 316L steel and CoCrFeMnNi high entropy alloy made by powder-bed laser melting [Journal] // AIP Conference Proceedings. -

2018. - AIP Publishing LLC. : Vol. 1960. - p. 140008.

Emadoddin E. [et al.] Influence of cold-rolling reduction on retained austenite texture in cold-rolled and intercritically annealed TRIP-assisted steel [Journal] // Journal of Applied Crystallography. - 2011. - Vol. 44(6). - p. 119.

Fortunato A. [et al.] Milling of maraging steel components produced by selective laser melting [Journal] // The International Journal of Advanced Manufacturing Technology. - 2018. - Vols. 94(5-8). - pp. 1895-1902.

Galindo-Nava E. I. and Rivera-Díaz-del-Castillo P. E. J. Understanding the factors controlling the hardness in martensitic steels [Journal] // Scripta Materialia. - 2016. - Vol. 110. - pp. 96-100.

Galindo-Nava E. I., Rainforth W. M. and Rivera-Díaz-del-Castillo P. E. J. Predicting microstructure and strength of maraging steels: Elemental optimisation [Journal] // Acta Materialia. - 2016. - Vol. 117. - pp. 270-285.

Gilbert A. and Owen W. S. Diffusionless transformation in iron-nickel, iron-chromium and iron-silicon alloys [Journal] // Acta Metallurgica. - 1962. - Vol. 10(1). - pp. 45-54.

Greenwood G. W. and Johnson R. H. The deformation of metals under small stresses during phase transformations [Journal] // Proceedings of the Royal Society of London. Series A. Mathematical and Physical Sciences. - 1965. - Vol. 283(1394). - pp. 403-422.

Gu D. D. [et al.] Laser additive manufacturing of metallic components: materials, processes and mechanisms [Journal] // International materials reviews. - 2012). - Vol. 57(3). - pp. 133-164.

Guo Z., Sha W. and Li D. Quantification of phase transformation kinetics of 18 wt.% Ni C250 maraging steel [Journal] // Materials Science and Engineering: A. - 2004. - Vols. 373(1-2). - pp. 10-20.

Hadadzadeh A. [et al.] Role of hierarchical microstructure of additively manufactured AlSi10Mg on dynamic loading behavior [Journal] // Additive Manufacturing. - 2019. - Vol. 28. - pp. 1-13.

Handbook A. S. M. Properties and selection: irons, steels and high performance alloys [Book]. - [s.l.] : The materials information company, 1990. - Vol. 1.

Hosford W. F. Mechanical behavior of materials [Book]. - [s.l.] : Cambridge university press, 2010.

Houtte P. Van The MTM-FHM Software System Version 2 [Journal] // Users Manual. - 1995. - KU Leuven.

Jägle E. A. [et al.] Comparison of maraging steel micro-and nanostructure produced conventionally and by laser additive manufacturing [Journal] // Materials. - 2017. - Vol. 10(1). - p. 8.

Jägle E. A. [et al.] Precipitation and austenite reversion behavior of a maraging steel produced by selective laser melting [Journal] // Journal of Materials Research. - 2014. - Vol. 29(17). - pp. 2072-2079.

Kempen K. [et al.] Microstructure and mechanical properties of Selective Laser Melted 18Ni-300 steel [Journal] // Physics Procedia. - 2011. - Vol. 12. - pp. 255-263.

Kuo Y. L., Horikawa S. and Kakehi K. Effects of build direction and heat treatment on creep properties of Ni-base superalloy built up by additive manufacturing [Journal] // Scripta Materialia. - 2017. - Vol. 129. - pp. 74-78.

Li X. and Yin Z. Reverted austenite during aging in 18Ni (350) maraging steel [Journal] // Materials Letters. - 1995 . - Vol. 24(4). - pp. 239-242.

Magee C. L. and Paxton H. W. Transformation kinetics, microplasticity and aging of martensite in Fe-31 Ni [Report]. - [s.l.] : Carnegie institute of technology Pittsburgh PA, 1966.

Material data sheet EOS Maraging Steel MS1. - [s.l.] : GmbH-Electro Optical System, 2017.

Meneghetti G. [et al.] Influence of build orientation on static and axial fatigue properties of maraging steel specimens produced by additive manufacturing [Journal] // Procedia Structural Integrity. - 2017. - Vol. 7. - pp. 149-157.

Mohammadi M. and Asgari H. Achieving low surface roughness AlSi10Mg_200C parts using direct metal laser sintering [Journal] // Additive Manufacturing. - 2018. - Vol. 20. - pp. 23-32.

Mooney B. [et al.] Process phenomena influencing the tensile and anisotropic characteristics of additively manufactured maraging steel [Journal] // Materials Science and Engineering: A. - 2019. - Vol. 745. - pp. 115-125.

Mooney B. and Kourousis K. I. A Review of Factors Affecting the Mechanical Properties of Maraging Steel 300 Fabricated via Laser Powder Bed Fusion [Journal] // Metals. - 2020. - Vol. 10(9). - p. 1273.

Mooney B., Kourousis K. I. and Raghavendra R. Plastic anisotropy of additively manufactured maraging steel: Influence of the build orientation and heat treatments [Journal] // Additive Manufacturing. - 2019. - Vol. 25. - pp. 19-31.

Mutua J. [et al.] Optimization of selective laser melting parameters and influence of post heat treatment on microstructure and mechanical properties of maraging steel [Journal] // Materials & Design. - 2018. - Vol. 139. - pp. 486-497.

Raabe D. [et al.] Designing ultrahigh strength steels with good ductility by combining transformation induced plasticity and martensite aging [Journal] // Advanced Engineering Materials. - 2009. - Vol. 11(7). - pp. 547-555.

Raabe D. [et al.] Segregation engineering enables nanoscale martensite to austenite phase transformation at grain boundaries: A pathway to ductile martensite [Journal] // Acta Materialia. - 2013. - Vol. 61. - pp. 6132-6152.

Schneider C. A., Rasband W. S. and Eliceiri K. W. NIH Image to ImageJ: 25 years of image analysis [Journal] // Nature methods. - 2012. - Vol. 9(7). - pp. 671-675.

Sha W., Cerezo A. and Smith G. D. W. Phase chemistry and precipitation reactions in maraging steels: Part I. Introduction and study of Co-containing C-300 steel [Journal] // Metallurgical and Materials Transactions A. - 1993. - Vol. 24(6). - pp. 1221-1232.

Sha Wei and Guo Zhanli Maraging Steels, Modeling of Microstructure, Properties and Applications [Book]. - [s.l.] : Woodhead Publishing, 2009.

Shakerin S. [et al.] Additive manufacturing of maraging steel-H13 bimetals using laser powder bed fusion technique [Journal] // Additive Manufacturing. - 2019. - Vol. 29. - p. 100797.

Shamsdini S. [et al.] A trade-off between powder layer thickness and mechanical properties in additively manufactured maraging steels [Journal] // Materials Science and Engineering: A. - 2020. - Vol. 776. - p. 139041.

Shamsdini S. [et al.] Plastic deformation throughout strain-induced phase transformation in additively manufactured maraging steels [Journal] // Materials & Design. - 2020. - p. 109289.

Standard A. S. T. M. ASTM E8/E8M-15a [Journal] // ASTM Standards. - [s.l.] : Standard Test Methods for Tension Testing of Metallic Materials, 2015.

Sun S. H. [et al.] Electron beam additive manufacturing of Inconel 718 alloy rods: Impact of build direction on microstructure and high-temperature tensile properties [Journal] // Additive Manufacturing. - 2018. - Vol. 23. - pp. 457-470.

Suryawanshi J., Prashanth K. G. and Ramamurty U. Tensile, fracture, and fatigue crack growth properties of a 3D printed maraging steel through selective laser melting [Journal] // Journal of Alloys and Compounds. - 2017. - Vol. 725. - pp. 355-364.

Tan C. [et al.] Microstructural characterization and properties of selective laser melted

maraging steel with different build directions [Journal] // Science and Technology of Advanced Materials. - 2018. - Vol. 19(1). - pp. 746-758.

Tan C. [et al.] Microstructural evolution, nanoprecipitation behavior and mechanical properties of selective laser melted high-performance grade 300 maraging steel [Journal] // Materials & Design. - 2017. - Vol. 134. - pp. 23-34.

Vasudevan V. K., Kim S. J. and Wayman C. M. Precipitation reactions and strengthening behavior in 18 Wt Pct nickel maraging steels [Journal] // Metallurgical Transactions A. - 1990. - Vol. 21(10). - pp. 2655-2668.

Vishwakarma J., Chattopadhyay K. and Srinivas N. S. Effect of build orientation on microstructure and tensile behaviour of selectively laser melted M300 maraging steel [Journal] // Materials Science and Engineering: A. - 2020. - Vol. 798. - p. 140130.

Wang M. M. [et al.] Nanolaminate transformation-induced plasticity–twinning-induced plasticity steel with dynamic strain partitioning and enhanced damage resistance [Journal] // Acta Materialia. - 2015. - Vol. 85. - pp. 216-228.

Wang M. M. [et al.] Smaller is less stable: size effects on twinning vs. transformation of reverted austenite in TRIP-maraging steels [Journal] // Acta Materialia. - 2014. - Vol. 79. - pp. 268-281.

Wang Y. M. [et al.] Additively manufactured hierarchical stainless steels with high strength and ductility [Journal] // Nature materials. - 2018. - Vol. 17(1). - pp. 63-71.

Weinberger C. R., Boyce B. L. and Battaile C. C. Slip planes in bcc transition metals [Journal] // International Materials Reviews. - 2013. - Vol. 58(5). - pp. 296-314.

Xiong J. [et al.] Heat propagation of circular thin-walled parts fabricated in additive manufacturing using gas metal arc welding [Journal] // Journal of Materials Processing Technology. - 2018. - Vol. 251. - pp. 12-19.

Xu X. [et al.] Improving mechanical properties of wire plus arc additively manufactured

maraging steel through plastic deformation enhanced aging response [Journal] // Materials Science and Engineering: A. - 2019. - Vol. 747. - pp. 111-118.

Xu X. [et al.] Microstructural evolution and mechanical properties of maraging steel produced by wire+ arc additive manufacture process [Journal] // Materials Characterization. - 2018. - Vol. 143. - pp. 152-162.

Yuan L. [et al.] Nanoscale austenite reversion through partitioning, segregation and kinetic freezing: Example of a ductile 2 GPa Fe–Cr–C steel [Journal] // Acta Materialia. - 2012. - Vols. 60(6-7). - pp. 2790-2804.

Zhou F. [et al.] Effect of aging treatment on microstructure and properties of additively manufactured maraging steel [Journal] // Ironmaking & Steelmaking. - 2020. - Vol. 47(9). - pp. 980-985.

Chapter 5
Effect of recoater-blade type on the mechanical properties and microstructure of additively manufactured maraging steels

Abstract

The application of soft and hard recoater-blades is studied on the mechanical properties and microstructure of additively manufactured maraging steels. The soft recoater-blade leads to unmelted powders as an initial site for premature fracture. Lower retained austenite fraction ends up with lower phase transformation, strain hardening and ductility.

Keywords: Maraging steel; additive manufacturing; building direction; deformation.

5.1 Introduction

Among all the process parameters affecting the additive manufacturing parts, the recoater blade type directly impacts the powder's packing density in the LPBF technique (Meier, et al., 2019). The recoater blade applies pressure along the building-direction to the powder particles and results in a densely packed powder layer (Kozhevnikov, et al., 2019). When a soft blade (such as a carbon fibre brush) is applied to deposit powder particles, the particles are spread gently without any applied pressure. Snow et al. (Snow, et al., 2019) showed that soft and hard recoater blades affected the powder spreadability over the build plate. However, they observed that the spreadability is more prone to the flowability of the powder. In other research conducted by Dana et al. (Daňa, et al., 2019), the hard recoater blade was observed to apply vibration due to contact with the support structure resulting in inconsistent powder distribution and, subsequently, cavities formation. Austenite reversion was investigated recently through the ageing process, and cyclic heat loads were shown to

improve the mechanical properties by austenite reversion (Conde, et al., 2019) (Conde, et al., 2019).

Comprehensive studies have been conducted on different process parameters affecting the microstructure and mechanical properties of 18Ni-300 maraging steel (Shamsdini, et al., 2020) (Mutua, et al., 2018) (Oliveira, et al., 2020). However, a study on the effect of recoater blade on the mechanical properties and microstructure of 18Ni-300 maraging steel is overlooked in the literature. Thus, the mechanical properties and microstructure of the maraging steel produced using the brush and ceramic recoater blades are compared in the current study. Finally, the XRD technique is conducted to investigate the deformation behaviour of the samples.

5.2 Experimental procedure

Gas atomized 18Ni-300 maraging steel powder was used in an EOS M290 machine. Two different types of soft (carbon fibre brush) and hard (ZrO2 ceramic) recoater blades were used to deposit the powder particles over a build plate. The powder was spread with a 200% dosing factor. The build plate was preheated at 40°C, and nitrogen gas was blown to reduce the building chamber's oxygen content. A 400W Yb-fiber laser was employed to melt the powder with a laser spot size of 100µm, laser power of 285W, powder layer thickness of 40µm, laser scan speed of 960 mm/s, and hatch spacing of 110µm. The process parameters were adjusted to reach the lowest possible porosity fraction. The chemical composition of the powder is presented in Table 5.1.

Table 5.1 Chemical composition of the maraging steel MS1 feedstock powder (sheet, 2017).

Element	Ni	Co	Mo	Ti	Al	Cr	Cu	C	Mn	Si	P	S
Ave. %	18.00	9.00	4.85	0.70	0.10	0.25	0.25	0.015	0.05	0.05	0.005	0.005
± %	1.00	0.50	0.35	0.10	0.05	0.25	0.25	0.015	0.05	0.05	0.005	0.005

The cylindrical samples were produced in the vertical direction using a stripe scanning strategy with a 67° rotation angle. All experiments performed in the current study were under the as-built condition, and no heat-treatment was conducted on the specimens. Samples were then machined to form uniaxial tensile test specimens with 30mm gauge length and 6mm in diameter (Standard, 2015). A 1332 universal hydraulic Instron performed the tensile tests in a quasi-static state with a 9×10^{-3} s^{-1} strain rate using a 25mm extensometer. The tensile tests have been repeated at least three times, and typical stress-strain curves were plotted. Porosity measurements were performed using a Zeta-20 optical microscope, and pores were identified based on the image contrast with the metal base using an image processing technique. Rockwell hardness measurements were performed over four layers of the material underneath the top surface using a CRM Clark Rockwell hardness machine. HRC scale measurements were performed, applying a 150kg load over the diamond indenter head. Each measurement was performed at least ten times to assure statistical soundness. A fine polishing up to 1µm was followed by etching with 3% Nital over a period of 120s. A Jeol 6400 SEM instrument was then carried out to characterize the etched surfaces and fracture surfaces.

Further studies were then conducted using an X-ray Diffraction (XRD) technique. A Brucker D8 instrument with a Co-Kα radiation source was used with 45mA and 35kV over a 2θ range of 45-130°. The texture measurements were also performed using a VANTEC 500 area detector with 5mm oscillation. The XRD studies were collected from the undeformed zone and the ones very close to the fracture area, representing undeformed and

deformed materials. The reference system defined in the current study is shown in Fig. 5-5(e) with load and building directions along the x-axis and XRD data along the z-axis. The phase fraction was measured based on the Rietveld technique by counting the bcc and fcc peaks representing martensite and austenite phases as major microstructure phases. Orientation distribution functions (ODF) were then calculated. For simplicity, the samples are designated as LPBF-Brush and LPBF-Ceramic in the current study.

5.3 Results

Fig. 5-1 shows the microstructure of both LPBF-Brush and LPBF-Ceramic samples. In Fig. 5-1(a), the LPBF-Brush melt-pools are shown to be orderly patterned without any apparent porosity or crack. Fig. 5-1(b-c) reveals melt-pool boundaries surrounding the columnar/equiaxed structure. Besides, the columnar structure is parallelly elongated in each melt-pool (Shakerin, et al., 2019). The triple junctions are also shown in Fig. 5-1(b-c), where the orientation of the cellular structure in each melt-pool is different. The scan tracks of LPBF-Ceramic are shown in Fig. 5-1(d). The triple junction demonstrates consistency in the orientation of the cells within the neighbouring melt-pools since they are mostly equiaxed with no preferential orientation, Fig. 5-1(e-f).

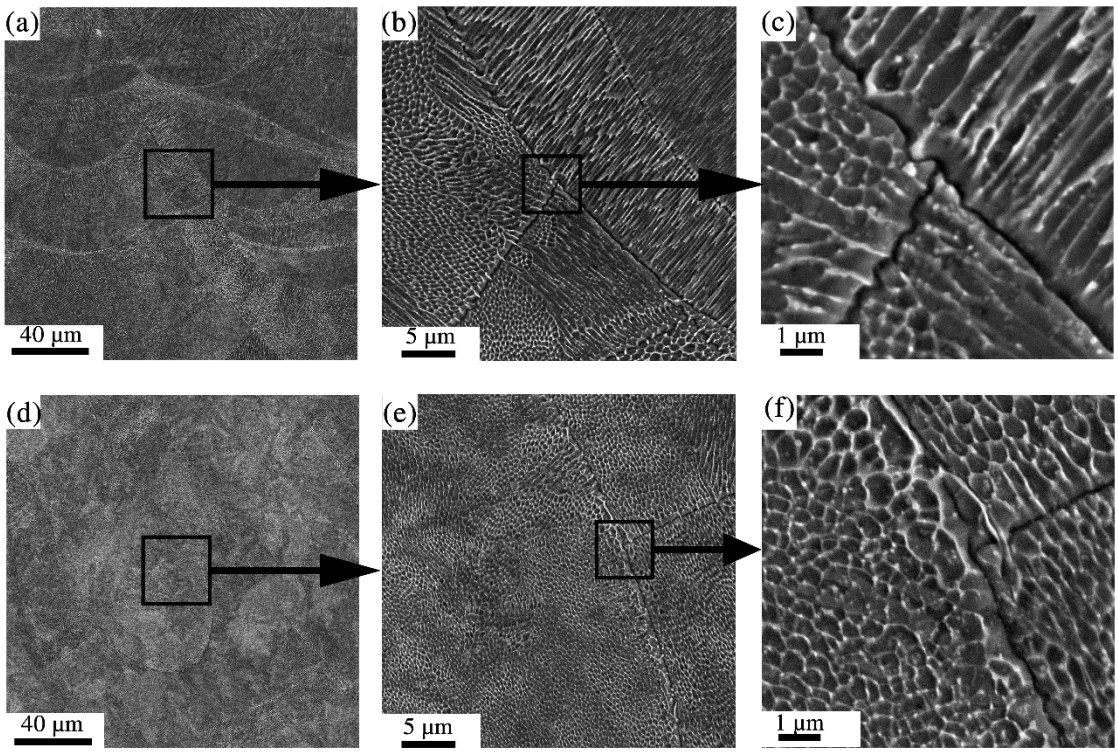

Fig. 5-1 SEM in different magnifications for (a,b,c): *LPBF-Brush*, (d,e,f): *LPBF-Ceramic*.

Fig. 5-2 shows the stress-strain curves comparing the mechanical properties of the LPBF-Brush samples with the LPBF-Ceramic ones. Yield and ultimate strengths are very close, while the ductility and strain hardening is severely lower for the LPBF-Brush results. The inconsistency shown in the LPBF-Brush sample close to the fracture is due to the necking phenomenon occurring very close to the gauge border, resulting in a plastic deformation extending beyond the gauge length. This strange behaviour is observed for all samples with no exception. However, the data before ultimate strength is similar to the LPBF-Ceramic case.

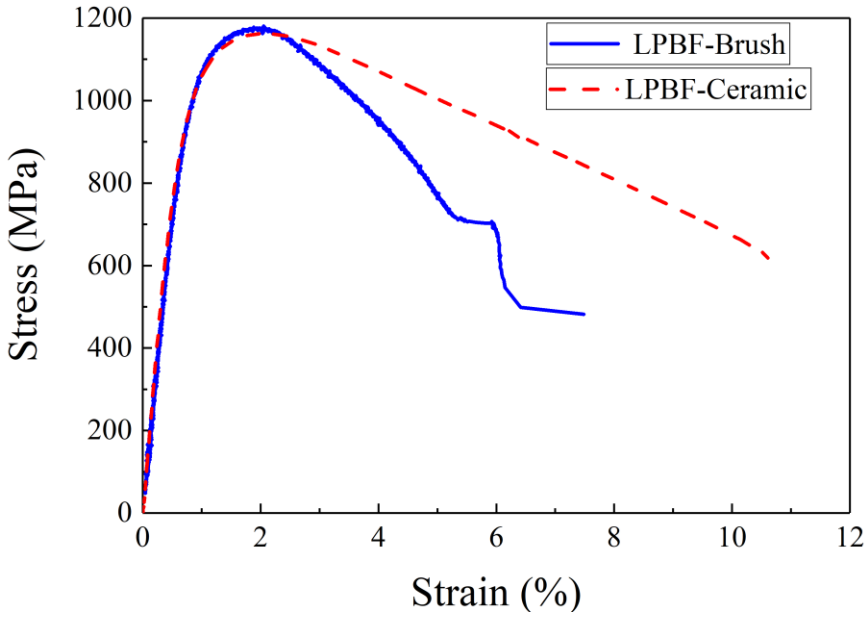

Fig. 5-2 Engineering stress-strain curves comparing *LPBF-Brush* and *LPBF-Ceramic* samples.

The values of porosity and hardness of LPBF-Brush and LPBF-Ceramic samples are measured through the depth and shown in Fig. 5-3(a,b). In Fig. 5-3(a), the hardness shows a gradual increase through the depth while the porosity increases at first and then decreases underneath the top surface in the LPBF-Brush sample. On the other hand, the LPBF-Ceramic sample shown in Fig. 5-3(b) (Shamsdini, et al., 2020), shows the hardness increase through the depth followed by a drop at deeper levels. The porosity decreases in deeper layers in agreement with the LPBF-Brush case. Porosity measurements in both cases reveal an almost fully dense material at deeper layers.

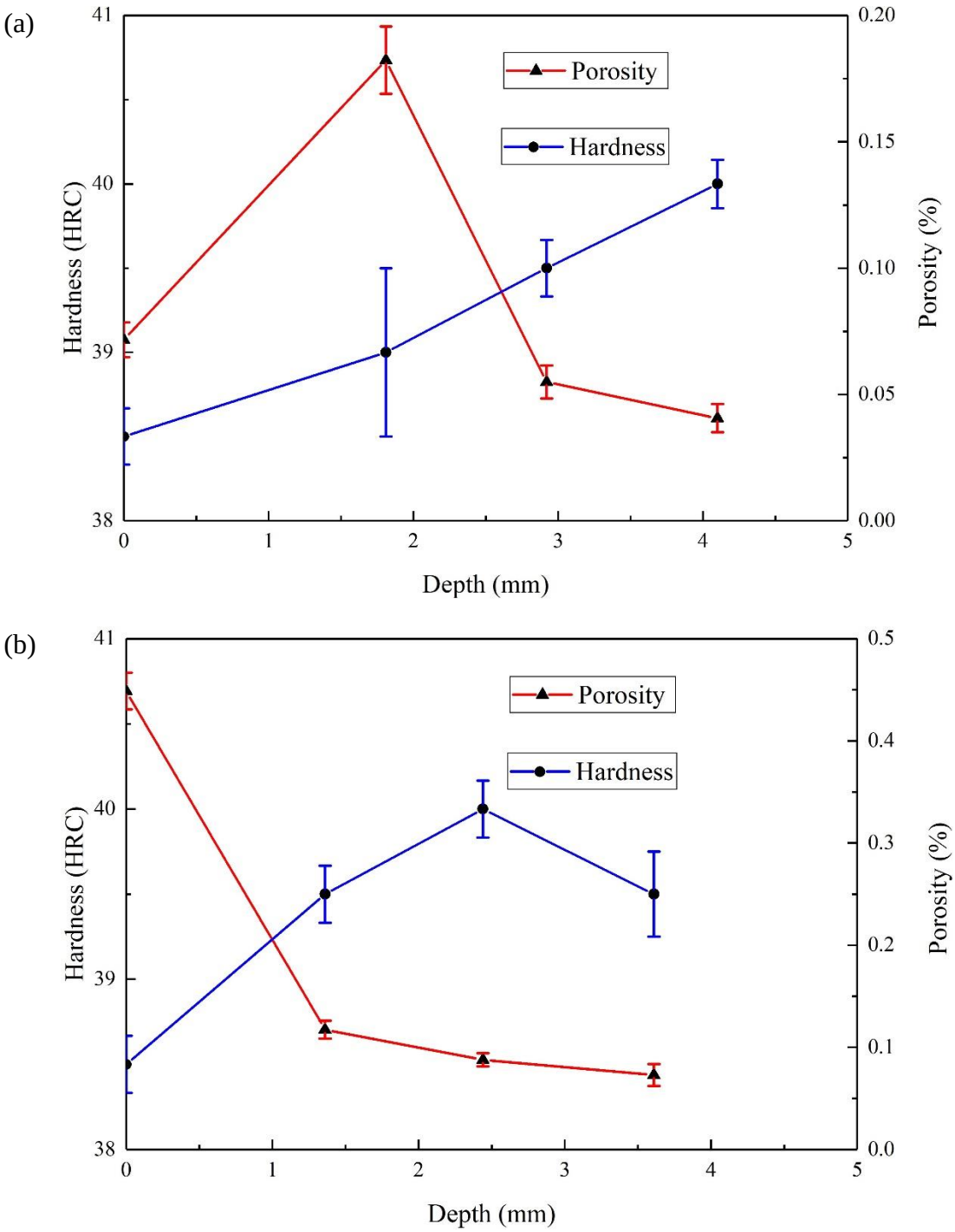

Fig. 5-3 Porosity and hardness measured through the depth (a): LPBF-Brush sample, (b): LPBF-Ceramic sample (Shamsdini, et al., 2020).

Fig. 5-4 shows the SEM fractography at different magnifications for both LPBF-Brush and LPBF-Ceramic samples. Fig. 5-4(a-b) shows the fracture surface of LPBF-Ceramic at

low and high magnifications. Necking along with the voids is representing a ductile fracture. In Fig. 5-4(c-f), necking is shown in the micrographs for the LPBF-Brush sample. Dimples, along with the cup and cones, show a ductile fracture (Cyr, et al., 2018). Fig. 5-4(e-f) illustrates an unmelted powder particle in the LPBF-Brush sample. Without proper packing of the powder layer in the LPBF-brush samples, more significant gaps are formed than the LPBF-Ceramic due to the presence of unmelted powder particles.

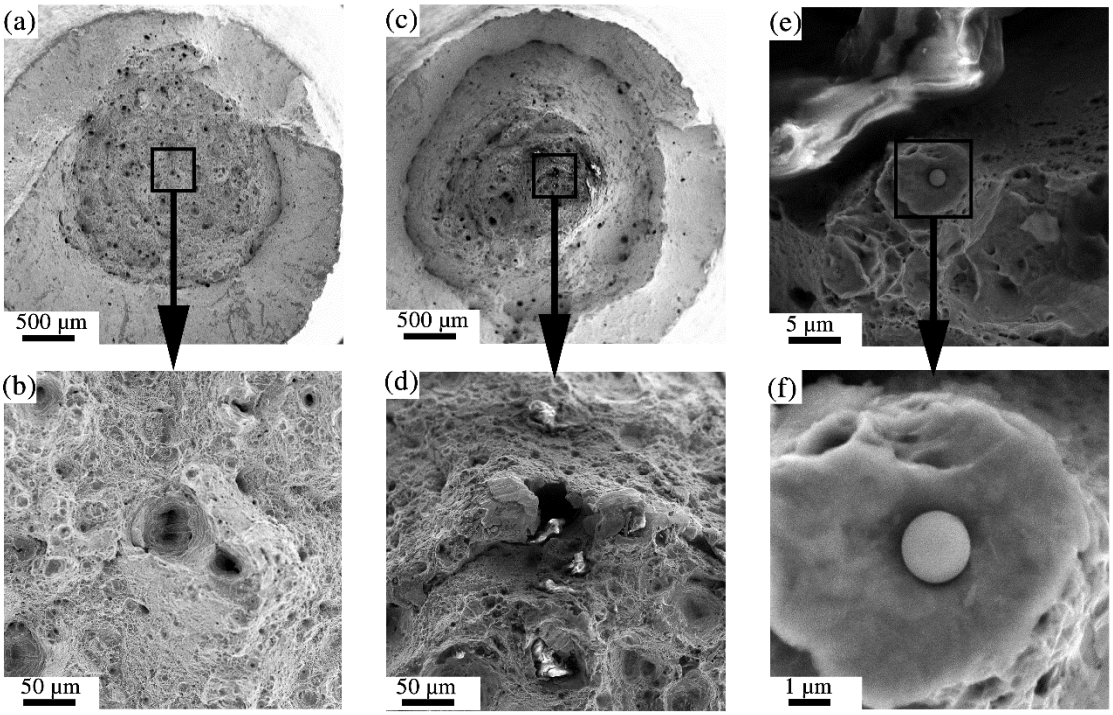

Fig. 5-4 SEM at low and high magnifications for (a-b): *LPBF-Ceramic*, and (c-f): *LPBF-Brush.*

Fig. 5-5 shows the XRD-ODF analysis before and after the deformation. The ODF graph is shown in Fig. 5-5(a) and reveals a relatively oriented texture along with the <001>-fibre normal to building direction in the undeformed LPBF-Ceramic sample. After deformation of the LPBF-Ceramic sample, the texture shows an evolution through <110>-fibre normal to the load direction as shown in Fig. 5-5(b). Similar textures are depicted in Fig. 5-5(c-d) for the LPBF-Brush sample in the undeformed and deformed cases. Fig. 5-5(c) shows the

undeformed samples for the LPBF-Brush, with <001> texture normal to building direction, while <110>-fibre normal to the load direction after deformation is depicted in Fig. 5-5(d). The texture evolution agrees with previous works conducted on maraging steel (Shamsdini, et al., 2020) (Shamsdini, et al., 2021). Since the ODF map results show similar behaviour in both LPBF-Brush and LPBF-Ceramic before and after deformation, it can be concluded that the microstructural evolution through the additive process and deformation is not affected by the recoater type.

The intensity variation was also measured for LPBF-Brush and LPBF-Ceramic. The XRD analysis showed that the LPBF-Brush sample austenite fraction reduced from 2.0% to 0.0%, while the reduction was from 3.0% to 0.0% in the LPBF-Ceramic. This reduction occurs during deformation-induced austenite to martensite phase transformation, which agrees with the ODF maps' texture evolution.

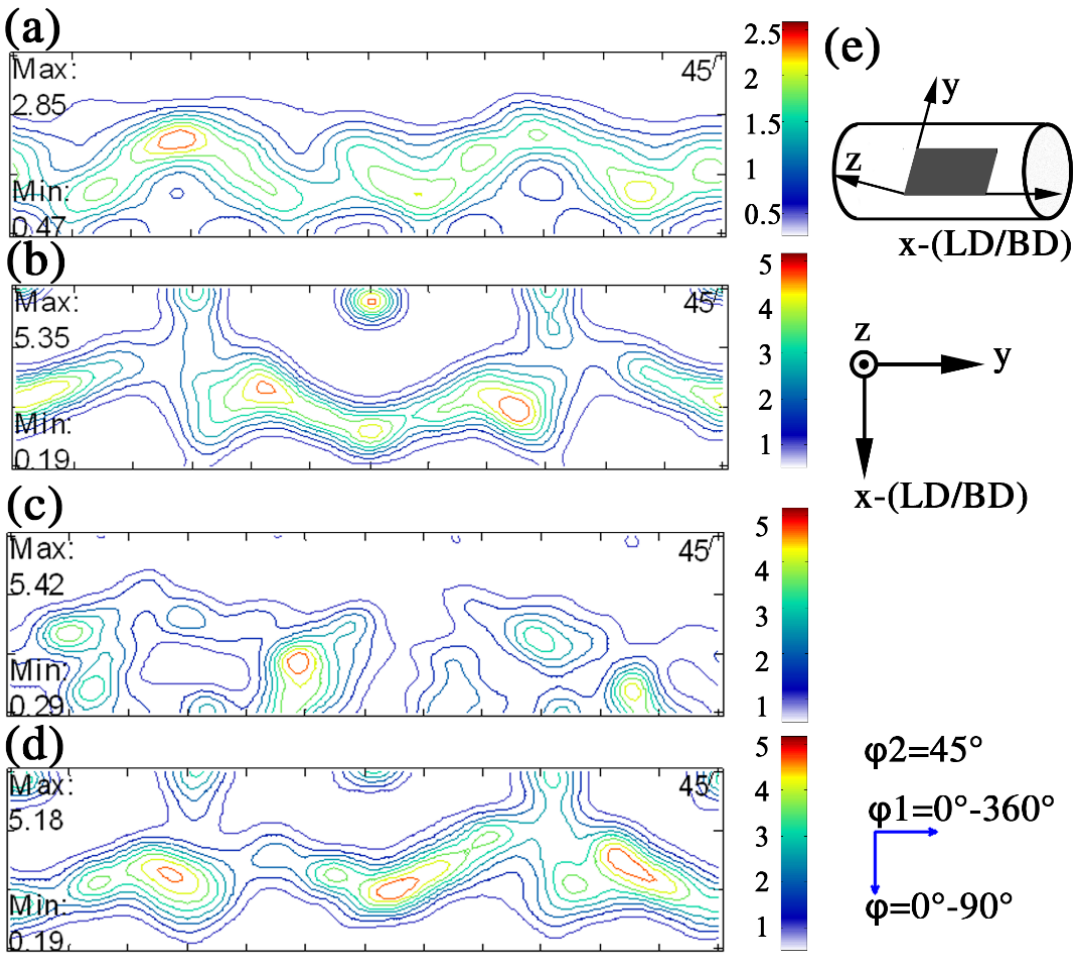

Fig. 5-5 XRD-ODF graphs for *LPBF-Ceramic* samples (a): undeformed, (b): deformed, *LPBF-Brush* (c): undeformed, (d): deformed, and (e): reference system.

5.4 Discussion

Comparing the current study with the literature shows that the recoater type does not affect the hardness variation (Shamsdini, et al., 2020). The overall porosity level shows a high-density material, while there is an increase in the porosity level 2mm deep inside the samples (i.e., 50 layers of powder deposition equivalent to 50 cycles of the remelting process). It can be concluded that deeper layers are prone to higher numbers of reheating cycles. The residual thermal stresses lead to the shrinkage of porosities (Narvan, et al., 2019). The last few layers are less exposed to cyclic thermal stresses. As a result, the

porosity decreases beneath the surface. This reduction of porosity through the depth agrees with previous studies on samples built using ceramic blades (Shamsdini, et al., 2020). However, the last few layers have lower porosity due to the change of the process parameters in the up-skin contour (Mohammadi, et al., 2018). The hardness is gradually increasing beneath the surface, which agrees with higher residual stresses in the lower layers. The slight increase of the hardness through the depth agrees with the literature (Shamsdini, et al., 2020).

An unmelted powder left behind in the melting process leads to a decohesion and detachment of the microstructure. It is also in agreement with lower ductility, which is evidence of premature failure due to crack formation (Yuan, et al., 2012). Despite the hard recoater that applies pressure to pack the powder layer firmly, the soft recoater gently spreads the powder, facilitating the smaller powder particles' movement.

The retained austenite's initial fraction prior to deformation is relatively lower in the LPBF-Brush than the LPBF-Ceramic. Despite a low porosity level, the LPBF-Brush samples seem to be prone to microvoids and unmelted powders resulting in the prevention of retained austenite formation. In other words, very high cooling rates through the additive process and the presence of microvoids lead to the formation of a higher fraction of martensite. The deformation-induced phase transformation leads to the transformation of retained austenite, resulting in a fully martensitic structure. With a lower initial fraction of retained austenite, the phase transformation has a lower capacity to occur, while after the completion of phase transformation, the material has lower room left for further plasticity. In other words, the initial austenite fraction increases the capacity of materials ductility.

The low ductility of the LPBF-Brush samples is in agreement with the lower retained austenite value, as illustrated in Fig. 5-2 (Sugimoto, et al., 1992).

5.5 Conclusions

In this paper, soft and hard recoater-blades were used to produce 18-Ni-300 maraging steel samples using the LPBF technique. Mechanical properties and microstructure of the LPBF-Brush samples were studied and compared to the LPBF-Ceramic. The highlights of this study can be summarized as:

The strength was not affected by the recoater type, while the ductility was drastically reduced. Furthermore, the porosity and hardness values were not much affected by changing the recoater blade. In other words, the melt-pools did not show any pores or cracks while using a soft recoater.

Fractography showed that the presence of unmelted powder could substantially affect the fracture mechanism, resulting in the material's premature failure.

The deformation led to phase transformation. The austenite phase completely transformed, and the texture evolved, leading to a textured material. A lower fraction of retained austenite contributed to a lower ductility.

5.6 References

Conde F. F. [et al.] Austenite reversion kinetics and stability during tempering of an additively manufactured maraging 300 steel [Journal] // Additive Manufacturing. - 2019. - Vol. 29. - p. 100804.

Conde F. F. [et al.] Effect of thermal cycling and aging stages on the microstructure and bending strength of a selective laser melted 300-grade maraging steel [Journal] // Materials Science and Engineering: A. - 2019. - Vol. 758. - pp. 192-201.

Cyr E. [et al.] Fracture behaviour of additively manufactured MS1-H13 hybrid hard steels [Journal] // Materials Letters. - 2018. - Vol. 212. - pp. 174-177.

Daňa M., Zetková I. and Hanzl P. The influence of a ceramic recoater blade on 3D printing using direct metal laser sintering [Journal]. - 2019.

Kozhevnikov A. [et al.] Investigation of the fluid flow during the recoating process in additive manufacturing [Journal] // Rapid Prototyping Journal. - 2019.

Meier C. [et al.] Critical influences of particle size and adhesion on the powder layer uniformity in metal additive manufacturing [Journal] // Journal of Materials Processing Technology. - 2019. - Vol. 266. - pp. 484-501.

Mohammadi M. and Asgari H. Achieving low surface roughness AlSi10Mg_200C parts using direct metal laser sintering [Journal] // Additive Manufacturing. - 2018. - Vol. 20. - pp. 23-32.

Mutua J. [et al.] Optimization of selective laser melting parameters and influence of post heat treatment on microstructure and mechanical properties of maraging steel [Journal] // Materials & Design. - 2018. - Vol. 139. - pp. 486-497.

Narvan M., Al-Rubaie K. S. and Elbestawi M. Process-structure-property relationships of AISI H13 tool steel processed with selective laser melting [Journal] // Materials. - 2019. - Vol. 12(14). - p. 2284.

Oliveira J. P., LaLonde A. D. and Ma J. Processing parameters in laser powder bed fusion metal additive manufacturing [Journal] // Materials & Design. - 2020. - Vol. 193. - p. 108762.

Shakerin S. [et al.] Additive manufacturing of maraging steel-H13 bimetals using laser powder bed fusion technique [Journal] // Additive Manufacturing. - 2019. - Vol. 29. - p. 100797.

Shamsdini S. [et al.] A trade-off between powder layer thickness and mechanical properties in additively manufactured maraging steels [Journal] // Materials Science and Engineering: A. - 2020. - Vol. 776. - p. 139041.

Shamsdini S. [et al.] Plastic deformation throughout strain-induced phase transformation in additively manufactured maraging steels [Journal] // Materials & Design. - 2021. - Vol. 198. - p. 109289.

sheet Material data EOS MaragingSteel MS1 [Report]. - München : EOS GmbH - Electro Optical Systems, 2017.

Snow Z., Martukanitz R. and Joshi S. On the development of powder spreadability metrics and feedstock requirements for powder bed fusion additive manufacturing [Journal] // Additive Manufacturing. - 2019. - Vol. 28. - pp. 78-86.

Standard A. S. T. M. [Journal] // ASTM E8/E8M-15a. - [s.l.] : Standard Test Methods for Tension Testing of Metallic Materials, 2015.

Sugimoto K. I., Kobayashi M. and Hashimoto S. I. Ductility and strain-induced transformation in a high-strength transformation-induced plasticity-aided dual-phase steel [Journal] // Metallurgical Transactions A. - 1992. - Vol. 23(11). - pp. 3085-3091.

Yuan L. [et al.] Nanoscale austenite reversion through partitioning, segregation and kinetic freezing: Example of a ductile 2 GPa Fe–Cr–C steel [Journal] // Acta Materialia. - 2012. - Vols. 60(6-7). - pp. 2790-2804.

Chapter 6

Summary

6.1 Final remarks

The four projects conducted in this thesis investigated different aspects of the additive manufacturing process's effect on the products. By implementing this work's outcome, one can select appropriate process parameters to achieve the required properties while reducing the manufacturing time and lowering the powder waste.

Maraging steel showed to have similar mechanical properties in higher powder layer thicknesses. Increasing the powder layer thickness and reducing the energy density led to faster manufacturing and lower energy consumption. A successful increase of 25% in powder layer thickness equal to 25% faster building time was achieved, while 19% of energy was saved through the melting process, as explained in more detail in chapter two.

18Ni-300 maraging steel showed the formation of fibre texture through the manufacturing process. The formation of <001> texture normal to the building direction revealed that grains tend to form in elongated shapes along the building direction. The <111> texture fibres normal to the building direction indicated martensite formation through the manufacturing process. The deformation of the material led to an increase in the low angle grain boundaries and decreased grain size. Those observations agreed with the increase in dislocation density and phase transformation. Maraging steel showed a complete deformation-induced phase transformation, and austenite disappeared at the severe deformation region. Phase transformation was accompanying rotation of previous

<001> and <111> textures and forming a new <110> texture normal to the load direction. Strain hardening showed to increase due to phase transformation and stop when the material is entirely martensite. The geometric softening then dominated to show a decrease in the strain hardening.

Samples manufactured in the horizontal direction showed higher mechanical properties compared to vertical. Elongated grains parallel to the building direction showed to increase the strength and ductility. However, ageing increased the strength regardless of the building direction. Since the precipitation was increasing the dislocation density, aged samples were showing similar strength in different directions. On the other hand, the ductility was governed by both the austenite content and the grain orientations. The two factors were assisting horizontal builds to show higher ductility in both as-built and aged cases. The austenite content was also related to the number of heat loads applied through the manufacturing process. Higher numbers of layers resulted in higher martensite transformation, which led to lower austenite and ductility.

The recoater blade showed to affect the mechanical properties. Although the strength was shown to be similar, the soft recoater led to the formation of unmelted powder through the manufacturing process resulting in lower ductility. The deformation behaviour of both soft and hard recoater cases was shown to be similar in terms of texture formation.

6.2 Additional information on the published articles

A summary of the findings in each project is presented below along with some additional information in order to clarify the results and analyses better.

The first project in chapter two proved that an increase in powder layer thickness with the current powder characteristics, and the same additive technology (LPBF) is possible option. This increase is desirable for faster manufacturing and lower power consumption, leading to higher productivity. Similar mechanical properties and microstructure for the higher and lower powder layer thickness offer the engineers a wider process parameter window. It is worth mentioning that a lower powder layer thickness is restricted because of the powder characteristics (size, morphology, etc.), while a higher powder layer thickness requires an improvement in the additive manufacturing machine technology.

Different analyses have been conducted on TEM samples, such as phase fraction on EDS maps. Since showing all the data would extend the length of this study, the author of this thesis decided to stick to the presented results. As a result, the STEM images along with the EDS element maps were presented.

In the second project presented in chapter three, the deformation behaviour of the maraging steel is shown to be affected by the phase transformation. The additive process shows a significant effect on the microstructure, resulting in unique properties compared to a conventional manufacturing process. This project showed that the microstructural evolution of the high and low powder layer thicknesses is similar.

The cellular structure shown in the SEM images is known to be formed in hexagonal shapes. The TEM studied in chapter three showed the segregation of alloying elements in the cell structure and is considered to have a hexagonal shape marked in the TEM results.

The true stress-strain was used in this project to study the strain hardening behaviour through plastic deformation. First, the true strain was calculated based on the incremental increase in the length of samples. Then, assuming no volume change in the material, the area fraction change was calculated. The trues stress was considered based on the measured forces per updated cross-section area. The true stress-strain curve was then presented in this chapter.

In project three, the anisotropy of the additive manufactured part is shown. From the manufacturing point of view, it is crucial to consider the optimal building orientation based on the application of the additively manufactured part. The mechanical strength and ductility are supposed to be considered while deciding on the building direction. Since most maraging steel samples used in the industry are heat-treated, the strength is not affected significantly in different orientations. However, the anisotropy regarding cellular structure affects the ductility, which needs to be recognized.

Besides, it is concluded from this project that the mechanical properties might vary due to the cyclic heat loading in different layers. Another parameter that needs to be considered while manufacturing an industrial part is the relationship between the layer number and the critical areas in terms of stress concentration factor. It is worth mentioning that the layer number indicates the number of cyclic heat loads and residual stresses.

The fourth project showed that applying a soft recoater blade is not going to affect the microstructural evolution through the additive manufacturing process. However, lower packing density results in unmelted powder, which leads to lower ductility.

Chapter 7

Conclusions and future works

7.1 Conclusions

In this thesis, a comprehensive study on additively manufactured 18Ni-300 maraging steels was conducted. The material was investigated from different aspects by studying mechanical properties and microstructure through various techniques.

The first paper published in the journal of *Materials Science and Engineering: A,* under the title "*A trade-off between powder layer thickness and mechanical properties in additively manufactured maraging steels*," and the study was started with powder characterization. Gas atomized 18Ni-300 maraging steel powder particles were studied as the raw material for the additive process. The powder particle morphology and microstructure were investigated as well as the particle size distribution. Mostly spherical powder particles were depicted with cellular microstructure and an average size of 17.40 ± 8.46 µm through SEM micrographs. Finally, the powder particles were tracked to contain a 7.37% austenite phase through the XRD technique. The next part of the first paper was to study the porosity level as well as hardenability through the depth of cube samples manufactured through the LPBF technique in two different powder layer thicknesses. In both cases, the porosity level and the hardness through the depth were similar, while at the surface, they are slightly different. Then, uniaxial tensile tests were conducted on prints of the two powder layer thicknesses of 40 and 50 µm, and the microstructure and mechanical properties were investigated through SEM, EBSD, TEM, and XRD. On the microscopic scale, the two cases were showing a similar structure, while on macroscopic, the hardness, strength, and ductility were slightly higher in the case of 40 µm powder layer thickness.

Aluminum oxide and titanium nitride were distributed in the form of spheres and shells, respectively. Equiaxed and columnar dendrite cells formed the cellular structure around and inside the melt pools.

In the second paper with the title "*Plastic deformation throughout strain-induced phase transformation in additively manufactured maraging steels*," published in the journal of "*Materials and Design*," the same process parameter of powder layer thickness was studied with a different approach compared to the first paper. This study was conducted on the as-built samples without any heat-treatment process. The material was studied before and after deformation, and a strain hardening plot was extracted from the stress-strain results. Both 40 and 50 µm tensile samples were studied, and the deformation behaviour was investigated through different EBSD analyses. Studying the IPF, pole figure, and ODF, the material was shown to have (111) and (100) fibre textures after the manufacturing process in the as-built condition. However, the deformation intensified the fibre texture mentioned above. Both cases show similar deformation behaviour in this study. The strain-induced plasticity revealed a phase transformation resulting in removing the austenite phase and transforming it into a fully martensitic structure throughout the deformation process. This study was conducted by using the XRD technique. The EBSD grain boundary maps and the kernel average misorientation (KAM) agree with the XRD results. Finally, the STEM graphs, along with the element distribution maps, revealed the cellular structure and the segregation of Ti, Mo, Co, and Ni into the cell boundaries as well as high dislocation density in the cell boundary. Despite the similar behaviour, higher fibre texture in the 40 µm case agreed with the higher mechanical strength than the 50 µm cases. The segregated

alloying elements enriched the cell boundaries during solidification and acted as the austenite stabilizer resulting in austenite retained at the cell boundaries.

The third paper, "*Plastic deformation throughout strain-induced phase transformation in additively manufactured maraging steels*," investigated the 18Ni-300 maraging steel in horizontal and vertical build directions for as-built and aged samples. Cube samples were first studied for the variation of porosity and hardness through the depth. The porosity level showed an increase beneath the surface, followed by a decrease in deeper layers. Aged samples revealed higher hardness and lower porosity levels. Although the cellular structure was not visible in the aged samples in SEM micrographs, they are depicted through the TEM technique. A hierarchical structure was recognized with the lath martensite as the main structure formed inside the cellular structure. Cells then formed grains depicted in the EBSD IPF graphs. On a large scale, the melt-pools embrace the grains as well as the smaller structures. Another study conducted in this paper was the strain-induced phase transformation in the as-built/aged conditions and the horizontal/vertical builds. Phase transformation occurred due to deformation. With higher ductility observed in the as-built case, the chance for turning into a fully martensitic structure was higher, while in the aged samples, brittle fracture prevented a complete transformation of the austenite phase. The (111) and (100) fibre textures were recognized before the deformation and weakened after the plastic deformation. These fibre textures were associated with the build direction, while after the plastic deformation, a (011) texture along the tensile direction was observed. The (111) textures were perceived to be due to the transformation of austenite to martensite due to heating load cycles. The (011) fibre texture was formed due to the formation of austenite in the solidification process.

The fourth and last paper, "*Effect of recoater-blade type on the mechanical properties and microstructure of additively manufactured maraging steels,*" studied the effect of using the brush recoater instead of the conventional ceramic one in the LPBF technique. Porosity measurements showed an increase followed by a drop beneath the surface, while the hardness increased slightly through the depth. Through SEM micrographs, cellular structure was observed, and the fracture surface showed a ductile fracture. XRD results revealed that the austenite phase transforms from a 2% fraction into 0% throughout the deformation strain and the pole figure and the ODF results represented a texture formed due to the deformation.

Conclusively, this dissertation studied powder particle's properties as the pre-manufacturing process, some of the process parameters such as powder layer thickness, building direction, and recoater blade, and finally, the heat-treatment known as the post-processing parameter. The deformation through the tensile test in a quasi-static state was studied, and the phase study of the powder, as-built samples (after applying the additive process), aged samples (after applying the heat treatment process) before and after the deformation was investigated.

7.2 Recommendation for future work

7.2.1 Tailored mechanical properties

The current work shows that the material manufactured through the additive process has a directional grain structure. The texture results in anisotropic behavior. The material can have higher mechanical strength and ductility in specific directions. On the other hand, the heat-treatment process defined so far does not remove the anisotropic structure entirely. A combination of the heat-treatment process with the building orientation can lead to tailored mechanical properties. In this regard, two studies need to be conducted. The first one is the interrupted test and the second one is different heat-treatment processes specifically on additively manufactured samples.

The as-built parts have enough ductility to let the austenite phase transform entirely into the martensite phase. As a result, it is essential to study the start and end of the phase transformation process. An experimental interrupted test can reveal the process of phase transformation in the as-built samples. The relationship between the phase transformation and microstructural evolution can be studied. There is a chance that the amount of austenite governs the ductility of the material. By changing the process parameters, different martensite-austenite phase fraction can be achieved. A relationship between the phase fraction and mechanical properties can be investigated. The result of such a study can lead to a material tailored with a specific strength and ductility.

As shown in this study, the additive manufacturing process implies an internal heat-treatment process. Consequently, the heat-treatment process is expected to be studied comprehensively. A solution treatment process prior to the heat-treatment can help to remove the anisotropy of the material. However, an anisotropic material might be needed

in some cases. An aging time vs. temperature window can help a designer to tailor specific material behavior. The recommendation is to study the ductility and strength and phase fraction and texture in each heat-treatment process.

During the additive manufacturing process, the heat loads showed to implement a semi heat-treatment process on the microstructure resulting in different mechanical properties and microstructure. Thermal analysis can show the relationship between the microstructure evolution with the cyclic heating and cooling loads. This study can be conducted experimentally by studying the phase fractions and grain structure in multiple layers of the material. The top layers (finishing layers) experience fewer heating loads while the lower layers (closer to the build plate) experience higher heating cycles. The hypothesis is that the lower layers have lower austenite fraction with higher strength and lower ductility.

An in-situ XRD can investigate the phase transformation through the heating and deformation process. The two parameters of heating and deformation can reveal the phase transformation mechanisms.

On the other hand, the effect of different heat-treatment processes on the reverted austenite formation can shed light on the aged samples' ductility. There is a chance that increasing the reverted austenite in the aging process increases the ductility while keeping the strength. Consequently, by changing the austenite fraction, a tailored ductility-strength material is obtainable.

With the results of the two experiments mentioned above on the anisotropy and heat-treatment, a tailored material with a specific strength and ductility in certain directions can be achieved.

7.2.2 Modelling and simulations

In addition to the experimental test explained above, a numerical model can help to predict the mechanical properties in different ways. A crystal plasticity framework can be developed on grain structures to model microstructure evolution through phase transformation. Besides, the effect of retained austenite fraction can be modelled to predict the manufactured part's strength and ductility. A physical model can also help to predict the mechanical behaviour as a function of grain structure.

The experimental studies on the heating and cooling cycles affecting the microstructure can be combined with a thermal simulation to model the microstructure's evolution through microscopic (local) heat-treatments. It is recommended that the heating cycle be modelled to analyze the phase change cycle that the material goes through. Each layer of material is shown to experience multiple heating cycles. It means that each layer goes through an $\alpha \leftrightarrow \gamma \leftrightarrow L$ process repeatedly, and this phase change cycle strongly affects the microstructure. It can be modelled and help design the experiment more efficiently to reach the design window.

Appendix A.

Copyright Clearance Center RightsLink®

Home | Help | Email Support | Sign in | Create Account

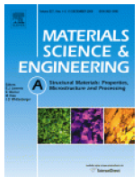

A trade-off between powder layer thickness and mechanical properties in additively manufactured maraging steels

Author:
SeyedAmirReza Shamsdini,Sajad Shakerin,Amir Hadadzadeh,Babak Shalchi Amirkhiz,Mohsen Mohammadi

Publication: Materials Science and Engineering: A

Publisher: Elsevier

Date: 3 March 2020

© 2020 Elsevier B.V. All rights reserved.

Please note that, as the author of this Elsevier article, you retain the right to include it in a thesis or dissertation, provided it is not published commercially. Permission is not required, but please ensure that you reference the journal as the original source. For more information on this and on your other retained rights, please visit: https://www.elsevier.com/about/our-business/policies/copyright#Author-rights

BACK CLOSE WINDOW

© 2020 Copyright - All Rights Reserved | Copyright Clearance Center, Inc. | Privacy statement | Terms and Conditions
Comments? We would like to hear from you. E-mail us at customercare@copyright.com

Copyright Clearance Center RightsLink®

Home | Help | Email Support | Sign in | Create Account

Plastic deformation throughout strain-induced phase transformation in additively manufactured maraging steels

Author:
SeyedAmirReza Shamsdini,M.H. Ghoncheh,Mehdi Sanjari,Hadi Pirgazi,Babak Shalchi Amirkhiz,Leo Kestens,Mohsen Mohammadi

Publication: Materials & Design

Publisher: Elsevier

Date: 15 January 2021

Crown Copyright © 2020 Published by Elsevier Ltd.

Please note that, as the author of this Elsevier article, you retain the right to include it in a thesis or dissertation, provided it is not published commercially. Permission is not required, but please ensure that you reference the journal as the original source. For more information on this and on your other retained rights, please visit: https://www.elsevier.com/about/our-business/policies/copyright#Author-rights

BACK CLOSE WINDOW

© 2020 Copyright - All Rights Reserved | Copyright Clearance Center, Inc. | Privacy statement | Terms and Conditions
Comments? We would like to hear from you. E-mail us at customercare@copyright.com

Copyright Clearance Center RightsLink®

Home | Help | Live Chat | Sign in | Create Account

A relationship between the build and texture orientation in tensile loading of the additively manufactured maraging steels

Author:
SeyedAmirReza Shamsdini,Hadi Pirgazi,M.H. Ghoncheh,Mehdi Sanjari,Babak Shalchi Amirkhiz,Leo Kestens,Mohsen Mohammadi

Publication: Additive Manufacturing

Publisher: Elsevier

Date: May 2021

Crown Copyright © 2021 Published by Elsevier B.V. All rights reserved.

Journal Author Rights

Please note that, as the author of this Elsevier article, you retain the right to include it in a thesis or dissertation, provided it is not published commercially. Permission is not required, but please ensure that you reference the journal as the original source. For more information on this and on your other retained rights, please visit: https://www.elsevier.com/about/our-business/policies/copyright#Author-rights

BACK CLOSE WINDOW

© 2021 Copyright - All Rights Reserved | Copyright Clearance Center, Inc. | Privacy statement | Terms and Conditions
Comments? We would like to hear from you. E-mail us at customercare@copyright.com

Copyright Clearance Center RightsLink®

Home | Help | Live Chat | Sign in | Create Account

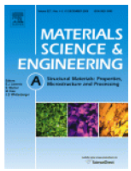

Effect of recoater-blade type on the mechanical properties and microstructure of additively manufactured maraging steels

Author: SeyedAmirReza Shamsdini,M.H. Ghoncheh,Mohsen Mohammadi

Publication: Materials Science and Engineering: A

Publisher: Elsevier

Date: 22 April 2021

© 2021 Elsevier B.V. All rights reserved.

Journal Author Rights

Please note that, as the author of this Elsevier article, you retain the right to include it in a thesis or dissertation, provided it is not published commercially. Permission is not required, but please ensure that you reference the journal as the original source. For more information on this and on your other retained rights, please visit: https://www.elsevier.com/about/our-business/policies/copyright#Author-rights

BACK CLOSE WINDOW

© 2021 Copyright - All Rights Reserved | Copyright Clearance Center, Inc. | Privacy statement | Terms and Conditions
Comments? We would like to hear from you. E-mail us at customercare@copyright.com

Curriculum Vitae

Candidate's full name: Seyedamirreza Shamsdini

Universities attended:

Shiraz University, Shiraz, Fars, Iran (2009-2012): M.Sc. Mechanical Engineering

Shiraz University, Shiraz, Fars, Iran (2004-2008): B.Sc. Mechanical Engineering

Awards:

2017-2020: International Differential Scholarship, University of New Brunswick

2017-2018: New Brunswick Innovation Foundation (NBIF)

2017: 2020: MITACS accelerate Award

2018: SEG Travel Grant to attend the CMSC-2018 Conference, Alberta

2019: CPDW-2019 Sponsorship to attend Canadian Material Diffraction Workshop, New Brunswick

Publications and Conference Presentations:

***Peer-Reviewed Publications**:*

Shamsdini, S., Ghoncheh, & Mohammadi, M. (2021). Effect of recoater-blade type on the mechanical properties and microstructure of additively manufactured maraging steels. Materials Science and Engineering: A, 141104.

Shamsdini, S., Pirgazi, H., Ghoncheh, M. H., Sanjari, M., Amirkhiz, B. S., Kestens, L., & Mohammadi, M. (2021). A relationship between the build and texture orientation in tensile loading of the additively manufactured maraging steels. Additive Manufacturing, 41, 101954.

Shamsdini, S., Ghoncheh, M. H., Sanjari, M., Pirgazi, H., Amirkhiz, B. S., Kestens, L., & Mohammadi, M. (2021). Plastic deformation throughout strain-induced phase transformation in additively manufactured maraging steels. Materials & Design, 198, 109289.

Shamsdini, S., Shakerin, S., Hadadzadeh, A., Amirkhiz, B. S., & Mohammadi, M. (2020). A trade-off between powder layer thickness and mechanical properties in additively manufactured maraging steels. Materials Science and Engineering: A, 776, 139041.

Shakerin, S., Hadadzadeh, A., Amirkhiz, B. S., Shamsdini, S., Li, J., & Mohammadi, M. (2019). Additive manufacturing of maraging steel-H13 bimetals using laser powder bed fusion technique. Additive Manufacturing, 29, 100797.

Cyr, E., Asgari, H., Shamsdini, S., Purdy, M., Hosseinkhani, K., & Mohammadi, M. (2018). Fracture behaviour of additively manufactured MS1-H13 hybrid hard steels. Materials Letters, 212, 174-177.

Conferences Presentations:

Shamsdini S., Mohammadi M., "Mechanical properties and microstructure of additively manufactured maraging steel". CMSC-2018 Conference, Alberta, Canada, 2018.